



Defense Special Weapons Agency
Alexandria, VA 22310-3398



DSWA-TR-96-45

Solid State Oxygen Compressor for Joule - Thompson Cryocoolers

W. N. Lawless
Ceram Physics, Inc.
921 Eastwind Drive
Suite 110
Westerville, OH 43081

March 1997

Technical

CONTRACT No. DNA 001-88-C-0244

Approved for public release;
distribution is unlimited.

19970408 009

DTIC QUALITY ENGINEERED 3

DESTRUCTION NOTICE:

Destroy this report when it is no longer needed.
Do not return to sender.

PLEASE NOTIFY THE DEFENSE SPECIAL WEAPONS
AGENCY, ATTN: CSTI, 6801 TELEGRAPH ROAD,
ALEXANDRIA, VA 22310-3398, IF YOUR ADDRESS IS
INCORRECT, IF YOU WISH IT DELETED FROM THE
DISTRIBUTION LIST, OR IF THE ADDRESSEE IS NO
LONGER EMPLOYED BY YOUR ORGANIZATION.



DISTRIBUTION LIST UPDATE

This mailer is provided to enable DSWA to maintain current distribution lists for reports. (We would appreciate your providing the requested information.)

- Add the individual listed to your distribution list.
- Delete the cited organization/individual.
- Change of address.

NOTE:

Please return the mailing label from the document so that any additions, changes, corrections or deletions can be made easily. For distribution cancellation or more information call DSWA/IMAS (703) 325-1036.

NAME: _____

ORGANIZATION: _____

OLD ADDRESS

CURRENT ADDRESS

TELEPHONE NUMBER: () _____

DSWA PUBLICATION NUMBER/TITLE

CHANGES/DELETIONS/ADDITIONS, etc.) (Attach Sheet if more Space is Required)

DSWA OR OTHER GOVERNMENT CONTRACT NUMBER: _____

CERTIFICATION OF NEED-TO-KNOW BY GOVERNMENT SPONSOR (if other than DSWA):

SPONSORING ORGANIZATION: _____

CONTRACTING OFFICER OR REPRESENTATIVE: _____

SIGNATURE: _____

CUT HERE AND RETURN



DEFENSE SPECIAL WEAPONS AGENCY
ATTN: IMAS
6801 TELEGRAPH ROAD
ALEXANDRIA, VA 22310-3398

DEFENSE SPECIAL WEAPONS AGENCY
ATTN: IMAS
6801 TELEGRAPH ROAD
ALEXANDRIA, VA 22310-3398

REPORT DOCUMENTATION PAGE			Form Approved OMB No. 0704-0188
<p>Public reporting burden for this collection of information is estimated to average 1 hour per response, including the time for reviewing instructions, searching existing data sources, gathering and maintaining the data needed, and completing and reviewing the collection of information. Send comments regarding this burden estimate or any other aspect of this collection of information, including suggestions for reducing this burden, to Washington Headquarters Services, Directorate for Information Operations and Reports, 1215 Jefferson Davis Highway, Suite 1204, Arlington, VA 22202-4302, and to the Office of Management and Budget, Paperwork Reduction Project (0704-0188), Washington, DC 20503</p>			
1. AGENCY USE ONLY (Leave blank)	2. REPORT DATE	3. REPORT TYPE AND DATES COVERED	
	970301	Technical	890406 - 960618
4. TITLE AND SUBTITLE		5. FUNDING NUMBERS	
Solid State Oxygen Compressor for Joule - Thompson Cryocoolers		C - DNA 001-88-C-0244 PE - SDIO 63224C PR - SF TA - SB WU - DH00027	
6. AUTHOR(S)			
W. N. Lawless			
7. PERFORMING ORGANIZATION NAME(S) AND ADDRESS(ES)		8. PERFORMING ORGANIZATION REPORT NUMBER	
Ceram Physics, Inc. -921 Eastwind Drive, Suite 110 Westerville, OH 43081			
9. SPONSORING/MONITORING AGENCY NAME(S) AND ADDRESS(ES)		10. SPONSORING/MONITORING AGENCY REPORT NUMBER	
Defense Special Weapons Agency 6801 Telegraph Road Alexandria, VA 22310-3398		DSWA-TR-96-45	
EST/Ware			
11. SUPPLEMENTARY NOTES			
This work was sponsored by the Defense Special Weapons Agency under RDT&E RMC Code B 7664 DSFSB 00027 PRPD 1950 A 25904D.			
12a. DISTRIBUTION/AVAILABILITY STATEMENT		12b. DISTRIBUTION CODE	
Approved for public release; distribution is unlimited.			
13. ABSTRACT (Maximum 200 words)			
<p>This report summarizes the work performed in the original Phase II Program and the results of the ARPA - sponsored program. Prototypes of the Honey Comb Oxygen Generators (ARPA) as Solid State Oxygen Compressors for the J-T (Joule-Thomson) Cryocoolers were tested. Previous results conducted in the original Phase II Program contributed to this study, but are not totally documented.</p> <p>Rate - Controlled - Sintering Studies aided as a powerful diagnostic tool for the evaluation of the prepared power. The small, simple J-T Refrigerator provided the cooling system. The results of the performance of the ceramic-toughening methods and stress analysis will greatly aid in the design and building of the Ceramic Honeycombs for the J-T Cryocooler Prototype. It is concluded that the results of this Phase II Program will provide excellent technology for the advancement to the next level of study.</p>			
14. SUBJECT TERMS			15. NUMBER OF PAGES
J-T Cryocooler Solid-State Oxygen Compressor Honeycomb Oxygen Generator			240
			16. PRICE CODE
17. SECURITY CLASSIFICATION OF REPORT	18. SECURITY CLASSIFICATION OF THIS PAGE	19. SECURITY CLASSIFICATION OF ABSTRACT	20. LIMITATION OF ABSTRACT
UNCLASSIFIED	UNCLASSIFIED	UNCLASSIFIED	SAR

UNCLASSIFIED

SECURITY CLASSIFICATION OF THIS PAGE

CLASSIFIED BY:

N/A since Unclassified

DECLASSIFY ON: N/A since Unclassified

14. SUBJECT TERMS (Continued):

Stress Analysis

SECURITY CLASSIFICATION OF THIS PAGE

OVERVIEW

These Phase I and Phase II SBIR Programs were dedicated to a solid-state oxygen compressor for driving a Joule-Thomson cryocooler. The compressor is based on a ceramic honeycomb structure, and oxygen as the working fluid can provide refrigeration in the 54 - 90 K temperature range.

The Phase I Program involved theoretical modeling studies of the generator + J-T valve and demonstrated the feasibility and attractiveness of this solid-state concept.

The Phase II program was dedicated to the experimental demonstration of the compressor + J-T system and was organized as follows:

- CeramPhysics, Inc.: Program management, additional system-modeling studies, physical property measurements on honeycombs, system integration and testing.
- Ohio State Univ.: Powder preparation, extrusion of ceramic honeycombs, ceramic-toughening methods, stress analyses of the honeycomb structure (MASTERS THESIS).
- Kenny Associates, Inc.: Development of rate-controlled sintering schedules for honeycomb sinterings.
- Cryogenic Designs, Inc.: Design and construction of a Joule-Thomson system for testing with a honeycomb oxygen generator.

It was discovered late in this Phase II Program that the large batch of ceramic powder prepared at the outset had NOT been fully reacted -- these powders contained unreacted batch materials (oxides) and off-composition OS-3 powders. As a consequence, the sintering studies were meaningless, the honeycombs sintered poorly and cracked, and the ceramic-toughening studies were probably of limited value.

CeramPhysics requested and received a number of no-cost extensions of this Phase II program in order to make other funding arrangements for obtaining reliable powder and satisfactory honeycombs. These efforts came to fruition with an ARPA-sponsored program which ended in May, 1996. However, it was not possible within the ARPA program to test these

prototype honeycomb generators as oxygen compressors with the J-T system developed by Cryogenic Designs, Inc.

This Final Report documents the meaningful results obtained in the original Phase II Program and the results achieved in the ARPA-sponsored program under the final no-cost extension.

SUMMARY, CONCLUSIONS, AND FUTURE DIRECTIONS

SUMMARY AND CONCLUSIONS

Much of the work performed under the original Phase II program was later seen to be meaningless due to the unreacted powder used. Consequently, in what follows we will summarize by Sections the meaningful work performed in the original Phase II program and in the ARPA-sponsored program under the final no-cost extension.

SECTION I. PROTOTYPE HONEYCOMB OXYGEN GENERATORS (ARPA)

Four honeycomb modules were successfully tested at five temperatures in the range 525 - 650 °C by CeramPhysics. The modules were sealed and manifolded at the operating temperatures. The results of these tests are presented in APPENDIX A. Also presented are data on current-carrying capacity, on pressure-burst experiments, and on the decrease of the ionic conductivity of the ceramic electrolyte with current density.

The main conclusions from this ARPA-sponsored program are as follows:

1. Exact compliance with Faraday's law was found in all the module tests (99.6% index of regression). This shows that:
 - a. Electronic conduction in the ceramic and in the glass seals is negligible.
 - b. Sealing and manifolding at the operating temperatures is hermetic.
2. Current-carrying tests at the operating temperatures

show that current densities in the range 2-5 A/cm² are stable.

3. Pressurization tests on honeycombs show that burst pressures in excess of 77 psi are possible.
 - a. No pressure failures of internal honeycomb walls were observed.
 - b. The observed pressure failures were associated with external walls and have simple explanations and cures (i.e., it is far easier to strengthen external walls compared to internal walls).
4. The optimum operating temperature appears to be in the 550-600 °C range.

SECTION II. ADDITIONAL THEORETICAL MODELING STUDIES

Additional modeling studies were performed by CeramPhysics in the original Phase II program; these were stand-alone, general studies of important aspects of solid-state oxygen compression. Since these studies have been reported previously in Monthly Reports they are not collected here in an appendix.

The topics studied and the dates reported are summarized below:

1. Auxiliary Heater, Oxygen Yield Parameter, Source Air Flow Rates, and Miscellaneous Power Losses (July 3, 1989).
2. Self-Heating in a Channel Wall (October 2, 1989).
3. Dependence of Power and Operating Temperature on the Ratio of Wall Thickness to Channel Opening (January 2, 1990).
4. Theory of Spreading Electrode Resistance (March 30, 1990).
5. Tradeoffs between Ceramic Toughening and Compressor Power (July 26, 1990).
6. Numerical Solutions of Spreading Electrode Resistance (January 7, 1991).

These modeling studies are of a general nature and are not dependent on the unreacted powder used; consequently, these

studies contribute to the understanding and operation of the solid-state compressor.

SECTION III. RATE-CONTROLLED-SINTERING STUDIES

Kenny Associates, Inc. performed several excellent studies of rate-controlled sintering with pellets and honeycomb samples. Unfortunately, the unreacted powders used to make these samples rendered these studies essentially useless.

The Summary from the Final Report of Kenny Associates is given here in APPENDIX B.

It is concluded that the rate-controlled-sintering approach is a powerful tool for determining the optimum time/temperature sintering path for ceramics in the general case. It is also a powerful diagnostic tool for evaluating poorly prepared powder, although this was not the intended purpose in Phase II.

SECTION IV. OXYGEN J-T REFRIGERATOR

Cryogenic Designs, Inc. designed and built a J-T refrigerator system. The Final Report on this system from Cryogenic Designs is given here in APPENDIX C.

It was concluded that a small, simple J-T refrigerator can be constructed to provide 100 mW of cooling at 95 K with an oxygen flow rate of 1.1 SLM at a pressure of 700 psi. Design improvements are discussed in APPENDIX C.

SECTION V. CERAMIC HONEYCOMBS FOR J-T CRYOCOOLER

Ohio State University performed research on ceramic-toughening methods and stress analyses of the honeycomb structure. As mentioned above, the powder prepared at OSU in the beginning of Phase II was unreacted, and therefore the honeycomb extrusion work at OSU was useless.

The work at OSU constituted a MASTERS THESIS, and this entire Thesis is given here in APPENDIX D.

The conclusions from the work at OSU are as follows:

1. Vibratory milling of powder is superior to conventional ball milling due to reduction in the sintered grain size, an increase in the sintered density, and a twofold increase in the modulus of rupture.
2. Studies of sintered samples made from the unreacted powders yielded an estimate of 17 atmospheres for the pressure withstanding strength of internal honeycomb walls. This result, while suspect due to the unreacted source powder, is in qualitative agreement with the results of the pressurization experiments in SECTION I above.
3. Attempts were made to strengthen the ceramic (using the unreacted powder):
 - a. Zirconia additions increased the strength of the ceramic but also led to a porous structure.
 - b. Precipitation hardening was attempted by forming small amounts of the tetragonal phase (which would transform to the monoclinic phase as a stress-relief mechanism). However, it was found that the tetragonal phase would not precipitate (using unreacted powder).
 - c. Silicon carbide whiskers were incorporated, but a vigorous chemical reaction occurred between these whiskers and the ceramic.
4. Stress analyses of the honeycomb structure shows that:
 - a. The "stripe" arrangement of anode/cathode channels is inherently stronger than the "checkerboard" arrangement (The former is preferred for practical manifolding reasons).
 - b. The maximum principle stress occurs at the corner of a cell, and this means that filleting can improve the pressure-withstand strength of the honeycomb structure.

FUTURE DIRECTIONS

The successful demonstration of oxygen generator prototype modules (SECTION I) which are sealed and manifolded at the operating temperature clearly shows that this concept of an oxygen compressor for a J-T refrigerator is a practical concept. The results obtained in SECTIONS I through V above provide a good database for advancing the technology to the next level.

The FUTURE DIRECTIONS for this technology are the following:

1. The ceramic-strengthening work in SECTION V should be repeated using fully reacted powder, except for the use of silicon carbide whiskers. Other candidate whiskers should be explored (alumina, silicon nitride, boron carbide). The ceramic powder should always be fully reacted and vibratory milled.
2. The pressurization results in SECTION I and the stress analyses in SECTION V should be used to design a dedicated extrusion die for producing honeycombs capable of withstanding large pressures.
3. Using the results and powder from 1. and the die from 2., honeycombs should be fabricated and pressure-tested at operating temperatures (The honeycombs will self-pressurize under oxygen generating conditions for these tests).
4. The existing J-T refrigerator should be used with the honeycombs from 3. for cryocooler tests.
5. Additional system-modeling studies should be performed to interpret the results from 4. In particular, the effect of current density on the ionic conductivity of the electrolyte observed in SECTION I should be incorporated.
6. The results obtained in 1. through 5. should be used to design and built a final prototype cryocooler system, including improvements in the J-T refrigerator.

APPENDIX A

SUMMARY OF ARPA-SPONSORED PROGRAM

TECHNICAL BACKGROUND

The honeycomb structure is a monolith consisting of a large number of channels separated by thin walls (see FIGURE 2 below). The basic scheme for the generator is to arrange half of these channels to be air passageways which are open at both ends (cathodes); and to arrange the other half of the channels to be oxygen-collection channels which are closed at both ends (anodes). Then the application of a voltage causes oxygen to be pumped from the cathode channels into the anode channels. The anode channels have to be manifolded in order to withdraw the generated oxygen. Finally, the sealing of the anode channels and the sealing of the manifold to the honeycomb should be hermetic at the operating temperature (These concepts will be illustrated in the photographs below).

The bismuth-oxide-based family of ceramics were selected for this honeycomb technology for two reasons: First, these ceramics have oxygen-ionic conductivities that are 30-50 times larger than the most conductive zirconia ceramics which leads to lower operating temperatures (and thereby more reliable seals); and second, these ceramics can be formed in the honeycomb structure inexpensively owing to their relatively low sintering temperatures ($\sim 1100^{\circ}\text{C}$). For comparison the zirconias sinter at much higher temperatures which compromises honeycomb sintering.

A comparison of the oxygen ionic conductivity of a representative bismuth-oxide-based cera-

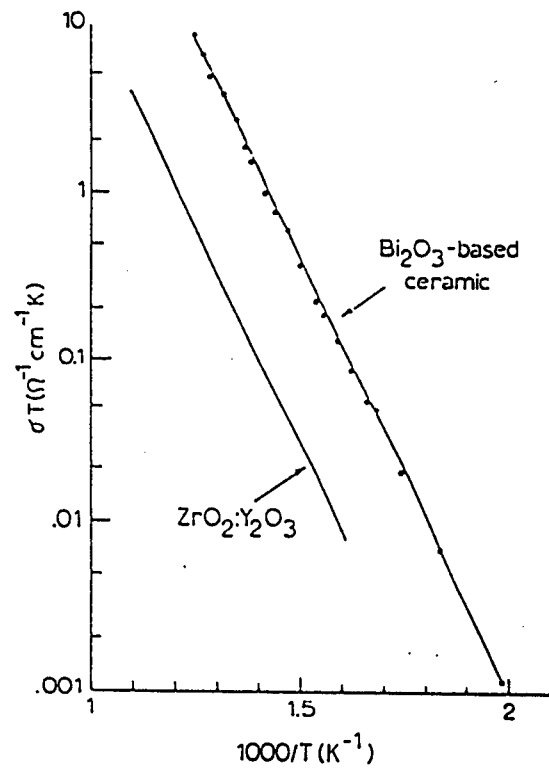


FIGURE 1. Oxygen ionic conductivity data for a representative bismuth-oxide-based ceramic and for the optimal zirconia ceramic.

mic and of the optimal zirconia ceramic is shown in FIGURE 1.

The first step undertaken by CeramPhysics was to develop the honeycomb-extrusion parameters for the bismuth-oxide-based types of ceramics in collaboration with Ohio State Univ. This was successful, and CeramPhysics retains the rights to this extrusion technology.

Next, CeramPhysics developed considerable background in the ancillary areas needed for this honeycomb technology: (1) Phase stability and physical properties of the bismuth-oxide-based ceramic compositions; (2) Compatible seals and metal alloys; (3) Electroding materials and methods; and (4) Thermo-dynamic systems analyses, including modeling codes (All these efforts yielded very important trade-secret information).

Because of this background at CeramPhysics, the Advanced Research Projects Agency funded a program to demonstrate proto-type honeycomb oxygen-generation modules. A commercial company specializing in honeycomb extrusions was supplied with the honeycomb-extrusion parameters and subcontracted to produce the honeycombs for this program (Applied Ceramics Inc., Atlanta).

PROTOTYPE HONEYCOMB OXYGEN GENERATORS

For reasons of cost and convenience, an available extrusion die was used by Applied Ceramics to extrude the honeycomb "logs" of the selected bismuth-oxide-based ceramic composition.

Generator modules cut from these green logs were machined (see below) and sintered, and in FIGURE 2 is shown a photograph of a green module and a sintered module. Also shown is a metal-alloy collection tube.

Note from the scale in FIGURE 2 that these modules are small -- this is due to the convenient die that was used. We shall return below to the dimensions of these honeycomb modules.

The modules in FIGURE 2 have been machined to provide both oxygen passageways and grooves for the wire interconnects, and in FIGURE 3 are shown schematic drawings of how these passageways and grooves were machined. The anode channels were machined

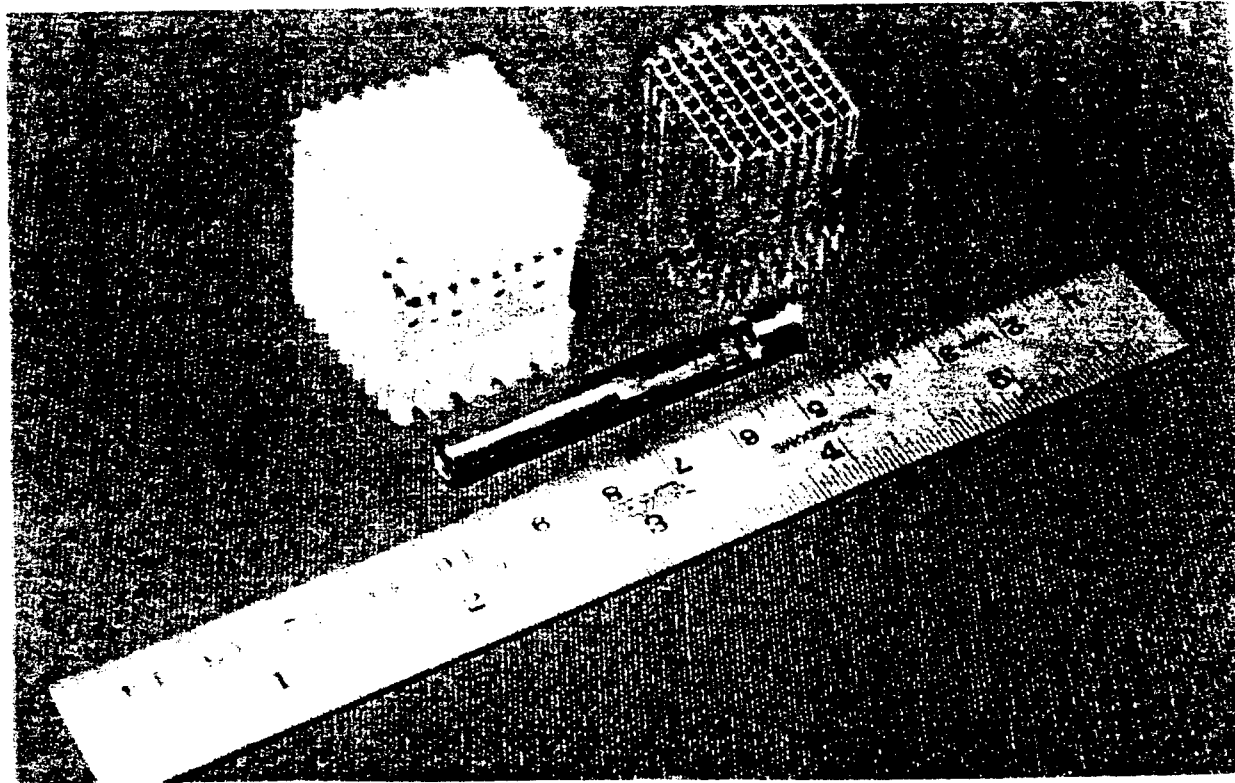


FIGURE 2. Photograph of a module machined in the green state and a machined module after sintering (17.1% shrinkage). A collection tube made from the metal alloy is also shown.

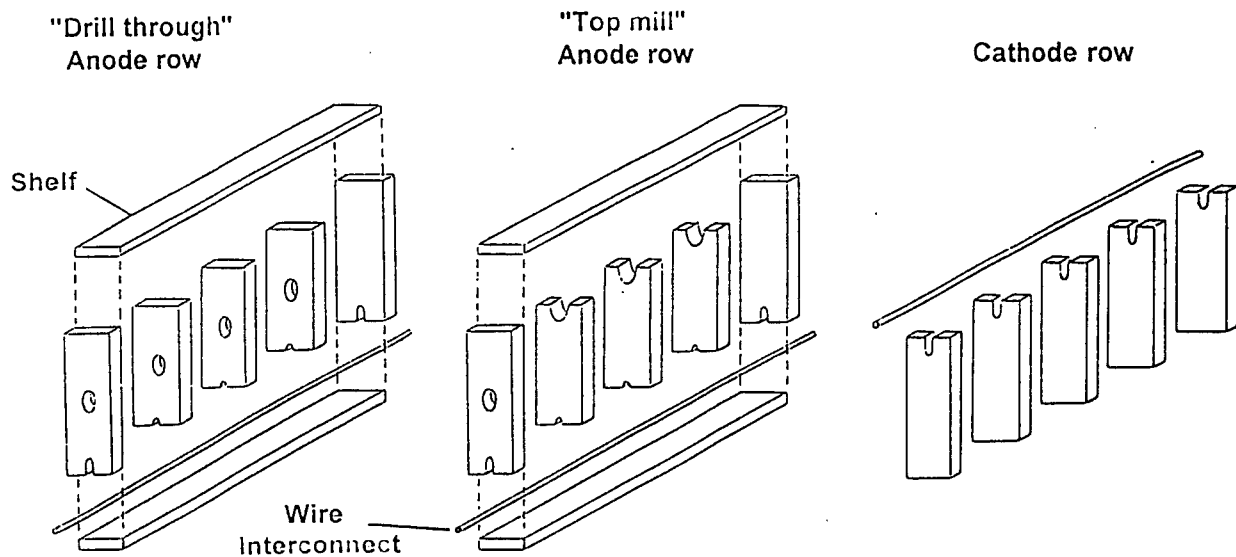
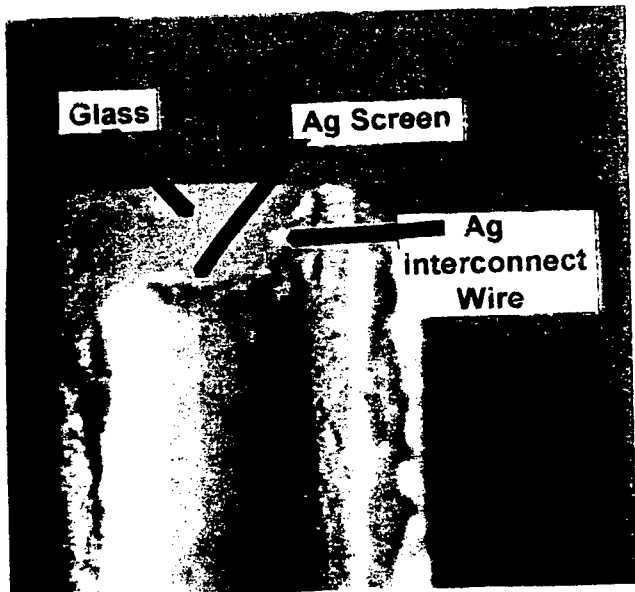


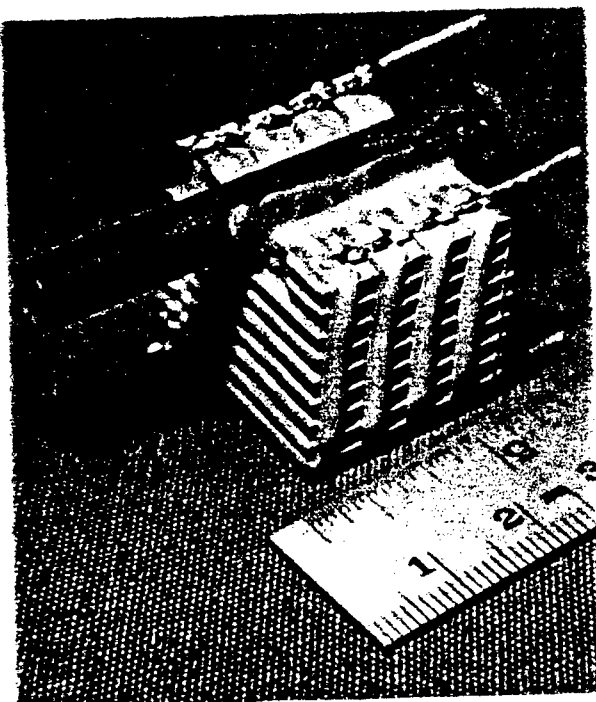
FIGURE 3. Schematic illustrations of the machining of the anode and cathode honeycomb channels (see text). The honeycomb module is machined in the green state prior to sintering.

two ways -- a "drill through" method and a "top mill" method. In the drill-through method the anode channel walls are drilled from the front face to (but not through) the rear face to provide oxygen passageways. In the top-mill method these passageways are milled into the tops of the anode channel walls. In both cases the oxygen generated in the anode channels passes through the hole in the front face and into the collection tube sealed to the side of the module (This can be judged from FIGURE 2).

The ends of the anode and cathode channel walls are grooved to accept the wire interconnects as shown in FIGURE 3, and a "Shelf" is inserted into the ends of the anode channels to support the glass used to seal the ends of these channels. Silver screens were used for these shelves, and this had the added benefit of reducing the electrical resistance of the wire interconnects.



(a)



(b)

FIGURE 4. (a) Photograph of a sectioned top of an anode channel. (b) Photograph of a sealed and manifolded honeycomb module with busbars attached.

The channels walls of the sintered modules were electroded with a platinum paste, and the wire interconnects were next sealed into the grooves in the ends of the anode and cathode channels with a gold paste. In the final step the glass seal was fired into the ends of the anode channels, and the metal collection tube was sealed to the side of the module with the same glass seal.

A microscope photograph of a sectioned top of an anode channel showing the glass seal, silver screen, and silver interconnect wire is shown in FIGURE 4(a). A photograph of a sealed and manifolded honeycomb module is shown in FIGURE 4(b). Also shown in FIGURE 4(b) are the busbars attached to the wire interconnects, and the anode and cathode rows are connected in parallel electrically to reduce the resistance of the module.

The scheme for assembling, wiring, and manifolding these modules is taught in the CeramPhysics' US Patent.

A swagelock fitting was attached to the metal collection tube for oxygen withdrawal to room temperature, and four modules were tested in a furnace at five different operating temperatures. The results of these oxygen-generation tests are shown in

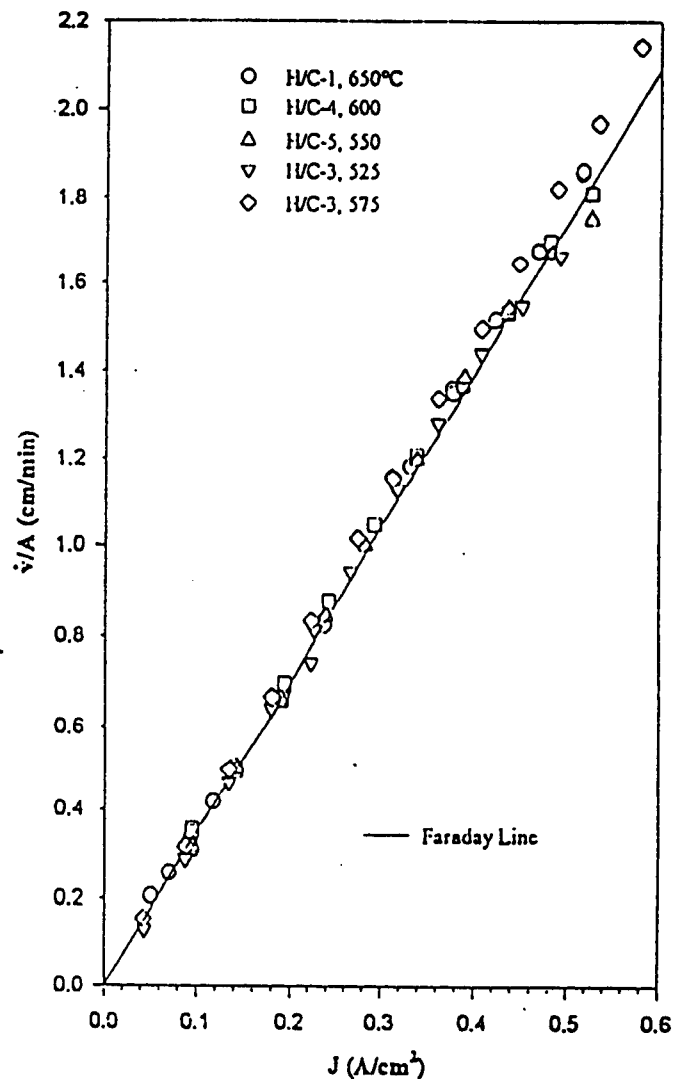


FIGURE 5. Oxygen-generation data measured on four prototype modules at five temperatures and plotted according to the Faraday Law.

FIGURE 5 where the oxygen flow rate per unit generation area is plotted versus the current density. The data are compared with the so-called Faraday Law of electrolysis. This law is independent of generator geometry, ceramic composition, and temperature, and is therefore the most stringent test of solid-state oxygen generation.

The data in FIGURE 5 demonstrate solid-state oxygen generation from prototype honeycomb generators and are the most important result of this prototype-demonstration program.

A remarkable finding is seen in FIGURE 5 -- namely, all five data sets follow the Faraday law very well. A fitting of all these data to the Faraday law yielded an index of regression of 99.6%.

The FIGURE 5 data are of much more than academic interest -- they in fact represent a major practical breakthrough for this technology. That is, if there were any electronic conduction through the ceramic honeycomb walls or through the sealing glass that plugs the tops of the anode channels, then the measured generation data would have fallen below the Faraday line in FIGURE 5. Also, if hermetic sealing conditions did not exist at the operating temperature, the data would not have fallen on the Faraday line. Therefore, all the current (power) supplied to the modules resulted in oxygen generation, and all the oxygen generated in the modules was delivered to room temperature.

It is of great practical significance that the metal tube and the sealing glass are chemically and thermally compatible with the ceramic honeycomb and provide hermetic conditions. The successful demonstration of these compatible materials was the second major breakthrough for this technology, and this glass seal and the metal alloy are commercially available.

CURRENT DENSITY

The third major breakthrough was in the current density that these honeycomb structures can support. That is, an upper limit

of about 0.5 A/cm^2 is used for oxygen generators based on closed-end tubes of zirconia, and the module measurements in FIGURE 5 were guided by this limit. However, in separate measurements it was found that two honeycombs supported 2 A/cm^2 at 550°C for 20 hours with no measurable degradation of performance. Two other honeycombs successfully supported 5 A/cm^2 at 600°C , and another honeycomb which supported 3 A/cm^2 at 550°C was later examined with a scanning electron microscope (SEM) and found to be indistinguishable from a honeycomb in the virgin state.

These current-density considerations lead us directly to the main reason why the honeycomb structure is the most desirable structure for oxygen generation, as follows. A figure of merit for oxygen generation is the specific oxygen generation rate -- i.e., the volume generation rate (dv/dt) per unit volume of ceramic honeycomb (V), given by

$$\text{Figure of Merit} = (dv/dt)/V = 0.00348 \text{ JA/V}$$

where J is the current density and A is the surface area for generation. The factor 0.00348 is the Faraday constant, dv/dt is in liters per minute (ℓpm), and V and A are in cm^3 and cm^2 , respectively. The larger $(dv/dt)/V$ is, the more volumetrically efficient will be the generator structure, and several manufacturing costs scale inversely with this efficiency. Honeycombs have large A/V -values, and large J -values have been demonstrated here -- therefore, very large figures of merit for oxygen generation are associated with honeycombs.

The modules here have $A/V = 3.8 \text{ cm}^{-1}$; a dedicated die would conveniently yield $A/V = 6.2 \text{ cm}^{-1}$. Going further, a dv/dt value of $4 \ell\text{pm}$ is the generation rate for home-breathing, and in the table below are given the honeycomb volumes needed to produce $4 \ell\text{pm}$ for various current-density values and for $A/V = 6.2 \text{ cm}^{-1}$.

Honeycomb Generator Volumes for 4 lpm

$J, A/cm^2$	V, cm^3	V, in^3
1	186	11.4
2	93	5.7
3	62	3.8
5	37	2.3

For example, at $J = 2 A/cm^2$, the generation honeycomb would be about 1" thick and have a face area $2 \frac{3}{8}'' \times 2 \frac{3}{8}''$. No other ceramic structure offers such a small size per lpm.

PRESSURE TESTS

Pressurization tests were made on these honeycombs (but not on the modules) by glass-sealing several small, 3 x 3 channel honeycombs into fixtures made from the metal alloy. The ends of these honeycombs were glass-sealed in a way that allowed separate pressure-testing of external walls and of internal walls. The samples were loaded in a furnace at 600 °C and pressurized to failure using a T-tank of helium gas.

Burst pressures in the range 40-60 psi were observed in these tests, and the failure mode was the same in all samples -- classic tension failures where the cross sectional area of the honeycomb was reduced for insertion into the metal fixtures. More important were the failure modes that were not seen -- no failures were due to the glass seals or to the internal walls.

DEPENDENCE OF ELECTROLYTE RESISTIVITY ON CURRENT DENSITY

One of the most interesting and important findings was the dependence of the resistivity of the ceramic electrolyte on current density in these honeycombs. This unusual effect is shown in FIGURE 6 where the ratio of the resistances at J and at $J=0$ are plotted versus J (The temperature dependence has been eliminated in these data). This ratio drops rapidly with increasing J (Note that the ratio is unity at $J=0$), then appears

to saturate above about $J = 0.5 \text{ A/cm}^2$. Data are shown in FIGURE 6 for both the modules in FIGURE 5 and for a single-channel sample. The effect is most pronounced for the module at 525°C where the ratio has dropped by a factor of 20.

For the module at 650°C in FIGURE 6 the ratio has a minimum at about 0.3 A/cm^2 , and this is due to the parasitic resistances of the metal components in the module. That is, the current being driven through the honeycomb walls to generate oxygen causes two effects -- the drop in the electrolyte resistance and self-heating. So, for this module at about 0.2 A/cm^2 the ceramic electrolyte resistance has been reduced below that of the metal components; at higher J -values and higher temperatures ($\sim 670^\circ\text{C}$) the resistance of the metal components dominate, and the minimum is due to the increase of the metal resistances with increasing temperature.

The J -dependence of the electrolyte resistance in FIGURE 6 is a real effect which is not understood. Nonetheless, this effect is of great practical significance for the power requirements -- i.e., not only is the resistance of the honeycomb structure reduced by virtue of the very thin walls, but the current density further reduces the resistance.

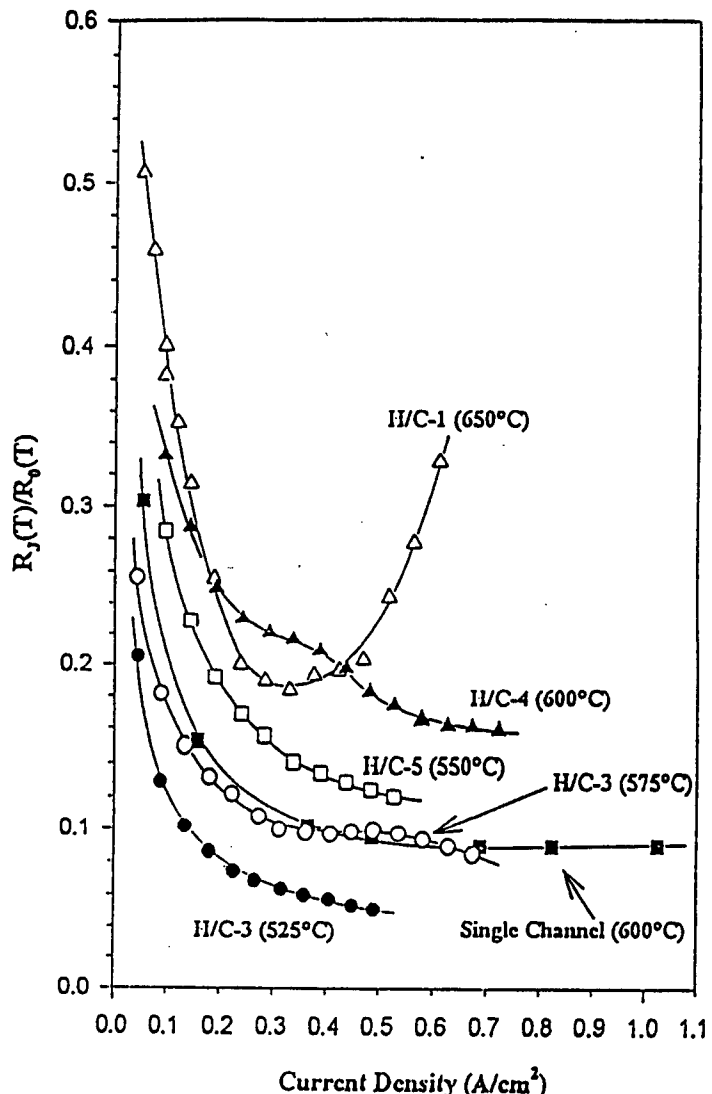


FIGURE 6. Resistance ratio as a function of current density measured on modules and a single-channel sample.

The data in FIGURE 6 show another important feature -- namely, the honeycomb generators should be operated well below 650 °C since otherwise the power dissipated in the metal components is wasted.

OXYGEN-GENERATION SYSTEM

The module tests shown in FIGURE 5 were carried out in a furnace which is unnecessary for an actual system. This system is illustrated in FIGURE 7 and involves a three-stream counter-flow heat exchanger attached to the generator. Source air is heated in the heat exchanger prior to entering the open cathode channels, and the spent air and generated oxygen are cooled in the heat exchanger. A power balance condition is achieved between the self-heating power dissipated in the generator and the heat flows into and out of the generator due to the gas streams -- the operating temperature is determined by this balance. The thermodynamic modeling of the system clearly shows that the heat exchanger cannot be too efficient (~90% is preferred), and this has the advantage of minimizing the cost of the heat exchanger.

The system modeling also shows that only relatively small amounts of oxygen should be removed from the source air (~10%) for greater efficiency. This removal is controlled by a draft fan on the air-exit leg of the heat exchanger, and this fan is the only moving part of the system.

The honeycomb generator is embedded in thermal insulation and encased in an enclosure. Finally, a jump-start heater is required to initially heat the generator close to the operating temperature.

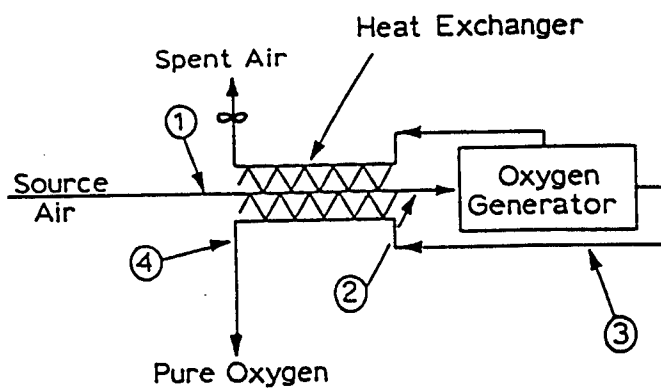


FIGURE 7. Schematic illustration of an oxygen-generation system.

APPENDIX B

Final Report
on Subcontract CPI-89-002

RATE CONTROLLED SINTERING OF OS-3 CERAMICS

for the program entitled

SOLID STATE OXYGEN COMPRESSOR
FOR JOULE-THOMSON CRYOCOOLERS

July 15, 1991

Submitted to

CeramPhysics, Inc.
921 Eastwind Drive, Suite 110
Westerville, Ohio 43081

by

Kenny Associates, Inc.
5840C McHines Place
Raleigh, NC 27604

Submitted by

Neal Kenny
Neal Kenny 919:872-2560
OXCOM2

Distributed to

Dr. W. Lawless, CeramPhysics, Inc.

1.0 Summary of the Rate Controlled Sintering Work

The objective of this work was to optimize the microstructure of extruded honeycombs of OS-3 ceramic for use in compressing oxygen for Joule-Thomson cryocoolers. High efficiency cryocoolers require honeycombs with thin walls (≤ 20 mils), which are capable of operating at high pressures (≈ 30 atm) and high temperatures (500°C). As a result, the honeycomb must have high strength, which requires the honeycomb microstructure to be of high density and small grain size. Rate Controlled Sintering (RCS) and Hot Isostatic Pressing (HIP) techniques were used in this investigation to produce the required microstructures.

All of the samples used in this investigation were supplied by Ohio State University. This investigation was limited to sintering studies, and to the microscopic evaluation of final microstructures.

Initial sintering studies of the OS-3 ceramic were done on *pressed pellets*, rather than *extruded honeycombs*. RCS studies on *pellets* produced a microstructure with high density—98% of theoretical—and a uniform grain size of 32 microns (1.3 mils). The temperature-time profile used to RCS sinter these pellets is presented in the report.

By combining RCS and HIP techniques, *pellets* were sintered with even higher density—100% of theoretical—with a finer grain size of 16 microns (0.6 mils). Although these samples have excellent density and grain size, they discolored during the HIP operation. Preliminary investigations at Kenny Associates, Inc., CeramPhysics, Inc., and Ohio State University rule out phase changes, contamination, and non-stoichiometry as the cause of the discoloration. Although the cause of the discoloration is not yet known, it is known that the mechanism underlying the discoloration does not affect the ionic conductivity of the samples.

Final sintering studies of the OS-3 ceramic were done on *extruded honeycombs*. RCS studies on *honeycombs* produced an optimized microstructure with high density—97% of theoretical—and a uniform grain size of 19 microns (0.7 mils). All of the honeycomb samples used in this investigation were in the form of cubes with an edge length of approximately 1/4 inch; all samples survived sintering without cracking or distorting. The temperature-time profile used to RCS sinter these honeycombs is presented in the report.

Although RCS sintering produced microstructures in the pellets and honeycombs with similar densities (98% and 97%, respectively) and grain sizes (32μ and 19μ , respectively), there were

many more complexities involved in sintering the honeycombs. The honeycombs exhibited a tendency to creep when sintered above 700°C, and to "de-densify" (a reduction in previously attained density) when sintering continued above 850°C. After all the experimental work of this investigation was completed, the scientists at Ohio State University discovered neither the pellets nor the honeycombs which were supplied to this investigation, were homogeneous in composition. The pellets and honeycombs were not the fully reacted OS-3 composition, rather they contained unreacted batch materials (other oxides) and off-composition OS-3 powders. Because of the difference in sintering behavior between the pellets and honeycombs, it is apparent that the honeycombs had the more serious problem. The compositional non-homogeneity explained the apparent creep and de-densification of the honeycombs during sintering: continued reaction of the batch materials to form the OS-3 phase led to both abnormal shrinkage (creep) and de-densification as the higher density batch materials formed the lower density OS-3 phase.

The discovery of the compositional non-homogeneity after the conclusion of the experimental work was very disappointing, because it meant the carefully developed rate controlled sintering profiles that maximized the density and minimized the grain size will not be useful for sintering either pellets or honeycombs of the correct OS-3 composition. Rate controlled sintering techniques produce excellent and consistent microstructures precisely because they are path dependent techniques. That is, RCS techniques are specifically designed to take a sample from an initial condition (composition, average particle size, and green density) along a precisely determined, and usually complex, sintering path (time-temperature profile) to produce a required microstructure. If the initial condition of the sample is substantially changed—and a change in composition is a substantial change—the sintering path to reach the required microstructure must also change.

Rate controlled sintering techniques were originally developed only to optimize sintering; the techniques were extended in the recent past to also optimize the burnout of organic forming aids. But it was never envisioned that the RCS techniques could be used to optimize the microstructure of partially reacted batch materials, since these unreacted materials undergo exothermic reactions, possible gas evolution, extensive diffusion, phase transformations, abnormal shrinkage, and density changes. It is truly remarkable that in this investigation the RCS techniques consistently delivered an optimized microstructure without physical failure of the thin walled body, given the presence of unreacted batch materials in the starting samples.

APPENDIX C

FINAL REPORT

on the

OXYGEN J-T REFRIGERATOR

by

Ray Sarwinski
CRYOGENIC DESIGNS, INC.
11404 SORRENTO VAL RD #115
SAN DIEGO, CA 92121
(619)-546-0870

Oxygen J-T Refrigerator Report

INTRODUCTION.

A Joule-Thomson refrigerator was designed, constructed and tested as part of a system utilizing a ceramic oxygen solid state compressor. This type of refrigerator was chosen to demonstrate the practicality of the combination of a clean compressor and a J-T device. A J-T refrigerator needs a clean compressor for it to operate over long periods of time. A solid state compressor is ideal. The J-T operates at a cold temperature of about 95 Kelvin. This is a sufficiently low temperature for the enhanced operation of infrared sensors (FLIRs). It is also cold enough for the operation of some High Temperature Superconducting devices. This oxygen J-T refrigerator was constructed for these reasons.

BASIC DESIGN PARAMETERS.

A number of design parameters were chosen based on the expected operating point of the compressor. The J-T would operate between 20 atmospheres and 1 atmosphere pressure with a throughput of 0.02 grams/sec. A perfect heat exchanger would yield refrigeration of about 0.12 watts. A simple counterflow heat exchanger (parallel tubes bonded together) was chosen so that the whole exchanger could be made in one piece. This would simplify cleaning and eliminate the possibility of leaks. It was therefore necessary to use a design for the J-T valve which would constrict the exchanger tube without severing the tube. We also wanted the J-T valve to be adjustable over a wide range of flows. We expected to operate the refrigerator from a high pressure gas bottle first as an open system before it was built into the ceramic compressor. We therefore also constructed a properly instrumented external gas handling system. The finished system is pictured in Fig. 1. The dewar, gas handling system and electronics easily fit on a desk top.

DETAILED DESIGN.

A. HEAT EXCHANGER.

Once the operating point was chosen, the size of the heat exchanger was determined. We chose a counterflow design consisting of two parallel tubes of stainless steel soldered together over the length of the exchanger. A simple computer program determined that the efficiency of the exchanger could be increased dramatically by the insertion of a number of stainless steel tubes in both the input and exit sides of the exchanger. The effect of the tubes is to increase the area in contact with the oxygen. Even though the stainless is known to have a low thermal conductivity, it is much better than oxygen at any temperature and pressure. We have used this trick before and found it to be effective. The use of one diameter for both the high and low pressure sides is not the most efficient but the benefits of single tube construction far out

weight the slight decrease in efficiency. We chose a tube size of 0.062 inch outside diameter having a wall thickness of 0.005 inches. Into each side (high and low pressure) was inserted 3 tubes each with an outside diameter of 0.022 inches, a wall thickness 0.003 inches and length 100 centimeters. Before assembly, all tubes were cleaned with Freon and then heated while a flow of ultra high purity helium gas was passed through the tubes. After the three tubes were inserted into the high and low pressure sides, the tube was bent into the proper configuration to accept the J-T valve and to provide a length over which cooling of an external object would take place. The tubes were then soldered together using an Allen salt flux and tin-lead-silver solder. After soldering, the ends of the exchanger were sealed to prevent contamination and the assembly cleaned externally to remove all flux. The heat exchanger was bent into the form of a multi-turned helix of diameter about 2 inches as seen in the Fig. 2.

B. J-T VALVE.

The J-T valve design was based on a previously successful design which formed a constriction in the exchanger tube by squeezing the tube between two 0.062 inch diameter rods. The amount of squeeze is adjustable by applying force to the upper rod through a 0-80 threaded rod. This rod was connected to a 1/8th inch diameter G-10 piece which extended through to the outside of the vacuum can and was sealed with double "O"-rings. Turning the rod adjusted the squeeze and therefore the flow. The J-T also automatically adjusts its flow during cooldown due to the differential contraction between the aluminum outside and the stainless inside of the valve. The details of its construction is shown in the included machinists drawings and in Fig. 3.

C. VACUUM CAN.

The vacuum can was constructed as shown in the drawings. It had an outside diameter of about 3 inches and was 6 inches high. This size was chosen to make assembly easy and was not intended to be the smallest refrigerator possible. As a practical device, a window could have been constructed in the base of the vacuum can to provide optical access.

D. GAS HANDLING SYSTEM.

A gas handling system was constructed as shown in the circuit diagram. The gas handling system is constructed entirely of stainless steel. This includes the pressure gages, the flow meter and the valves (which are stainless steel bellows valves). Stainless steel Swagelok fittings were used for all connections. The pressure gages (PX120 from Omega) measured the high and low pressures during operation. The stainless steel mass flow meter (Edwards Datametrics 0-1SLM) measures the oxygen flow up to 1 standard liter/minute. Ultra high purity oxygen gas from a standard cylinder (at 2800 psi) was used during open cycle operation. A 0-1000 psi regulator (Linde single stage) was used to control the pressure. The output was then passed through a 13x

Molecular sieve filter and then through a 0.5 micron mechanical filter. All parts were carefully cleaned before assembly and the gas handling system carefully leak checked.

E. INSULATION.

The system was to be checked out first without insulation. Super-insulation was added in stages as needed. The first stage of insulation is shown pictorially in Fig. 4. The final insulation is shown in Fig. 5.

G. INSTRUMENTATION.

For thermometry, we decided to go with a single Platinum resistance thermometer thermally tied to the lower cooling loop about 30 cm downstream of the J-T valve. The leads to the PRT were bi-filar 5mil Manganin. The lead resistance was measured at 58 ohms. The calibration was checked by dipping in liquid nitrogen. A 1/4 watt metal film resistor was used as a heater. It was connected about 10 cm downstream of the J-T valve. The leads again were 5mil Manganin with a resistance of 58 ohms. 0.5 grams of activated charcoal pellets were thermally tied to the cooling loop between the heater and the thermometer. The charcoal served to clean up the vacuum as the refrigerator cooled.

OPERATION.

We expected to make a number of runs, learning something new each time. On the first run, we expected to check the flow rate and so we did not insulate either the J-T or the heat exchanger. We first calibrated the flow meter, the pressure gages, the heater and the thermometer. We installed the vacuum can. We then diffusion pumped the vacuum can to a pressure of about 12 microns. We pumped and flushed the gas handling system at least 10 times using pure (Ultra-High Purity) oxygen. We set system pressure at 700 psi and started the flow. The temperature vs time is shown as Run 1 on the graph. We found the maximum flow to be 0.38 SLM. At this low flow and with the high thermal radiation heat load because of no insulation, we observed very little cooling. We warmed the system to room temperature to make the necessary changes.

For the second run, we worked on the J-T valve to increase the flow. We also added some superinsulation. We spiral wound two layers of insulation around the length of the exchanger and around the cooling turns as shown in Fig. 4. We put it back together and pumped the dewar. Again, we turned on the flow at 700 psi. The flow was set to 1 SLM. Cooling stopped at about 245 K so we upped the flow to 2 SLM using the variable J-T valve. Again we observed cooling to 192 K where the flow stopped due to blocking of the J-T valve by some contamination. We were able to unblock for short periods by adjusting the J-T valve but eventually the blocking became too severe. We warmed to room temperature to make more modifications.

For the third run, we added five more layers of superinsulation. We also added a liquid nitrogen trap to clean up the oxygen as it exited the tank. This was an experiment to test

the refrigerator and not the quality of the oxygen we used, so we allowed such a trap. The final configuration, when the refrigerator is operated with the ceramic compressor, will not have a contamination problem. We began the run with 700 psi pressure and a flow of 1.3 SLM. Cooling was more rapid and consistent with the mass of material used in making the refrigerator. The final temperature reached was about 162 K. We allowed the system to warm to room temperature. On all runs, we plotted the warm up time and found that for each run, the system warmed more slowly. From the warmup curve, we estimated the heat leak into the fridge was still large and probable due to a combination of poor vacuum and too little superinsulation.

For the fourth run, we added 8 more layers of SI to the cold end and then 8 more layers over the whole refrigerator-exchanger combination. See Fig. 5. To insure a good vacuum, we diffusion pumped the vacuum space overnight. Our vacuum at the start of the run, was better than 5 microns as read on the TC gage. We started with 700 psi and 1.1 SLM flow. The refrigerator cooled linearly to its final temperature of 94 K in 110 min. At this point, we started applying heater power at 400 mW. The refrigerator warmed. We gradually reduced the heater power until we found that we could hold temperature for thirty minutes with a heater power of 100 mW. This was very near to our design goal. We then turned off the heater and experimented with the variable flow J-T valve. We found that we could vary the flow between 0.3 and 3.0 SLM. This was a satisfactory range. Since our design goals were met, we warmed the refrigerator to room temperature and noted that the heat leak could still be reduced. Next time, we would recommend more superinsulation. All runs are shown on Graph 1 and the data is given in Table 1.

CONCLUSION.

We concluded that all of the design goals were met. The refrigerator operated at a sufficiently low pressure of 700 psi. (Operation from a higher pressure would increase efficiency). The refrigerator operated at the design flow in the center of the variable J-T range. The cooling power was as expected at 100 mW indicating a successful heat exchanger design.

In a redesign, there are some things we would change. To decrease cooldown times, we would attempt to reduce the total mass of the cooled portion by reducing the wall thickness of the stainless steel tubing and by reducing the amount of solder between the counterflow tubes. We would also reduce the mass of the aluminum portion of the J-T valve. We would reduce the size of the whole system by winding the heat exchanger in a tighter helix. We would also double the amount of superinsulation.

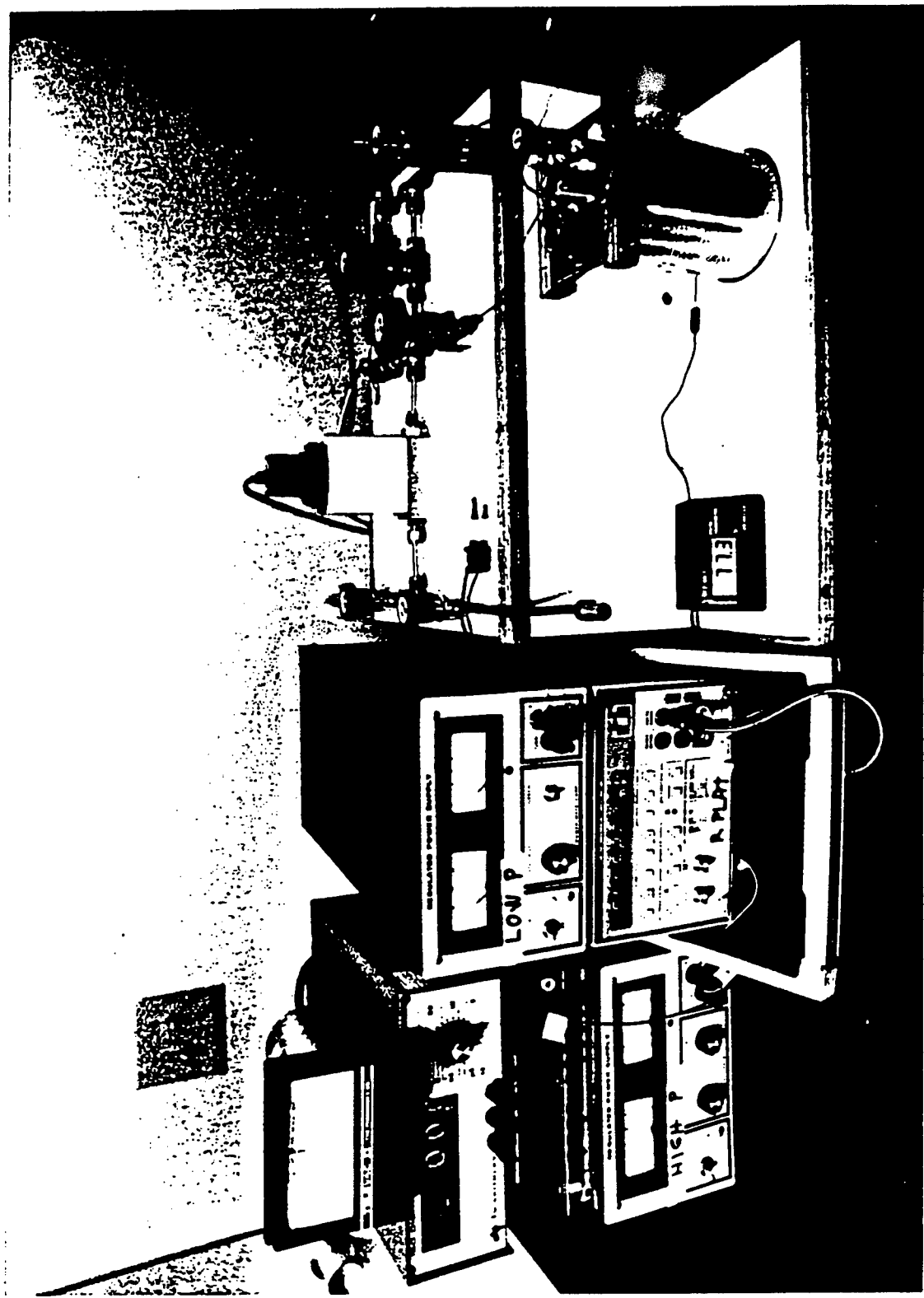


FIG. 1 6

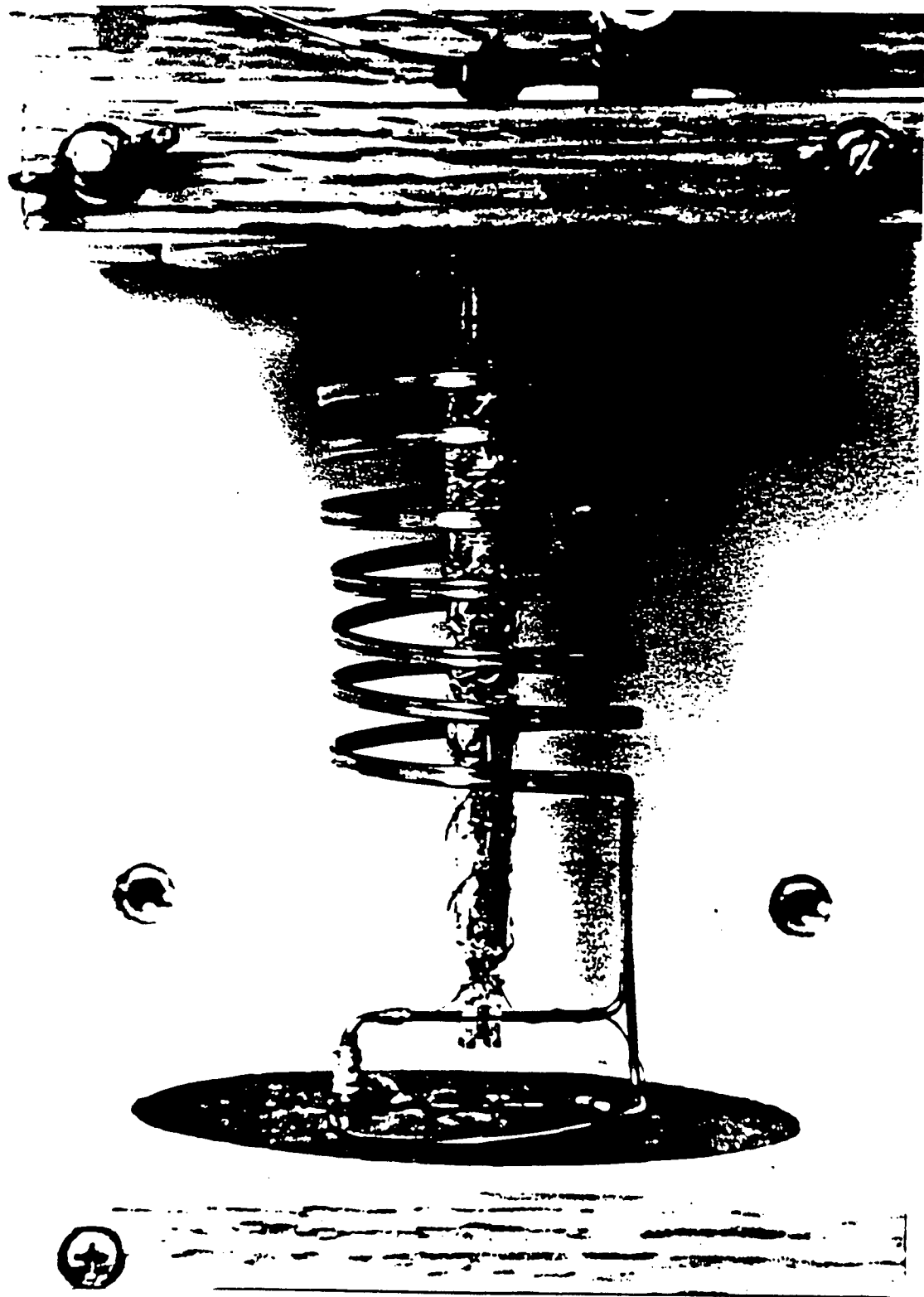


FIG. 2

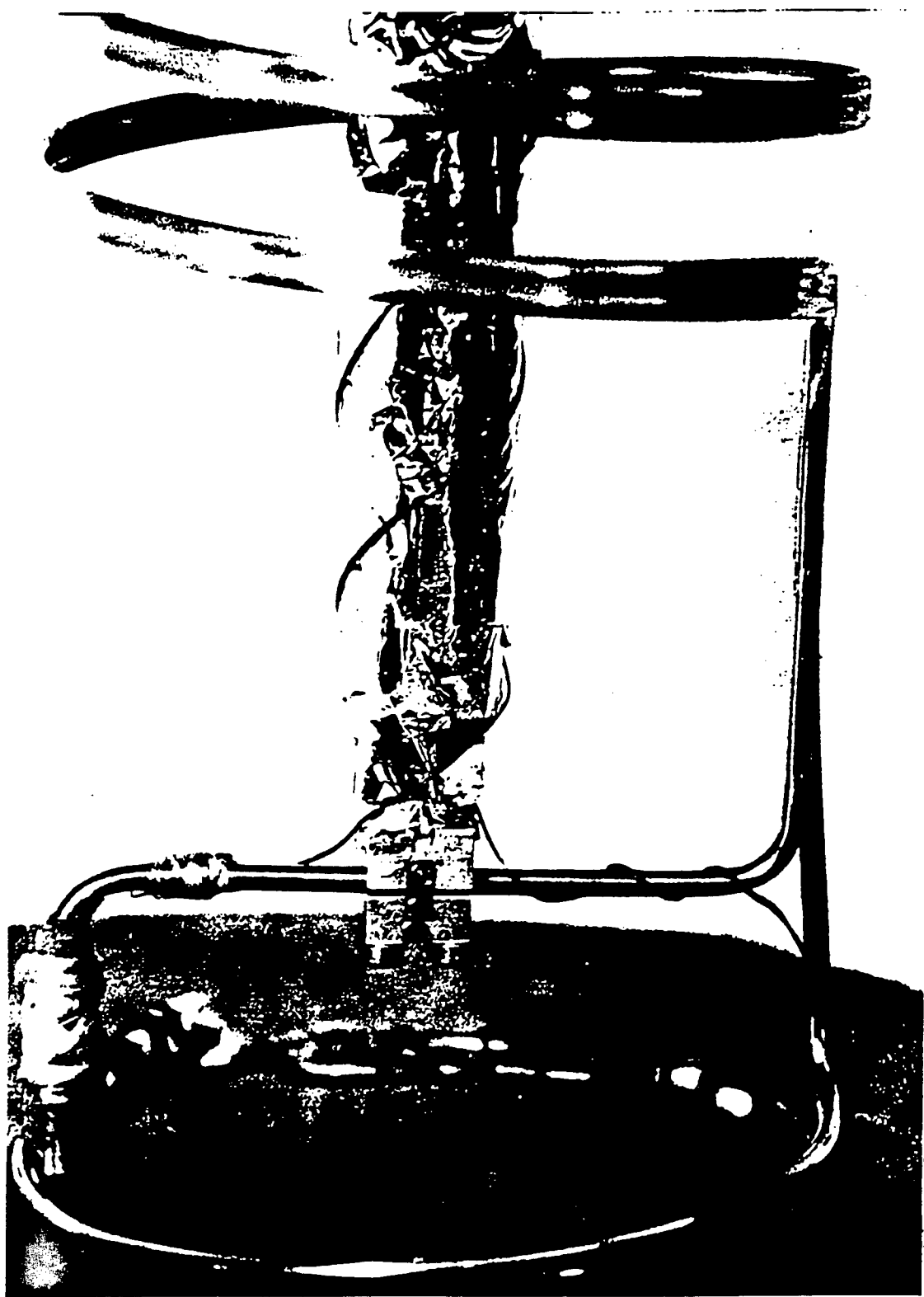


FIG. 3

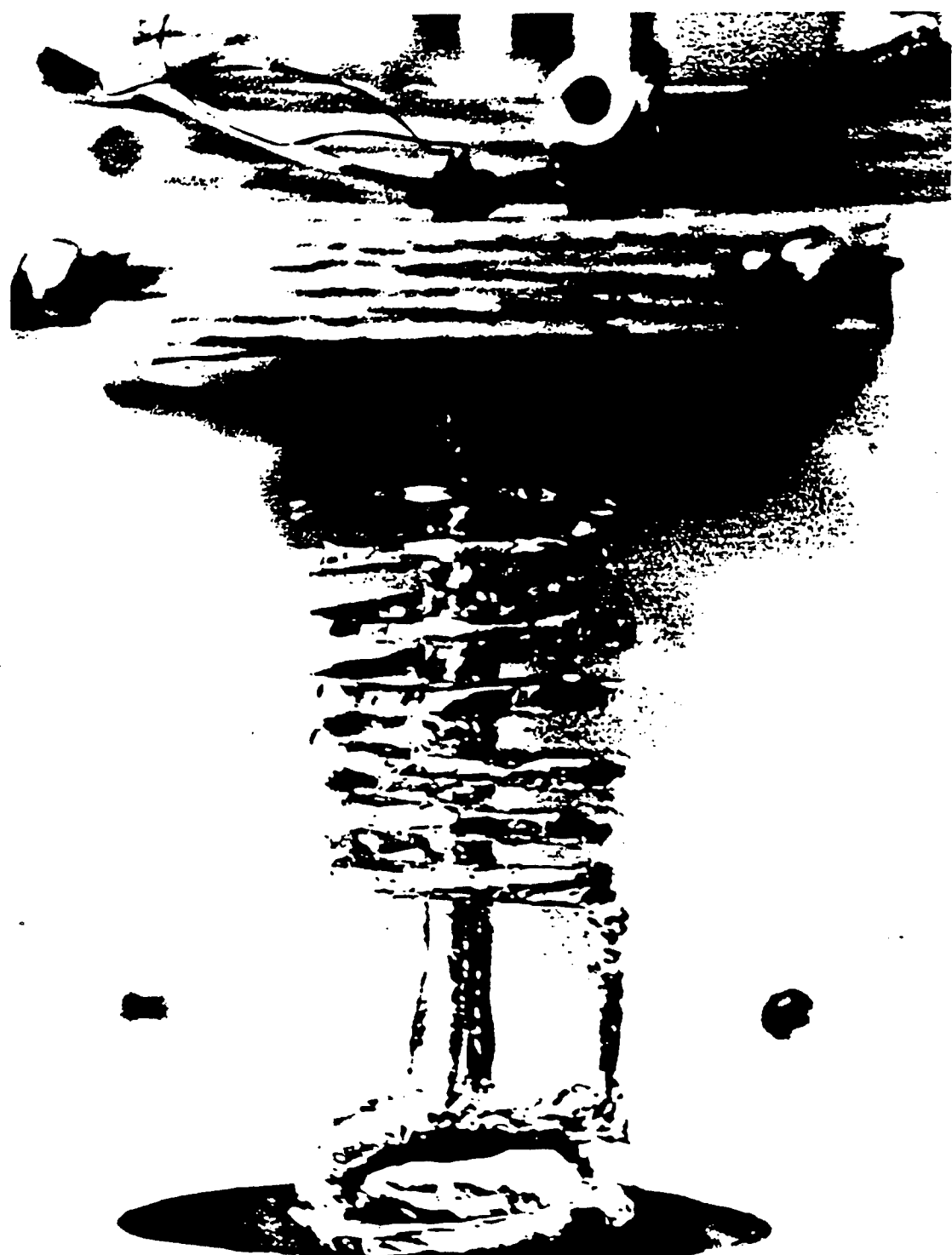


FIG. 4 9

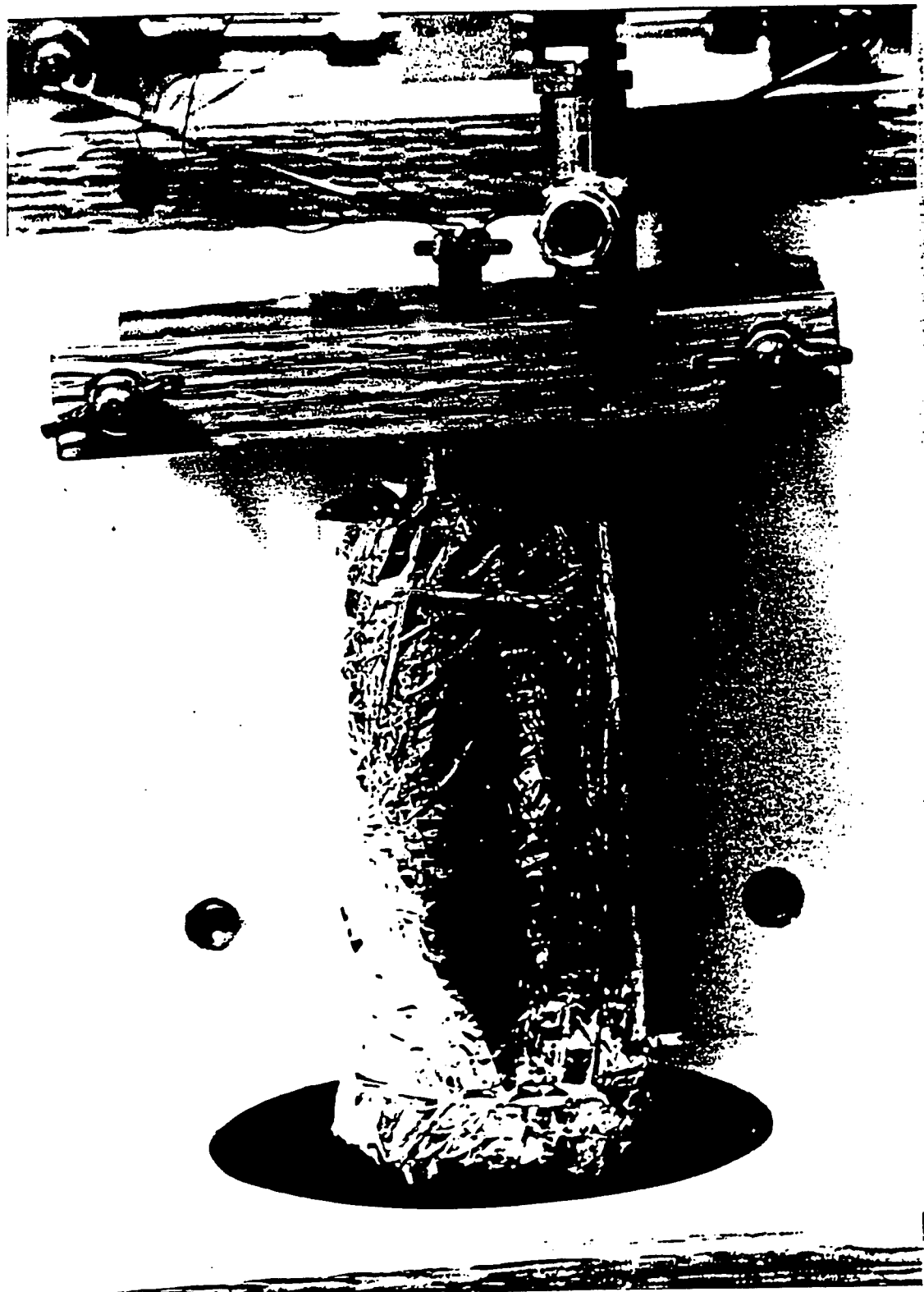


FIG. 5

CERAMPHYSICS JT RUNS

6/26/91

RUN 1

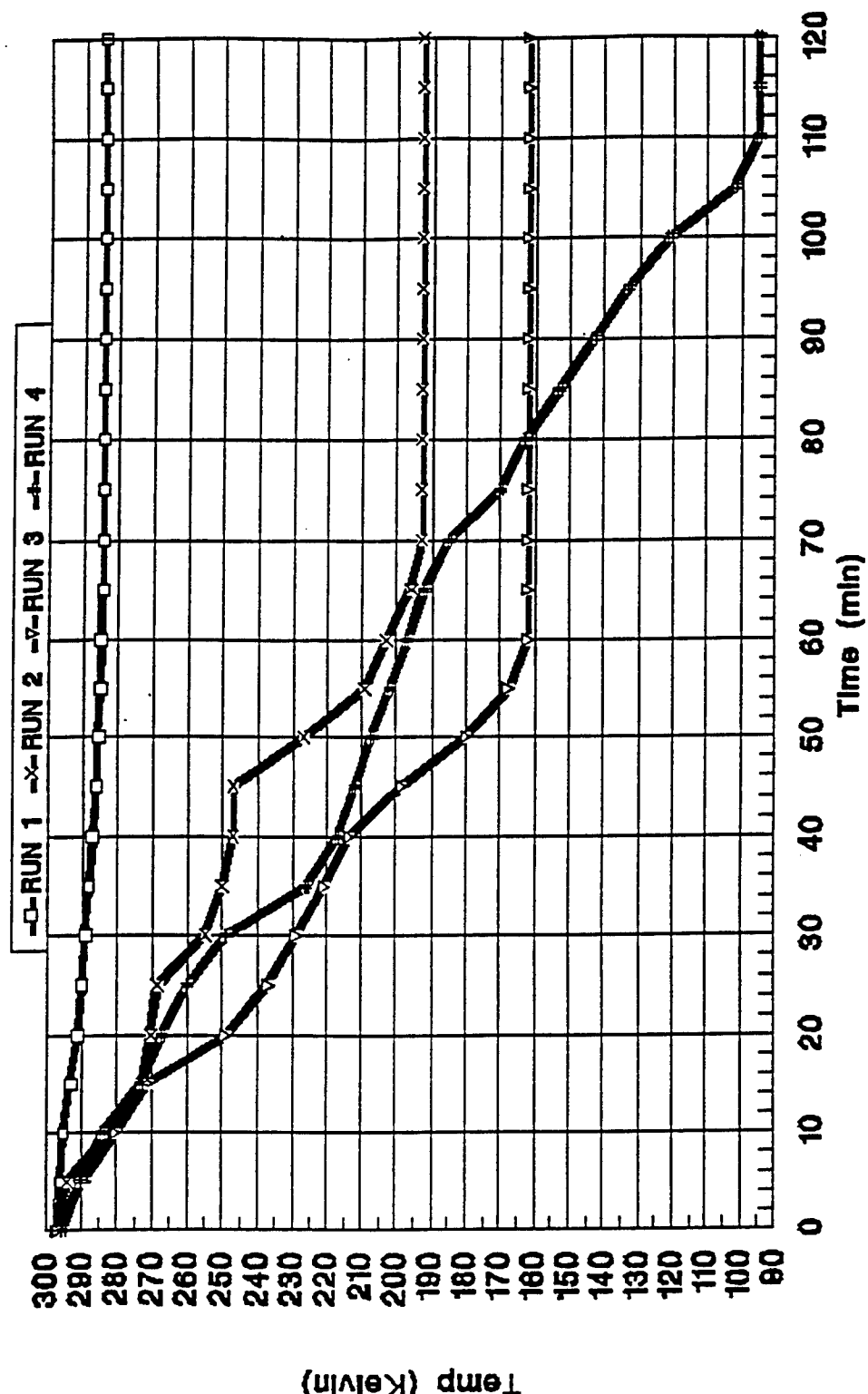
RUN 2

RUN 3

RUN 4

TIME MIN	RUN 1		RUN 2		RUN 3		RUN 4	
	C	K	C	K	C	K	C	K
0	24	297	24	297	23.5	296.5	22	295
5	23	296	21	294	16	289	17	290
10	22	295	9.5	282.5	7	280	11	284
15	20	293	0	273	-2	271	0	273
20	18	291	-2.5	270.5	-24	249	-6	267
25	17	290	-4.5	268.5	-36	237	-13	260
30	16	289	-18	255	-44	229	-24	249
35	15	288	-23	250	-52	221	-47	226
40	14	287	-26	247	-59.5	213.5	-56	217
45	13	286	-26	247	-74.5	198.5	-61	212
50	12.5	285.5	-46	227	-93	180	-66	207
55	12	285	-64	209	-106.	167.5	-71	202
60	11.8	284.8	-70	203	-111	162	-76	197
65	11.5	284.5	-77	196	-111	162	-81	192
70	11.5	284.5	-80	193	-111	162	-88	185
75	11.5	284.5	-80	193	-111	162	-103	170
80	11.5	284.5	-80	193	-111	162	-110	163
85	11.5	284.5	-80	193	-111	162	-120	153
90	11.5	284.5	-80	193	-111	162	-130	143
95	11.5	284.5	-80	193	-111	162	-140	133
100	11.5	284.5	-80	193	-111	162	-152	121
105	11.5	284.5	-80	193	-111	162	-171	102
110	11.5	284.5	-80	193	-111	162	-178	95
115	11.5	284.5	-80	193	-111	162	-178	95
120	11.5	284.5	-80	193	-111	162	-178	95

JT RUNS
at Cryogenic Designs, Inc.
6/28/91 - 7/3/91

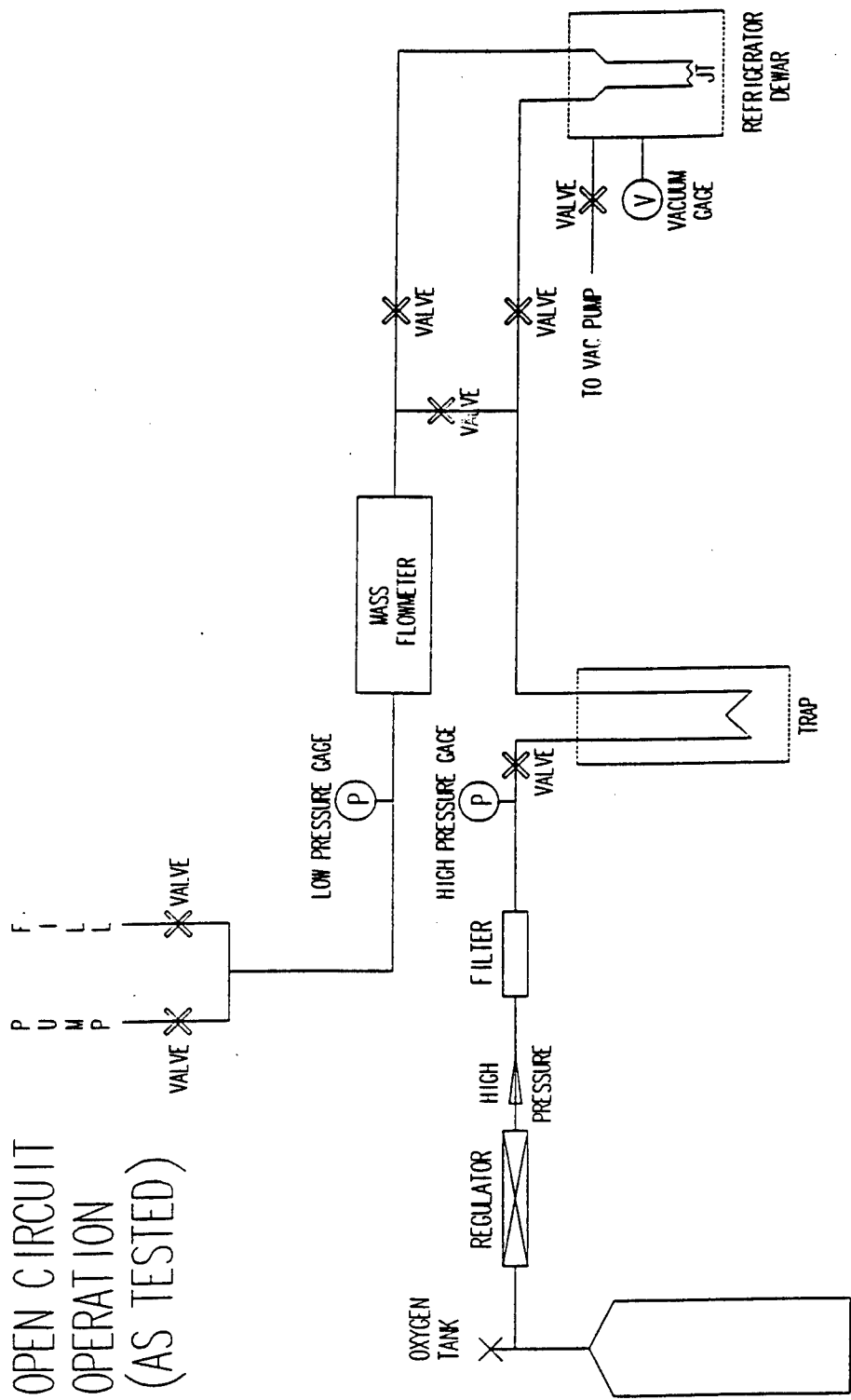


GAS HANDLING CIRCUIT

and

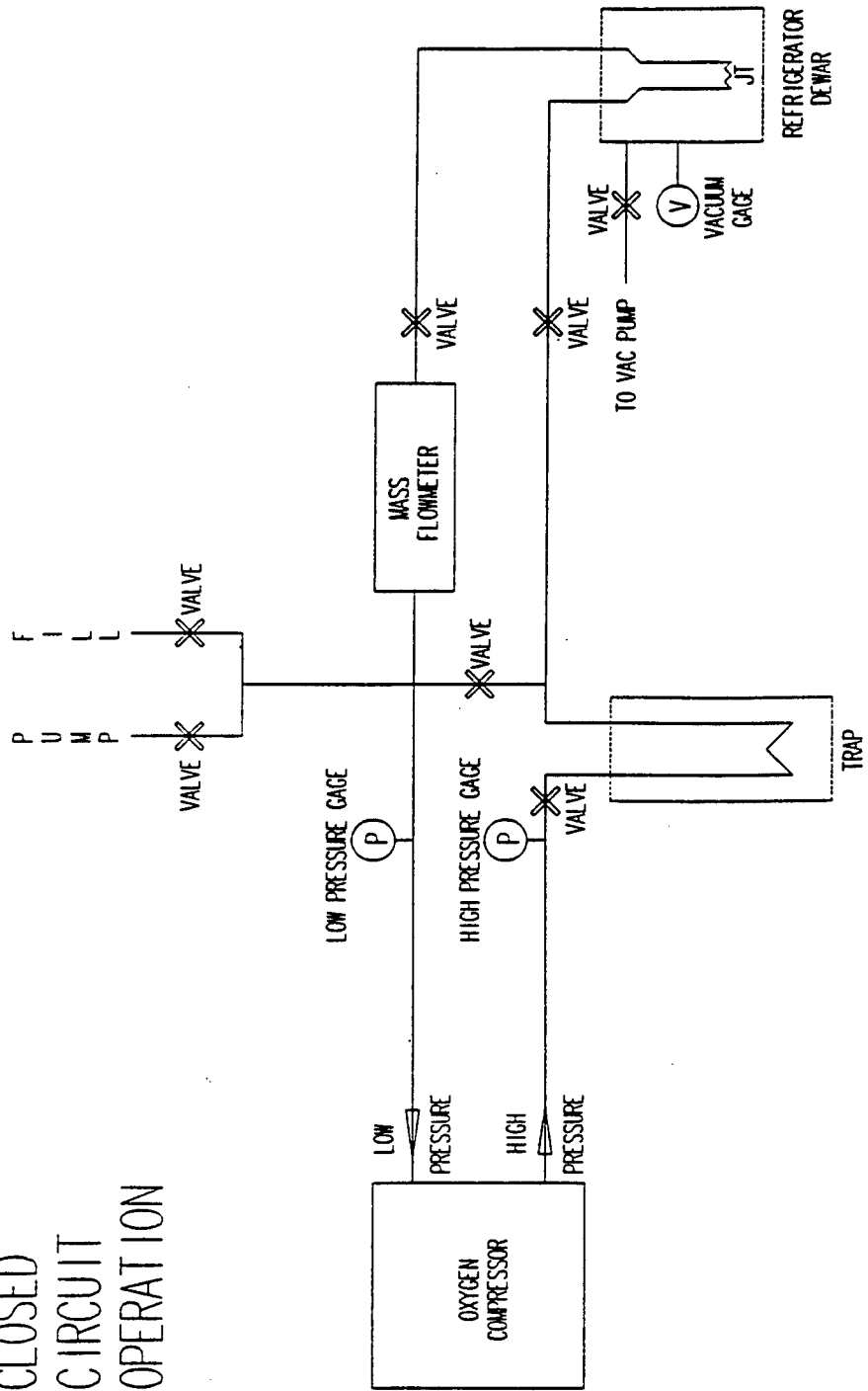
MECHANICAL DRAWINGS

OPEN CIRCUIT
OPERATION
(AS TESTED)



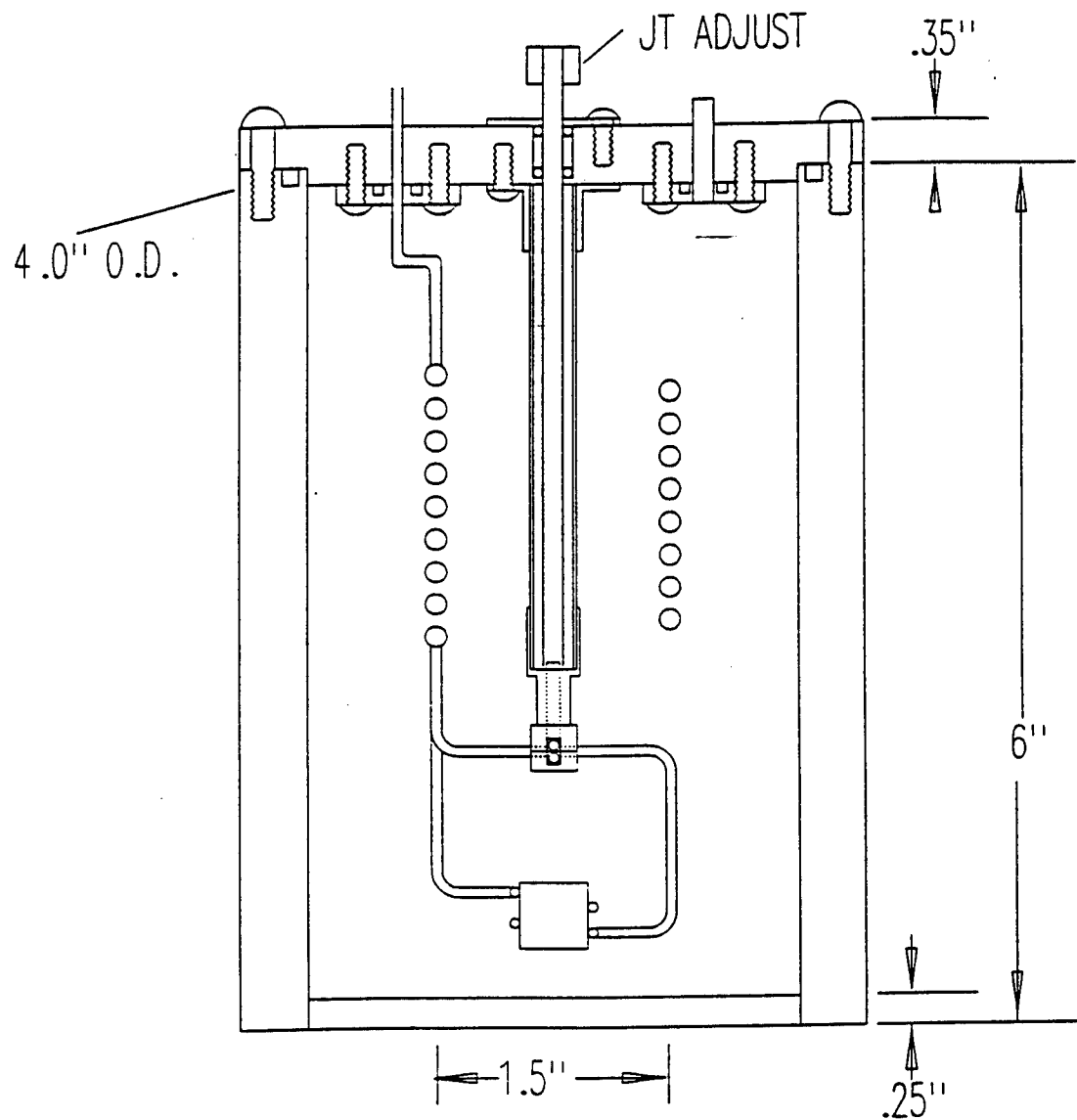
R. SARWINSKI 10/10/89

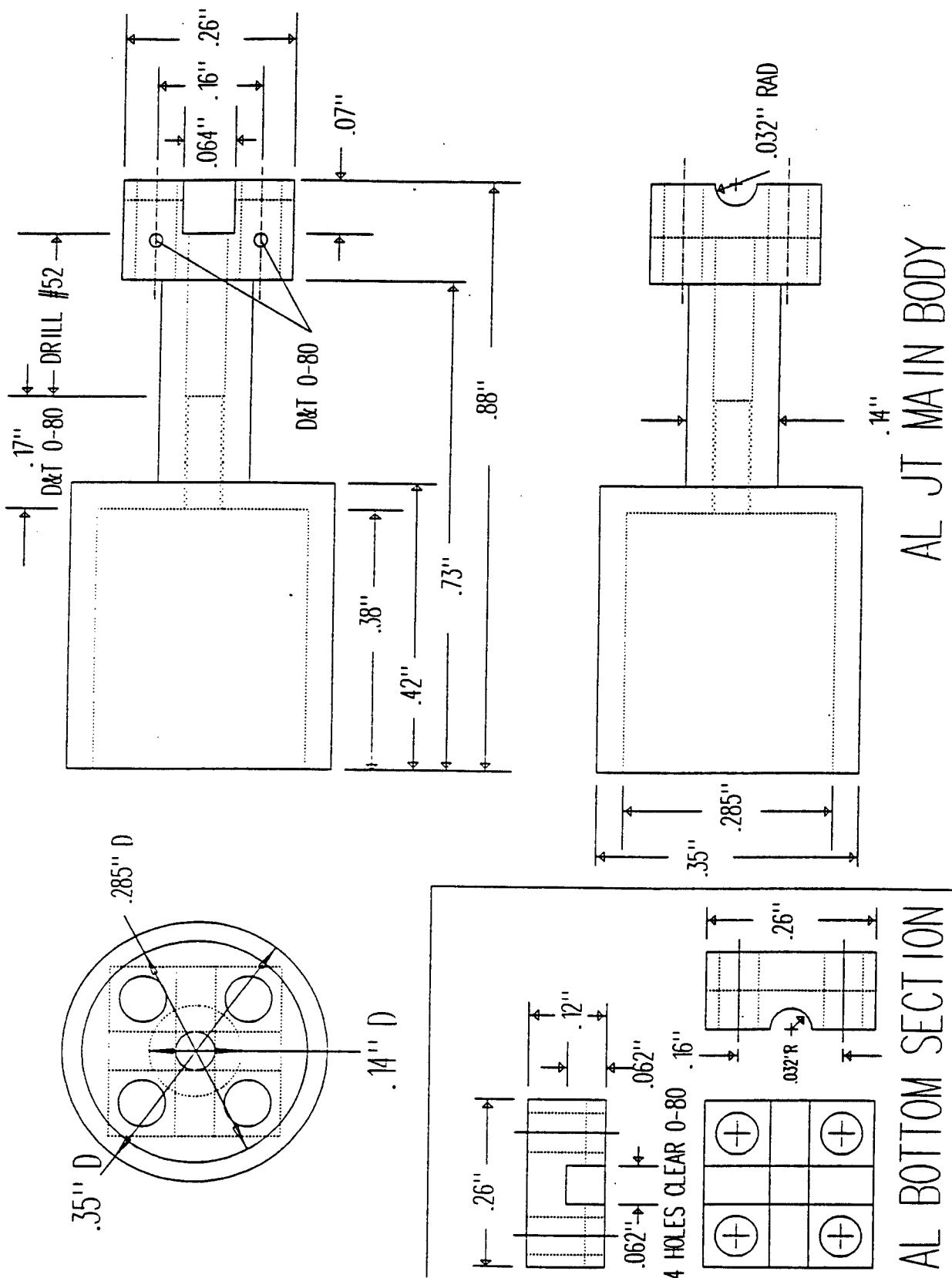
CLOSED
CIRCUIT
OPERATION

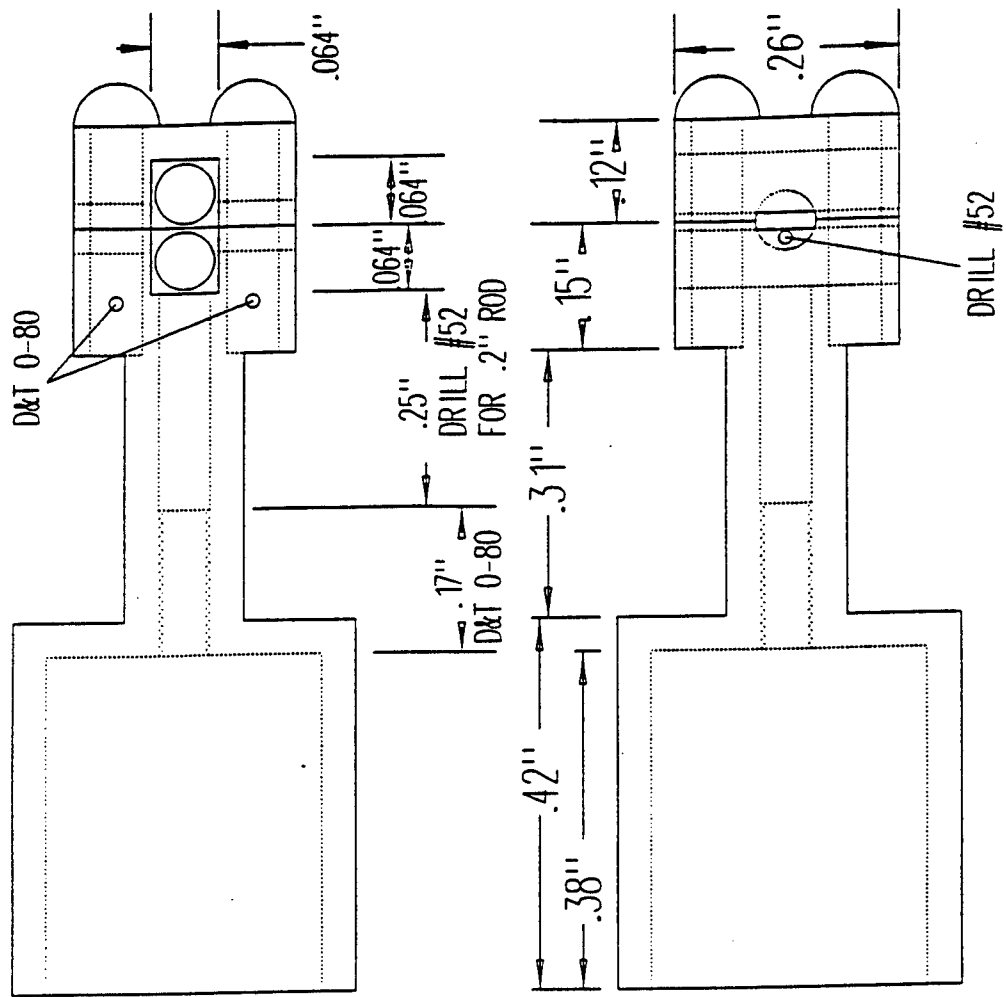


R. SARWINSKI 10/10/89

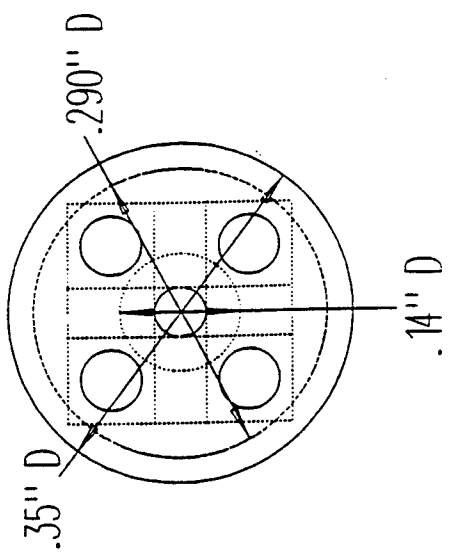
JT IN DEWAR





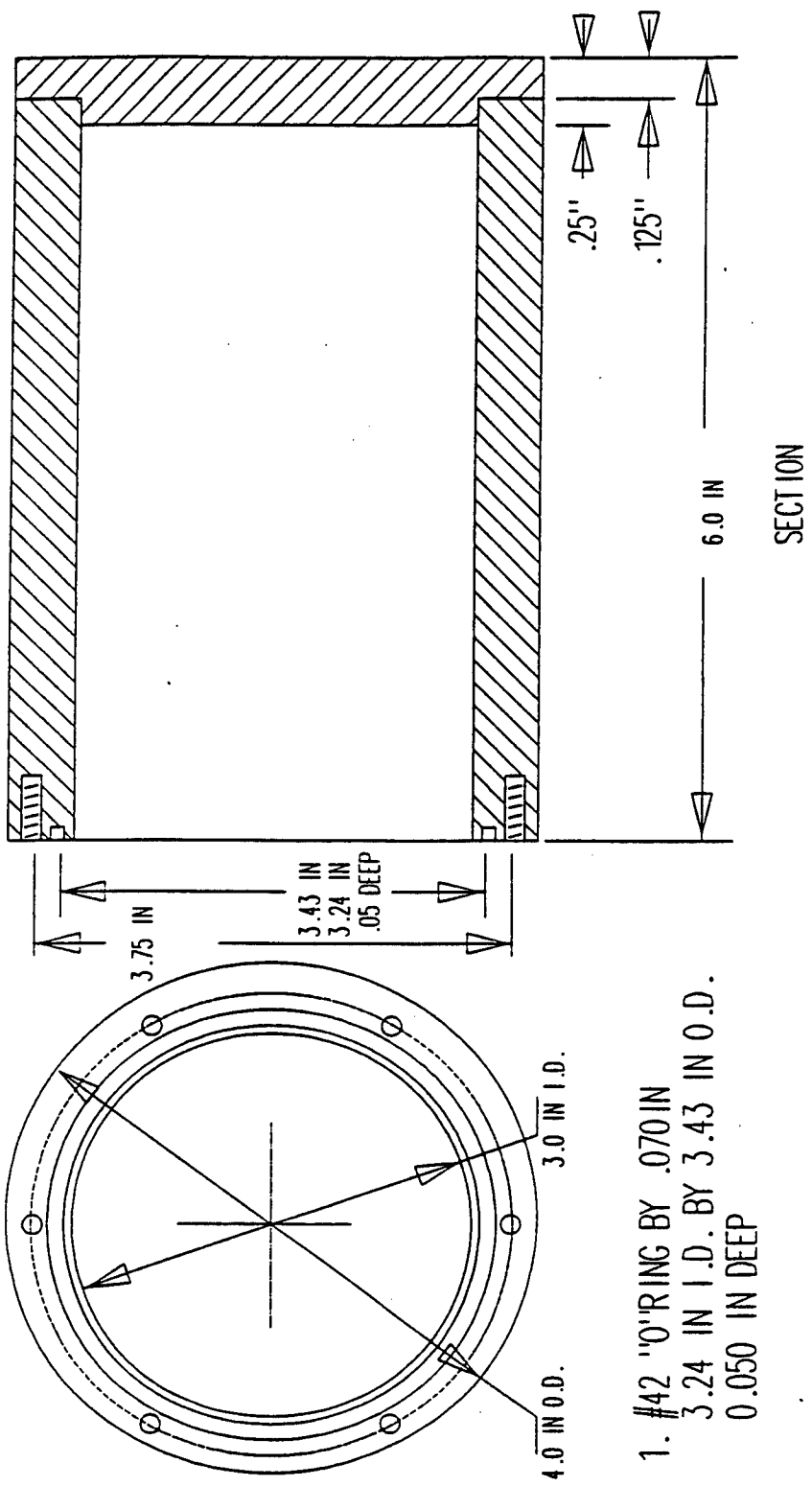


10/24/89 R.E. SARWINSKY

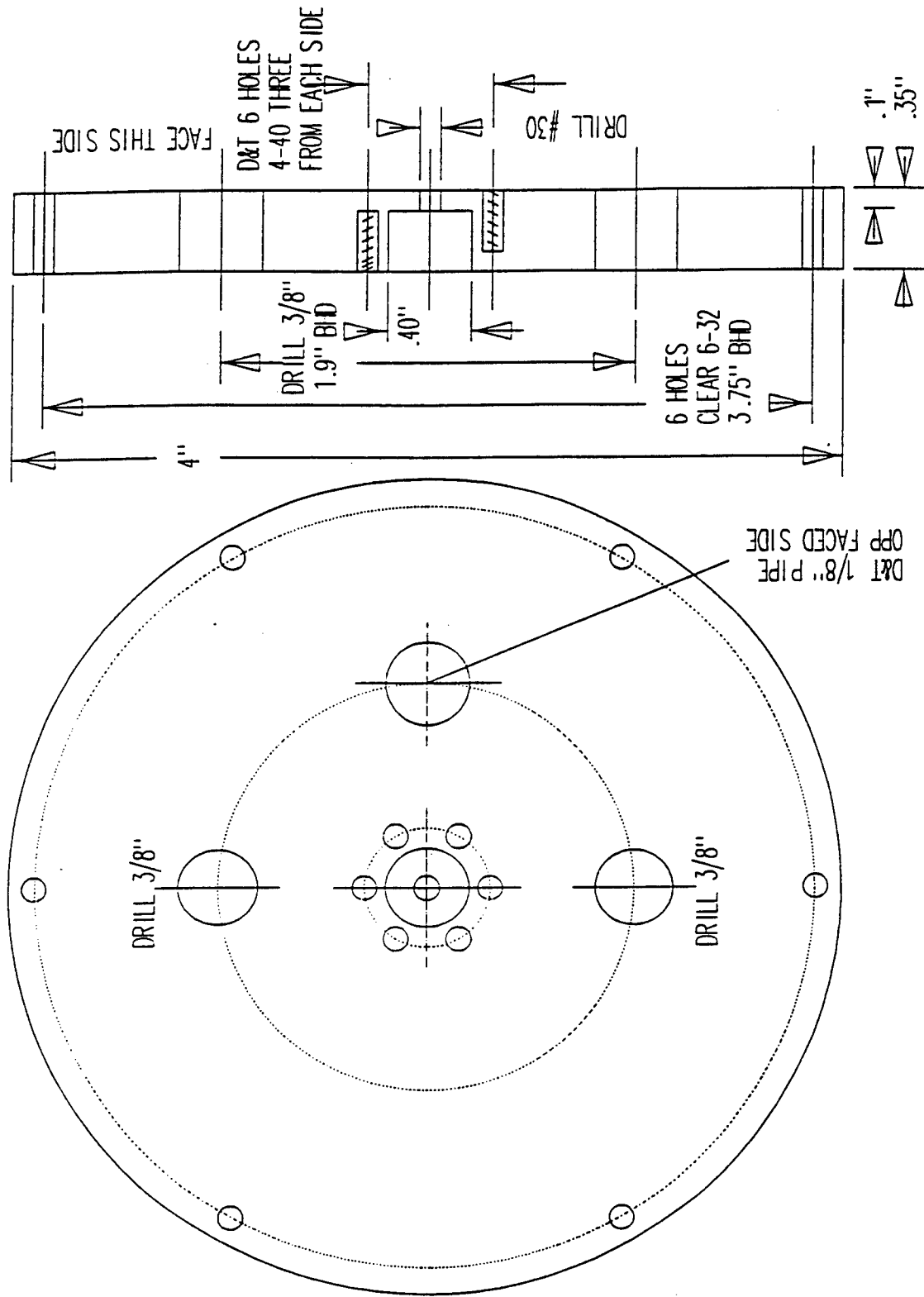


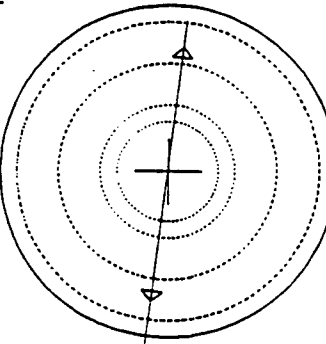
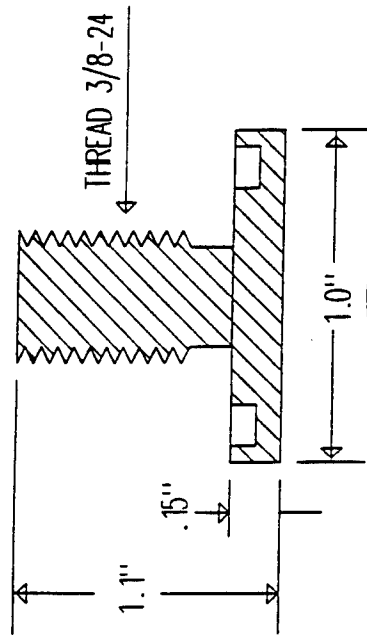
AL J-T BODY

VACUUM CAN (AL)



TOP PLATE (AL)

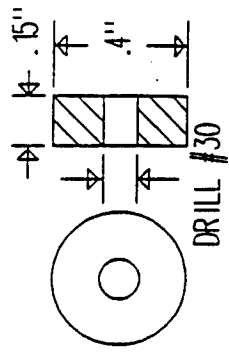




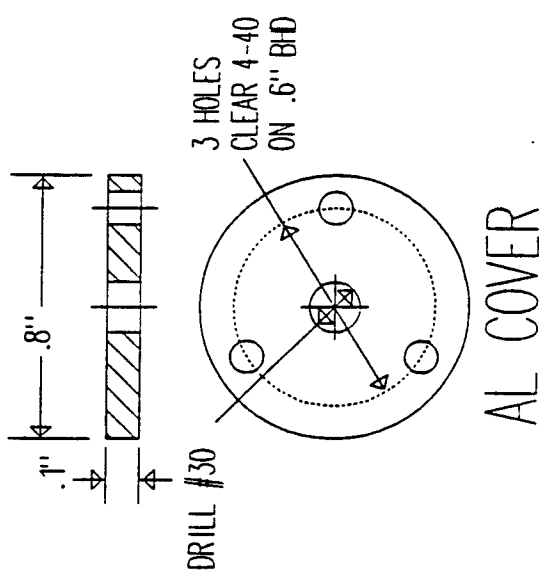
O-RING GROOVE
.9" O.D. BY .7" I.D.
.05" DEEP

BRASS

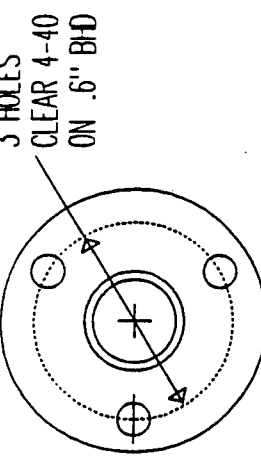
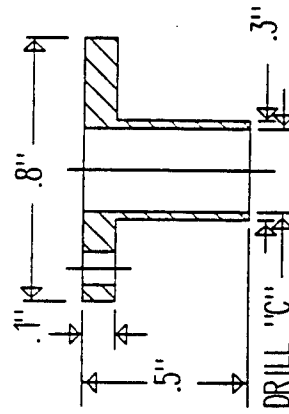
MAKE TWO FEEDTHROUGHS



AL SPACER



AL COVER



AL UPPER TUBE SOCKET

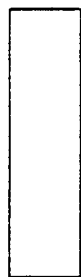
10/24/89 R.E. SARWINSK

MISC J-T PARTS

G 10 ROD
8" BY 1/8" DIAM



MAKE FROM S.S.
0.121" I.D.
0.14" O.D.



1 PC FROM S.S.
.20" BY 1/16" D



2PCS FROM S.S.
.26" BY 1/16" D

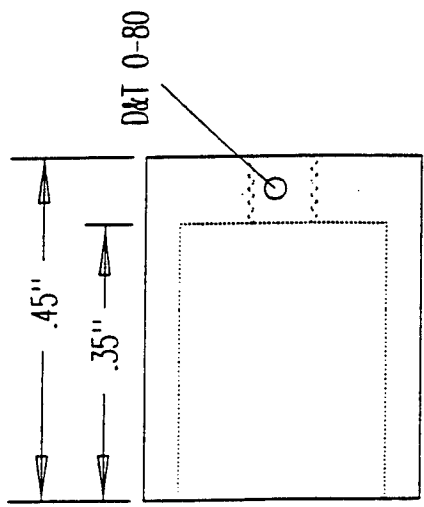


TABLE XVIII **Temperature Vs. Resistance Table**

For European Curve, Alpha = .00385

1° Celsius Increments

*C	Ohm	Diff.	*C	Ohm	Diff.	*C	Ohm	Diff.	*C	Ohm	Diff.	*C	Ohm	Diff.	*C	Ohm	Diff.
-200	18.49		-140	43.87	0.42	-80	68.33	0.41	-20	92.16	0.39	± 0	100.00	0.39	+ 60	123.24	0.38
199	18.93	0.44	139	44.28	0.41	79	68.73	0.40	19	92.55	0.39	+ 1	100.39	0.39	61	123.62	0.38
198	19.36	0.43	138	44.70	0.42	78	69.13	0.40	18	92.95	0.40	2	100.78	0.39	62	124.01	0.39
197	19.79	0.43	137	45.11	0.41	77	69.53	0.40	17	93.34	0.39	3	101.17	0.39	63	124.39	0.38
196	20.22	0.43	136	45.52	0.41	76	69.93	0.40	16	93.73	0.39	4	101.56	0.39	64	124.77	0.38
195	20.65	0.43	135	45.94	0.42	75	70.33	0.40	15	94.12	0.39	5	101.95	0.39	65	125.16	0.39
194	21.08	0.43	134	46.35	0.41	74	70.73	0.40	14	94.52	0.40	6	102.34	0.39	66	125.54	0.38
193	21.51	0.43	133	46.76	0.41	73	71.13	0.40	13	94.91	0.39	7	102.73	0.39	67	125.92	0.38
192	21.94	0.43	132	47.18	0.42	72	71.53	0.40	12	95.30	0.39	8	103.12	0.39	68	126.31	0.39
191	22.37	0.43	131	47.59	0.41	71	71.93	0.40	11	95.69	0.39	9	103.51	0.39	69	126.69	0.38
190	22.80	0.43	130	48.00	0.41	70	72.33	0.40	10	96.09	0.40	10	103.90	0.39	70	127.07	0.38
189	23.23	0.43	129	48.41	0.41	69	72.73	0.40	9	96.48	0.39	11	104.29	0.39	71	127.45	0.38
188	23.66	0.43	128	48.82	0.41	68	73.13	0.40	8	96.87	0.39	12	104.68	0.39	72	127.84	0.39
187	24.09	0.43	127	49.23	0.41	67	73.53	0.40	7	97.26	0.39	13	105.07	0.39	73	128.22	0.38
186	24.52	0.43	126	49.64	0.41	66	73.93	0.40	6	97.65	0.39	14	105.46	0.39	74	128.60	0.38
185	24.94	0.42	125	50.06	0.42	65	74.33	0.40	5	98.04	0.39	15	105.85	0.39	75	128.98	0.38
184	25.37	0.43	124	50.47	0.41	64	74.73	0.40	4	98.44	0.40	16	106.24	0.39	76	129.37	0.39
183	25.80	0.43	123	50.88	0.41	63	75.13	0.40	3	98.83	0.39	17	106.63	0.39	77	129.75	0.38
182	26.23	0.43	122	51.29	0.41	62	75.53	0.40	2	99.22	0.39	18	107.02	0.39	78	130.13	0.38
181	26.65	0.42	121	51.70	0.41	61	75.93	0.40	1	99.61	0.39	19	107.40	0.38	79	130.51	0.38
180	27.08	0.43	120	52.11	0.41	60	76.33	0.40				20	107.79	0.39	80	130.89	0.38
179	27.50	0.42	119	52.52	0.41	59	76.73	0.40				21	108.18	0.39	81	131.27	0.38
178	27.93	0.43	118	52.92	0.40	58	77.13	0.40				22	108.57	0.39	82	131.66	0.39
177	28.35	0.42	117	53.33	0.41	57	77.52	0.39				23	108.96	0.39	83	132.04	0.38
176	28.78	0.43	116	53.74	0.41	56	77.92	0.40				24	109.35	0.39	84	132.42	0.38
175	29.20	0.42	115	54.15	0.41	55	78.32	0.40				25	109.73	0.38	85	132.80	0.38
174	29.63	0.43	114	54.56	0.41	54	78.72	0.40				26	110.12	0.39	86	133.18	0.38
173	30.05	0.42	113	54.97	0.41	53	79.11	0.39				27	110.51	0.39	87	133.56	0.38
172	30.47	0.42	112	55.38	0.41	52	79.51	0.40				28	110.90	0.39	88	133.94	0.38
171	30.90	0.43	111	55.78	0.40	51	79.91	0.40				29	111.28	0.38	89	134.32	0.38
170	31.32	0.42	110	56.19	0.41	50	80.31	0.40				30	111.67	0.39	90	134.70	0.38
169	31.74	0.42	109	56.60	0.41	49	80.70	0.39				31	112.06	0.39	91	135.08	0.38
168	32.16	0.42	108	57.00	0.40	48	81.10	0.40				32	112.45	0.39	92	135.46	0.38
167	32.59	0.43	107	57.41	0.41	47	81.50	0.40				33	112.83	0.38	93	135.84	0.38
166	33.01	0.42	106	57.82	0.41	46	81.89	0.39				34	113.22	0.38	94	136.22	0.38
165	33.43	0.42	105	58.22	0.40	45	82.29	0.40				35	113.61	0.39	95	136.60	0.38
164	33.85	0.42	104	58.63	0.41	44	82.69	0.40				36	113.99	0.38	96	136.98	0.38
163	34.27	0.42	103	59.04	0.41	43	83.08	0.39				37	114.38	0.39	97	137.36	0.38
162	34.69	0.42	102	59.44	0.40	42	83.48	0.40				38	114.77	0.39	98	137.74	0.38
161	35.11	0.42	101	59.85	0.41	41	83.88	0.40				39	115.15	0.38	99	138.12	0.38
160	35.53	0.42	100	60.25	0.40	40	84.27	0.39				40	115.54	0.39	100	138.50	0.38
159	35.95	0.42	99	60.66	0.41	39	84.67	0.40				41	115.93	0.39	101	138.88	0.38
158	36.37	0.42	98	61.06	0.40	38	85.06	0.39				42	116.31	0.38	102	139.26	0.38
157	36.79	0.42	97	61.47	0.41	37	85.46	0.40				43	116.70	0.39	103	139.64	0.38
156	37.21	0.42	96	61.87	0.40	36	85.85	0.39				44	117.08	0.38	104	140.02	0.38
155	37.63	0.42	95	62.28	0.41	35	86.25	0.40				45	117.47	0.39	105	140.39	0.37
154	38.04	0.41	94	62.68	0.40	34	86.64	0.39				46	117.85	0.38	106	140.77	0.38
153	38.46	0.42	93	63.09	0.41	33	87.04	0.40				47	118.24	0.39	107	141.15	0.38
152	38.88	0.42	92	63.49	0.40	32	87.43	0.39				48	118.62	0.38	108	141.53	0.38
151	39.30	0.42	91	63.90	0.41	31	87.83	0.40				49	119.01	0.39	109	141.91	0.38
150	39.71	0.41	90	64.30	0.40	30	88.22	0.39				50	119.40	0.39	110	142.29	0.38
149	40.13	0.42	89	64.70	0.40	29	88.62	0.40				51	119.78	0.38	111	142.66	0.37
148	40.55	0.42	88	65.11	0.41	28	89.01	0.39				52	120.16	0.38	112	143.04	0.38
147	40.96	0.41	87	65.51	0.40	27	89.40	0.39				53	120.55	0.39	113	143.42	0.38
146	41.38	0.42	86	65.91	0.40	26	89.80	0.40				54	120.93	0.38	114	143.80	0.38
145	41.79	0.41	85	66.31	0.40	25	90.19	0.39				55	121.32	0.39	115	144.17	0.37
144	42.21	0.42	84	66.72	0.41	24	90.59	0.40				56	121.70	0.38	116	144.55	0.38
143	42.63	0.42	83	67.12	0.40	23	90.98	0.39				57	122.09	0.39	117	144.93	0.38
142	43.04	0.41	82	67.52	0.40	22	91.37	0.39				58	122.47	0.38	118	145.31	0.38
141	43.45	0.41	81	67.92	0.40	21	91.77	0.40				59	122.86	0.39	119	145.68	0.37

Note: At 100°C resistance is 138.50 ohms.

(DIN 43 760)

APPENDIX D

FINAL REPORT ON CERAMIC HONEYCOMBS FOR JOULE-THOMPSON CRYOCOOLER

by

Eric R. Kreidler
Daniel C. Sherman
Peter M. Anderson

Sponsor: CeramPhysics, Inc.
921 Eastwind Dr.
Suite # 110
Westerville, OH 43081

Contract No. CPI-89-003

OSURF Project No. 722276
OSURF Project NO. 722402

The Ohio State University
Department of Materials
Science and Engineering
107 Watts Hall
2041 College Road
Columbus, OH 43210

On this and the following page, the most significant results of Dan Sherman's M.S. Thesis entitled "Mechanical Properties of Niobia Doped Bismuth Sesquioxide" are summarized. The numbers in parentheses refer to pages in the thesis. A copy of the thesis is attached hereto, and this summary along with the thesis constitute the final report for the project.

Bismuth oxide is a complex material, having at least five crystalline structures. Although individual structures are reasonably well understood (p 15-20), the stability relationships among the phases are open to question especially when impurities such as Nb_2O_5 are present (p 20-25). In any event one of the phases, delta- Bi_2O_3 , has exceptionally high oxygen ion conductivity, can be stabilized by addition of Nb_2O_5 and other additives to low temperatures, and can be sintered to a nearly pore free state in complex geometries. These properties are all favorable for use of delta- Bi_2O_3 (hereafter referred to as BNO) as a solid state oxygen compressor.

The main question which this research addressed is whether BNO possesses sufficient mechanical strength to support the oxygen pressure differential required in a practical compressor. By comparing experimental modulus of rupture values to stresses calculated by finite element methods (p 121-125, 139-140), it has been found that at their present stage of development, BNO honeycombs would be able to sustain a maximum pressure differential of about 17 atmospheres at an operating temperature of 600°C (p 125). Pressures of 50 to 150 atmospheres are required. Therefore, the strength of BNO will have to be increased by a factor of 3 to 9 times for this application to be realized.

The most significant improvement achieved in this work resulted from a change in powder preparation method. Vibratory milling of calcined powder (rather than conventional ball milling) resulted in a two fold increase in modulus of rupture (p 94-95), an increase in sintered density from 95.0 to 98.3 % of theoretical (p 93) and a reduction in average sintered grain size from 26 to 15 micrometers (p 92).

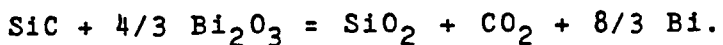
Several attempts were made to further improve the strength of BNO. These included; (A) addition of zirconia as a transformation toughening agent (p 106-112), (B) controlled precipitation of second phases from BNO (p 112-117), and (C) whisker strengthening (p 117).

Results of the zirconia additions were somewhat promising in that a strengthening effect was observed (p 108) despite the fact that the microstructures obtained were very poor. The microstructures showed that the zirconia was not well dispersed (p 110-111) and large pores were present (p 109). Numerous attempts to improve the microstructure of zirconia containing samples were unsuccessful. Although some toughening by zirconia was observed, this is not a promising direction to pursue because zirconia additions have a large negative effect on the electrical

conductivity of BNO. At 500°C the conductivity of pure BNO is about 0.009 (ohm cm)⁻¹ while the specimen showing the largest toughening effect had a conductivity of 0.001 (ohm cm)⁻¹ (p 113). This nearly ten fold decrease in conductivity is unacceptable.

The idea behind precipitation toughening was that since Bi₂O₃ has both tetragonal and monoclinic phases, and since tetragonal transforms to monoclinic on cooling, a toughening effect similar to that in partially stabilized zirconia might be possible. In this way toughening might be achieved without a large loss in conductivity since no zirconia would be added. Extensive annealing studies were done on BNO samples containing from 6.7 to 19.3 mole % Nb₂O₅. Tetragonal Bi₂O₃ was not observed to precipitate from BNO under any of the conditions studied (p 114) and no significant strengthening was observed (p 114).

Silicon carbide whiskers were incorporated into bar specimens in an attempt to strengthen BNO. This was unsuccessful due to a chemical reaction between Bi₂O₃ and SiC which is presumed to be



The resulting samples were melted (glassy), had foamed up, and did contain metallic bismuth (p 117). They could not be tested for strength.

Further work on BNO indicated a fracture toughness of 0.42 MPa/√m (p 118) which is lower than for most ceramics. High temperature modulus of rupture measurements (p 104-107) indicate that an 18% reduction in strength would occur at the operating temperature (ca 600°C) of a practical oxygen compressor. The reasons for this are not clear, but may be related to thermal shock effects. In any case the loss in strength is not catastrophic. Calculations of critical flaw sizes for failure (using observed modulus of rupture and toughness values) indicate that the grain sizes and porosity inherent in the microstructure are not the failure causing flaws. This suggests that large processing defects are responsible for failure (p 120-121) and some examples of such flaws are shown (p 116).

In summary, at its present state of development, BNO has 10 to 30% of the strength needed for a practical oxygen compressor. Conventional toughening mechanisms do not appear to be applicable, but reduction or elimination of large processing defects may lead to significant strength improvements, and possibly to a material capable of meeting the requirements for application in a solid state oxygen compressor.

MECHANICAL PROPERTIES OF NIOBIA DOPED BISMUTH

SESQUIOXIDE

A Thesis

Presented in Partial Fulfillment of the Requirements for the Degree
of Master of Science in the Graduate School of The Ohio State
University

By

Daniel Christopher Sherman B. S. Cer E., M. S. Cer. E.

* * * * *

The Ohio State University

1991

Master's Examination Committee:

Approved By

E. R. Kreidler

Erie R. Kreidler

P. Anderson

J.J. Lannutti

Advisor

Department of Material
Science and Engineering

THESIS ABSTRACT

THE OHIO STATE UNIVERSITY
GRADUATE SCHOOL

NAME: Sherman, Daniel Christopher QUARTER/YEAR: Summer '91

DEPARTMENT: Ceramic Engineering DEGREE: Master of Science

ADVISOR'S NAME: Kreidler, Eric R.

TITLE OF THESIS: Mechanical Properties of Niobia Doped Bismuth Sesquioxide.

Niobia doped bismuth oxide was studied for possible application as a solid electrolyte in a Joule-Thompson refrigeration system. The mechanical properties and microstructure of the material were found to be inferior to other structural ceramics. Several techniques were used in an attempt to improve the strength of this material but they resulted in an unacceptable decrease in the conductivity and/or in the mechanical strength. The microstructure was improved by optimizing processing variables.

The extrusion properties of the material were also examined. The material was extruded into honeycomb geometries. Problems of viscosity and flow were encountered that resulted in components that were not structurally sound. Adjustments to the die arrangement and the composition of the extrusion batch resulted in structurally sound honeycombs.

Eric R. Kreidler
Advisor's Signature

ACKNOWLEDGMENTS

I would like to extend my gratitude to my advisor, Dr. Eric Kreidler, for his insight and knowledge and the confidence he inspired in me. To Fred Clark, Bill Lawless and Ken Scheel I can only begin to thank you for your support and contributions to this effort. To the Strategic Defense Initiative Office, I would like to impart my thanks for financially supporting this research. I express my thanks and love to my parents for the opportunity and support they gave me throughout my college career. I would like to thank all my friends who have been there when I needed a break and sometimes when I didn't. Without you, I may might never have achieved this goal or had the experiences I did. A special thanks goes to Dr. Anderson who was more than a co-advisor, but a friend whom I could talk to. Last, I would like to thank Jeff Moser for his time and effort expended toward the completion of my thesis. I only hope that sometime I can repay him the effort he put forth.

VITA

September 21, 1966 Born - Cleveland, Ohio

1988 B. S. The Ohio State
University
Columbus, Ohio

1988 - Present Research Associate,
Department of
Ceramic Engineering,
The Ohio State University,
Columbus, Ohio

FIELD OF STUDY

Major Field: Ceramic Engineering

TABLE OF CONTENTS

ACKNOWLEDGMENTS	ii
VITA	iii
LIST OF TABLES	vii
LIST OF FIGURES	viii
LIST OF PLATES	xiii
CHAPTER	PAGE
I. INTRODUCTION	1
II. THEORY	8
Basic Concepts for Ion Transport	8
Phase Diagram for Bismuth Sesquioxide (Pure)	15
Phase Stability in the Bi_2O_3 - Nb_2O_5 System	20
Porosity Effects on Mechanical Properties	26
Brittle Fracture	33
Grain Size Effect on Mechanical Properties	35
Temperature Dependence of Strength	39
Agglomeration Effects	40
Toughening Mechanisms in Ceramic Composites	46
Crack Deflection Processes	49
Transformation Toughening	55

III EXPERIMENTAL PROCEDURE	60
Raw Materials	60
Powder Preparation	60
Composite Processing	63
Precipitation Toughened Specimen Preparation	66
Mechanical Testing	70
High Temperature Mechanical Testing.	71
Fracture Toughness	72
Honeycomb Extrusion	74
Characterization Techniques	81
IV RESULTS	85
Particle Size Reduction	85
Particle Size Effect on Strength	91
Extrusion of Honeycomb Geometry	95
Sintering of Honeycomb Components	97
High Temperature Modulus of Rupture.	104
Transformation Toughening	106
Precipitation Toughening	112
Whisker Reinforcement	117
Fracture Toughness	118
Finite Element Analysis	121
V DISCUSSION	126
Particle Size Reduction	126
Extrusion of Honeycomb Geometry	130
Densification of Honeycomb Samples	131
High Temperature Modulus of Rupture.	132
Fracture Toughness	134
Transformation Toughening	135
Precipitation Toughening	137
Whisker Reinforcement	138
Finite Element Analysis	139

VI FUTURE WORK	141
APPENDICES	143
A. Homogenizer Plate	143
B. Raw Data for Modulus of Rupture Measurements Samples made from ball milled powder	144
C. Raw Data for Modulus of Rupture Measurements Samples made from vibratory milled powder	146
D. Flow restrictor plate	148
E. Raw Data for Modulus of Rupture Measurements High Temperature Tests	149
F. Raw Data for Modulus of Rupture Measurements Transformation Toughened Samples	151
G. Raw Data for Modulus of Rupture Measurements Precipitation Toughened Samples	157
REFERENCES	161

LIST OF TABLES

TABLE	PAGE
1. Initial sintering schedule for BNO samples	66
2. Sintering schedule as determined by rate controlled sintering studies done by Kenny and Associates.	67
3. Modified RCS sintering schedule to accommodate the samples with the lower niobia contents.	69
4. Particle size as a function of milling time for ball and vibratory milling techniques.	87
5. Results of x-ray analysis of annealed specimens with different compositions in the bismuth-niobia system.	114
6. Calculated values for failure causing flaw sizes in several of the materials tested.	120
7. Measured values for the cell dimensions in the sintered honeycombs.	125

LIST OF FIGURES

FIGURE	PAGE
1. Energy Barrier Diagram for Ion Motion	11
2. Structure of Beta phase projection on the (001) plane . . .	18
3. Phase diagram of the system Nb_2O_5 - Bi_2O_3 as obtained by Roth and Waring	21
4. Revised phase diagram in the Nb_2O_5 - Bi_2O_3 system by Powers	23
5. Subsolidus phase diagram as determined by Powers . . .	25
6. Relative elastic modulus versus porosity	29
7. Effect of porosity on strength	31
8. Strength of compacts produced by different processing methods	32
9. Crack penetrating through the thickness of a large plate .	34
10. Grain size versus strength	37
11. Modulus of rupture versus temperature for different grades of BeO	41

12. Green density as a function of aggregate content.	43
13. Magnitude of the ratio of the stress to move a semi-elliptical crack and the stress to move a straight crack versus r_0/C	48
14. The effect of variation in interparticle spacing and crack interaction on the strength	49
15. Examples of particle-crack interaction	51
16. Relative toughness as predicted from crack deflection model including interparticle spacing	53
17. Crack deflection and crack bowing predictions for relative toughness	54
18. The effect of temperature on the toughness of a transformation toughened composite	56
19. Effect of zirconia stabilizer on the toughness of an $\text{Al}_2\text{O}_3\text{-ZrO}_2$ composite	58
20. Particle size and concentration effect on toughness.	58
21. Toughness as a function of precipitate size	58
22. Mechanical splitting device used for producing representative powder samples.	63
23. Mechanical testing design used for modulus of rupture testing. Four point bend design.	71
24. Experimental arrangement used for high temperature modulus of rupture tests.	72
25. Graph of the exponential function $F(a/b)$ used in determining the fracture toughness on notched beam specimens	75

26. Diagram of a pug mill	79
27. Experimental design used for the extrusion of honeycombs	80
28. SEM photograph of BNO powder showing extensive agglomeration	86
29. Particle size versus milling time for vibratory and ball milling techniques	89
30. Typical ball milled powder showing a typical particle size distribution	90
31. Typical vibratory milled powder showing narrow particle size distribution	90
32. Microstructure of bars produced from ball milled powder	92
33. Microstructure of bars produced from vibratory milled powder	92
34. Porosity in sintered bars produced from ball milled powder	94
35. Porosity in bars produced from vibratory milled powder	94
36. Sintering arrangement placing the honeycomb in hydrostatic compression	99
37. Sintering arrangement reducing component-setter friction	99
38. X-ray pattern from BNO material calcined at 700°C showing the monoclinic Bi_2O_3 phase	100

39. X-ray pattern of material calcined at 800°C showing the cubic phase	101
40. TGA curve for honeycomb material showing weight loss as a function of temperature. Material was dried thoroughly before testing.	103
41. Optical micrograph showing grain size and porosity of a honeycomb sample produced from powder calcined at 700°C	103
42. Optical micrograph showing grain size and porosity of a honeycomb sample produced from fully calcined material	105
43. Strength of sintered BNO bodies as a function of temperature	107
44. Strength versus weight percent zirconia	108
45. Optical photograph of a BNO bar containing 20 wt. % zirconia	110
46. Photograph showing an area of high zirconia concentration in BNO doped with 11.6 wt.% zirconia	110
47. Optical photograph indicating BNO rich areas encompassed by porosity.	111
48. Optical photograph of a BNO specimen doped with zirconia	111
49. Conductivity versus temperature for pure BNO and BNO doped with zirconia.	113
50. Surface void causing failure in bismuth doped with 16.3 mole % niobia	116

51. Flaw initiating failure in bismuth doped with 16.3 mole % niobia	116
52 Scanning electron micrograph of a typical fracture surface obtained during fracture toughness measurements.	119
53. Honeycomb geometry and dimensions	122
54. Stress concentration factor as a function cell geometry .	124
55. Homogenizer Plate	143
56. Flow restrictor plate	148

LIST OF PLATES

I. Honeycomb Geometry	7
---------------------------------	---

CHAPTER I

INTRODUCTION

Several oxide systems have been discovered that have extremely high oxygen conducting properties. The primary application of these materials are as oxygen sensors, although several other innovative and exciting applications are currently under consideration. Fuel cells, oxygen enrichers and oxygen pumps are other applications in which these materials may have an important role to play.

The possibility of a cooling system based on a solid state oxygen pump has been proposed and is theoretically feasible. This pump would use oxygen as the cooling fluid much like a household refrigerator uses freon. The cooling system would contain no moving parts and use a Joule-Thompson expansion valve to produce a system capable of cryogenic temperatures. The solid state electrolyte would be used to produce a stream of pure oxygen

that would be pressurized and passed through a Joule-Thompson expansion valve.

There are several advantages to this type of refrigeration system. The system would contain no moving parts such as a mechanical pump, eliminating the possibility of failure due to mechanical problems. A solid state oxygen pump would produce pure oxygen which reduces the concentration of impurities in the gas stream to essentially zero. This is important since a common failure of cryocoolers is a stoppage of flow due to freezing of impurities such as oil from a mechanical compressor. The electrolyte material chosen for study in this research was niobia doped bismuth oxide.

Takahashi et al.¹ have studied several bismuth oxide systems and found that a dopant level of approximately 15 mole percent niobia gave the optimum oxygen conductivity. The oxygen conductivity is $1.1 \times 10^{-2} \Omega^{-1} \text{cm}^{-1}$ at 500°C, this value is over ten times greater than conventional zirconias. In contrast, this material is also an excellent electronic insulator. It has very low electronic conduction in the stabilized δ -form. Furthermore, the oxygen conductivity of bismuth oxide is not dependent on the partial pressure of oxygen in the oxygen source. This is an

important consideration in the design of the cooling system. A cooling system designed to use the atmosphere as the oxygen source (open system) or a self contained cooling system (closed) is possible without correction for the properties of the electrolyte.

A major concern in the operation of this device will be the heat produced due to resistance in the solid electrolyte. This will be significant not only due to structural considerations, but also for thermodynamic reasons. The cooling capabilities of a system will be dependent on several factors, one of which will be the ability of the system to remove or dissipate heat effectively. Bismuth sesquioxide (Bi_2O_3) has a thermal conductivity greater than the conventional zirconias. This allows a greater rate of heat dissipation during operation.

The final reason bismuth sesquioxide was chosen for this study is that it has a very low sintering temperature. In comparison to typical zirconia materials which have sintering temperatures of approximately 2000 °C, the sintering temperature of bismuth sesquioxide is very low. Bismuth sesquioxide has a melting point of approximately 900°C depending on the composition. This criteria is important because the complicated geometry of the oxygen compressor requires special sintering

arrangements limiting the maximum temperature.

In order to produce a sufficient amount of oxygen by utilizing the solid electrolyte, several design criteria have been established. The power requirements can be approximated using Faraday's law of electrolysis,

$$\frac{dn}{dt} = I/ZeN_0 \quad (1)$$

where dn/dt is the transport of oxygen in moles, I is the current, N_0 is Avogadros' number and Ze is the charge on the ion being transported. Lawless² determined that in order to produce a refrigeration of 1W at 90K, an oxygen mass-flow rate of 30 mg/s is needed. Following Faraday's law, a current of 300A is needed to produce this mass-flow rate.

The large current needed is a factor that must be reduced because of power requirements. A practical solution would be to align several units in a series, such as 20 units at a current level of 15 A each. The resistance of the total circuit is dependent on the resistance of each unit. Equation 2 relates the total circuit resistance, R_{eq} , to the individual units' resistance, R_k .

$$R_{eq} = \sum 1/R_k \quad (2)$$

A series of 20 or 30 units would have a significant amount of resistance. If a parallel arrangement is used, the resistance can be considerably reduced. The resistance of a parallel set of resistors, R_k , may be related to a total resistance, R_{eq} , by

$$1/R_{eq} = \sum 1/R_k \quad (3)$$

The only practical way to reduce the resistance is to have a multitude of resistors in parallel.

The considerations mentioned above require a specific geometry in order to produce a useful compressor. The structure must consist of several units in series with each unit having low resistance. Having a multitude of cells in parallel with each other in each unit would produce the desired effect. Achieving the parallel arrangement is the most difficult requirement to satisfy. The honeycomb geometry satisfies the above criterion. Plate 1 is representative of the honeycomb geometry. To produce oxygen, the walls of the honeycomb will be platinized to allow a current to be passed across the material. Alternating rows at both ends will be blocked off with the opposing ends of the blocked off channels open. This creates a physical barrier between the two ends of the honeycomb by which a pressure can be maintained. When a current is applied to the material, oxygen will pass from one end of the

honeycomb through the channel walls to the other. This arrangement satisfies the criteria of several low resistance cells in parallel with each other. The low sintering temperature of the BNO material gives it the unique ability to be formed into the honeycomb shaped geometry shown in Plate 1. The honeycomb geometry is the only practical way to achieve the high rate of oxygen production while maintaining a reasonable power demand and is essential to the design of a cryocooler system.

The objective of this research was to produce an oxygen compressor based on a cellular monolith (honeycomb) structure and the highly conductive bismuth oxide material. A design following the above criteria would satisfy all the geometrical and mechanical requirements imposed on the oxygen compressor.

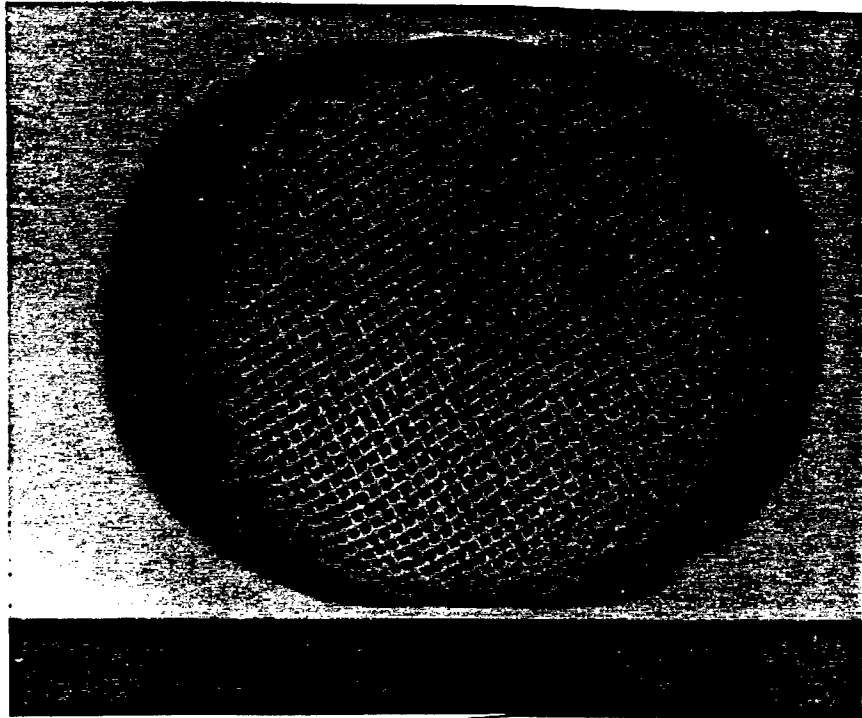


Plate I: Honeycomb geometry

CHAPTER II

THEORY

BASIC CONCEPTS FOR ION TRANSPORT

Diffusion of ions in a solid takes place due to a potential gradient of some type acting on the migrating species. Fick's law relates the concentration gradient parallel to the diffusion direction to the flux of atoms in the same direction. Fick's first law may be stated for one-dimensional diffusion as

$$J = -D(\partial c / \partial x) \quad (4)$$

where J is the flux of atoms diffusing in the x -direction, D is the diffusion coefficient and c is the concentration of diffusing atoms at the plane (per unit volume). J has the units of $(\text{time-area})^{-1}$, $\partial c / \partial x$ has the units $(\text{volume-length})^{-1}$ so D has the units $(\text{area})/(\text{time})$. For diffusion under the influence of a force such as an electric field or a thermal gradient, Fick's first law can be

written in the form of

$$J = -D^* (\partial c / \partial x) \quad (5)$$

where

$$D^* = D - c \langle v \rangle_f / (\partial c / \partial x) \quad (6)$$

Here c is the concentration of moving ions and $\langle v \rangle_f$ is the drift velocity under the influence of the force F . Combining Equations (4) or (5) with the equation of continuity

$$\partial c / \partial t = -\nabla \cdot J \quad (7)$$

where ∇ is the gradient operator and t is time, gives Fick's second law

$$\partial c / \partial t = \nabla \cdot (D \nabla c) \quad (8)$$

In one dimension when D is independent of x , Equation (8) reduces to

$$\partial c / \partial t = D \partial^2 c / \partial x^2 \quad (9)$$

The continuity equation states that the change in concentration in a specified volume is equal to the net flow into that volume.

Ionic conduction in solids can occur only under conditions that allow the movement of the ion through the lattice. Because of the dense matrix of other atoms in a solid, there are two conditions that must be met in order for ionic conduction to

proceed. The first requirement is that an empty site must be present in the direction of travel in order that the mobile ion can occupy it. The site can be either a vacancy or an interstitial position. On a macroscopic scale, the number of ions contributing to conduction must be smaller than the number of available sites. The second requirement is that the free energy of each successive jump is energetically favorable, i.e. the motion of the ion is not impeded.

Looking at the basic formalism for an atomistic jump with no driving force operating on the atom, the possibility of a jump in either the forward or reverse direction is equally probable. Figure (1a) indicates this type of arrangement. The energy barrier opposing motion is identical in the forward and reverse directions. This symmetry is the reason for the identical probabilities of motion in either direction.

The application of a driving force upsets the balance of the energy barriers. The resultant energy barrier diagram is represented in Figure (1b). The driving force F makes the probability of a jump in the forward direction more likely than a jump in the reverse direction. The force is equal to

$$F = zeE \quad (10)$$

where ze is the charge on the particle, and E is the strength of the

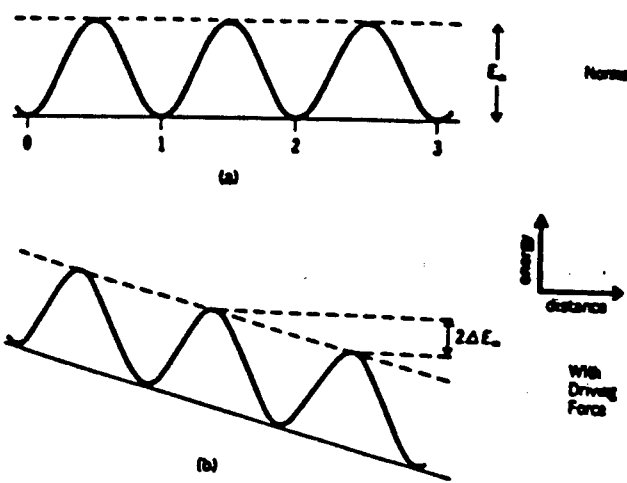


Figure 1) a) Energy well with no outside force acting on the barrier. b) Energy well with an applied force.
Ref (3).

electric field. The resulting drop in the potential energy from a unit jump, λ , in the forward direction is $-\lambda F$. Therefore, the change in free energy of the atom is equal to

$$\Delta G = G_b - G_a \quad (11)$$

where G_b is the energy before the jump and G_a is the energy after the jump. G_a is lowered by an amount equal to

$$G_a = G_b - \lambda F \quad (12)$$

Substituting equation (12) into (11) the change in free energy from a forward jump is $-\lambda F$.

The energy barrier height is equal to the difference between

the energy at the lattice site and the energy when the atom is at the midpoint of the jump or $\frac{1}{2}\lambda$. The atom will gain a energy $\Delta E_m = \frac{1}{2}\lambda F$ when it moves to the "saddle" point in the presence of a force F . The energy required to move the atom to the saddle point in the lattice is $G_m = G_a - \Delta E_m$, where G_{m0} is the original barrier height in the absence of an applied force.

The number of times the ion attempts to jump the barrier, jump frequency Γ , is proportional to $\exp(-G_m/kT)$. The basic equation then becomes

$$\Gamma_f = \Gamma_0 \exp(\Delta E_m/kT) \quad (13)$$

where Γ_f is the jump frequency in the forward direction, Γ_0 is the jump frequency when the force in not present, T is the temperature and k is the Boltzman constant. When kT is much larger than ΔE_m , which is the case for normal ionic conductors, the equation reduces to

$$\Gamma_f = \Gamma_0 (1 + \epsilon) \quad (14)$$

where ϵ is much smaller than 1 and

$$\epsilon = \Delta E_m/kT = \lambda z e E/2kT \quad (15)$$

Using this equation it can be shown that this analysis holds for any force acting on the atom such as a chemical or electrical

potential³.

Solid electrolytes are usually under the influence of an electric field. Relating Fick's first law with the flow of charged particles through a unit area in a unit time Equation (16) is obtained.

$$j_i = n_i z_i e v \quad (16)$$

n_i is the number of charged particles per volume with a drift velocity v and $z_i e$ is the charge per particle. The electrical conductivity is defined by

$$\sigma = \frac{j}{E} \quad (17)$$

where E is the applied electric field. Combining Equations (16) and (17)

$$\sigma = n_i z_i e (v/E) \quad (18)$$

The ratio of drift velocity to the electric field is the mobility.

$$\mu_i = v_i/E \quad (19)$$

The conductivity is then defined as the combination of Equations (18) and (19)

$$\sigma = n_i z_i e \mu_i \quad (20)$$

The ion must overcome an energy barrier if it is to move through the lattice under the driving force of an electric field.

Combining Equations (3) and (16) and relating the jump frequency, Γ_0 , to the jump distance λ and vibrational frequency v , Equation (21) is obtained.

$$j_{\text{forward}} = z \epsilon n \lambda v \left[\exp\left(\frac{-G_b + z \epsilon E \lambda / 2}{kT}\right) \right] \quad (21)$$

The reverse flux is

$$j_{\text{reverse}} = z \epsilon n \lambda v \left[\exp\left(\frac{-G_b - z \epsilon E \lambda / 2}{kT}\right) \right] \quad (22)$$

The total flux in the forward direction is

$$j_{\text{total}} = j_{\text{forward}} - j_{\text{reverse}} = 2 z \epsilon n \lambda v \left[\exp\left(\frac{-G_b}{kT}\right) \right] \left[\sinh\left(\frac{z \epsilon E \lambda}{2kT}\right) \right] \quad (23)$$

Substituting typical values of E , λ and T , the value for the sinh portion is small and Equation (23) reduces to

$$j_{\text{total}} = 2 \left(\frac{n v \lambda^2 z^2 e^2}{kT} \right) (e^{-G_b/kT}) E = \sigma E \quad (24)$$

This equation is usually generalized to the form

$$\sigma = C/T \exp(-E/RT) \quad (25)$$

Most ionic conductors follow this type of Arrhenius behavior for ionic conductivity.

PHASE DIAGRAM FOR BISMUTH SESQUIOXIDE (PURE)

The polymorphism of bismuth oxide has received a considerable amount of study in recent years. The exceptionally high ionic conductivity of the material in the high temperature form has generated a great amount interest. The high temperature form is that of a defect fluorite crystal structure. This defect structure has provided a wide variety of excellent ionic conductors. Along with bismuth based materials, ZrO_2 , CeO_2 and ThO_2 -based materials have shown the high ionic conductivity characteristic of fast ion conductors. The basis for the exceptional conductivity is in the defect crystal structure of the material.

Determining a phase diagram for bismuth oxide is complicated by the fact that some of the polymorphs can be obtained only by the careful control of processing and are affected by small additions of impurities. Levin and Roth et. al. (4, 5) have studied pure Bi_2O_3 and determined that the low temperature form is a monoclinic, pseudo-orthorhombic phase (α - Bi_2O_3). The low temperature monoclinic form is stable below 730 ± 5 °C. At 730 °C, the monoclinic phase transforms to the high temperature face-centered cubic phase.

The FCC phase remains stable until the melting temperature

of 825°C is reached. Levin and Roth found that if the sample is heated to a temperature below 745°C or rapidly to higher temperatures, then, upon cooling, the monoclinic form will not appear until approximately 700°C . Along with the phase transformation to the face centered cubic form, Levin and Roth obtained a volume expansion 6.9%. Harwig et. al.⁶ determined the spacegroup of the low temperature monoclinic phase to be $\text{P}2_1/\text{c}$ with b as the unique axis. The structure consists of layers of bismuth atoms at $X = 0$ and at $X = 0.5$ parallel to the (100) plane. The layers are separated by oxygen atoms arranged in sheets. Harwig also observed strings of vacancies in the oxygen sublattice in the $\langle 001 \rangle$ direction. The monoclinic form can also be obtained by slow heating of a body-centered cubic phase or the slow cooling of a tetragonal phase⁵.

The β -phase (tetragonal) can be obtained by quenching molten Bi_2O_3 or by heating Bismuthite ($\text{Bi}_2\text{O}_3 \cdot \text{CO}_2$). Malmros⁷ reported the β -phase to have the $\text{P}42_1\text{c}$ space group with lattice constants of $a = 7.7425$ and $c = 5.613$ Å. Sillen determined the space group to be of the $\text{P}4\bar{1}\text{b}2$ type. Both space groups limit the possible

reflections that can occur. The space group $P\bar{4}b2$ only allows the $h01$ reflection, where $h = 2n$. However, the 301 reflection is observed in the X-ray pattern. This invalidates the $P\bar{4}b2$ space group. Khachaturyan⁸ predicted the structure of the β -phase to be of the $P42_1c$ space group by ordering and Pseudo-Jahn-Teller instability. Figure 2 shows the projection of the β -phase on the (001) plane according to Sillen⁹. Defects are seen in the $\langle 111 \rangle$ direction in the fluorite subcell but Malmros also found channels in the $\langle 001 \rangle$ direction at $0,0,z$ and $\frac{1}{2},\frac{1}{2},z$. The channels are formed by voids along the edge of distorted oxygen cubes. The true form of the β -phase is still under investigation but the widely accepted space group is $P42_1c$.

A transition from the high temperature δ -phase or from the melt to a bcc phase, γ -phase, may be observed at $639^{\circ}C$ upon cooling. The γ -phase has been described as a metastable bcc form (sillenite). This phase has been studied by several authors and each has supplied questionable results. Sillen⁹ has suggested two different models for the γ -phase with one being

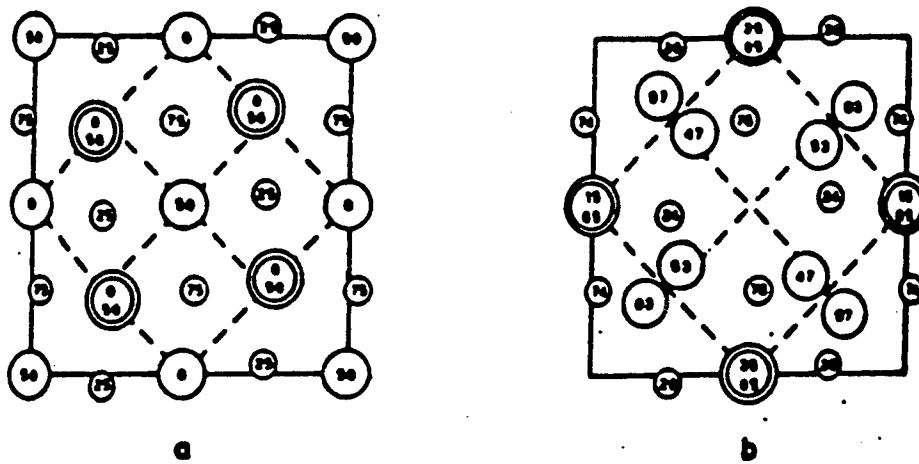


Figure 2: Structure of the Beta phase projected on the (001) plane according to a) Sillen⁹ and b) Harwig¹⁰. The position parameters in the <001> direction are multiplied by 100.

contaminated by metal ions such as Si, Fe or Al. The pure bismuth oxide phase was determined to be a cell containing $\text{Bi}_{24}\text{O}_{36}$. The Bi atoms are in fourfold coordination with the oxygen with the oxygen

forming octahedra around (000) and $\frac{1}{2}, \frac{1}{2}, \frac{1}{2}$. Schumb and Ritner¹¹

determined the cell parameter to be 10.245 Å for the unit cell containing $\text{Bi}_{26}\text{O}_{39}$. Schumb and Ritner have indicated that the unit cell contains the $\text{Bi}_{26}\text{O}_{39}$ structure due to isomorphism with several bismuth oxides of the form $\text{M}_2\text{Bi}_{24}\text{O}_{39}$. The two structures would be identical inasmuch as the bismuth ions would occupy the center position where the impurity ion is normally located. Other

materials incorporating the impurity ions Ge and Fe and forming the compounds $\text{Bi}_{12}\text{GeO}_{20}$ and $\text{Bi}_{25}\text{FeO}_{40}$ have been studied. These crystallize in the space group I23 and are isomorphous. The Bi_2O_3 host lattice forms a cage type structure where the small metal ions reside in a tetrahedral coordination with oxygen ions. Most of the literature has agreed on one point and that is that the γ -phase is a bcc phase with a structure very similar to that of the impure phase.

The structure gaining the most attention these days is the high temperature face-centered cubic form (δ -phase). This phase exhibits exceptionally high oxygen conduction due to its defect nature. The defects giving rise to the high conductivity are oxygen vacancies. These vacancies are caused by the fact that for stoichiometric Bi_2O_3 in the fluorite (δ) structure the number of oxygen atoms per Bi atom is 1.5. This gives rise to a 25% vacancy population in the δ -phase. Pure Bi_2O_3 can be converted to the δ -form by heating the monoclinic form to temperatures above 730°C . The bcc γ -phase and the β -phase can also yield the δ -phase by heating to 640°C and 660°C respectively. The δ -phase can be stabilized to room temperatures by the addition of large amounts of metal ions.

Sillen⁹ originally defined the lattice as a simple cubic structure with a Pn3m space group and a lattice constant of 5.66Å. The model contained ordered oxygen vacancies in the <111> direction. His work has been disputed later by Harwig et. al.⁶. Harwig et. al. have proposed a lattice with the space group Fm3m and a lattice constant of 5.66Å. The fcc structure was proposed as a CaF₂ structure with a high degree of oxygen defects. Both models have the bismuth atoms on the lattice of a fcc cube and differ only in the positions of the oxygen atoms. The next section discusses further work on the high temperature structure of samples stabilized with metals ions.

PHASE STABILITY IN THE Bi₂O₃ - Nb₂O₅ SYSTEM

The phase diagram for the system Bi₂O₃ and Nb₂O₅ has been extensively studied by several authors. As previously noted, the stability of the high temperature phases can be increased by the addition of a metal ion. Figure 3 shows the published phase diagram according to Roth And Waring¹². The most notable feature of this diagram is that the δ-phase (Css on phase diagram) can be stabilized down to approximately 600°C by the addition of 19% Nb₂O₅. The increase in the niobia content also increases the

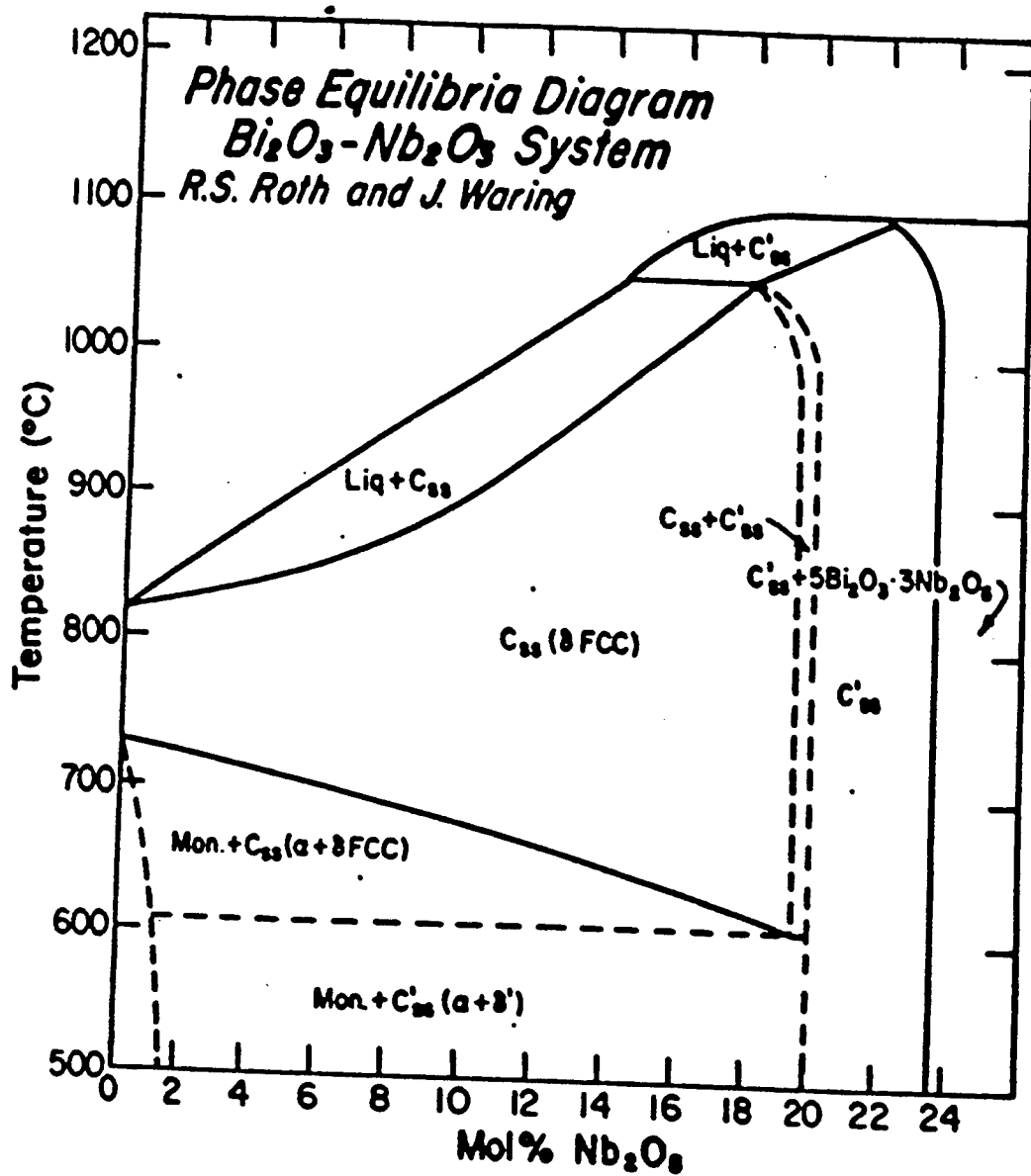


Figure 3: Phase diagram of the system $\text{Bi}_2\text{O}_3\text{-Nb}_2\text{O}_5$ as obtained by Roth and Waring. Ref. (12).

stability range up to a maximum at approximately 1020°C.

Increasing the amount of Nb_2O_5 past approximately 18% at elevated temperatures results in the formation of a C'ss + Css region. This region is only on the order of 1 mole percent or less in width and leads into a single phase C' region. The C' phase is a tetragonal phase similar to the C phase as determined by Zhou, Jefferson and Thomas¹³. Because of the similarity between the δ -phase and C', x-ray diffraction analysis is not sufficient to differentiate the two phases. Zhou, Jefferson and Thomas used high resolution electron microscopy to determine the actual parameters of the two phases. The C' phase is a more ordered structure than the δ -phase. It follows that the ionic conductivity of this phase would be smaller than the more disordered δ -phase.

According to the published phase diagram, the δ -phase is only stable down to 600°C. The C' phase is stable down to room temperature. Powers¹⁴ determined a phase diagram somewhat different from the published version (Figure 4). The δ -phase could be stabilized down to approximately 525°C by the addition of approximately 14 percent Nb_2O_5 . The region of stability for the C' phase is shifted to the right to between 21 and 23.5 percent

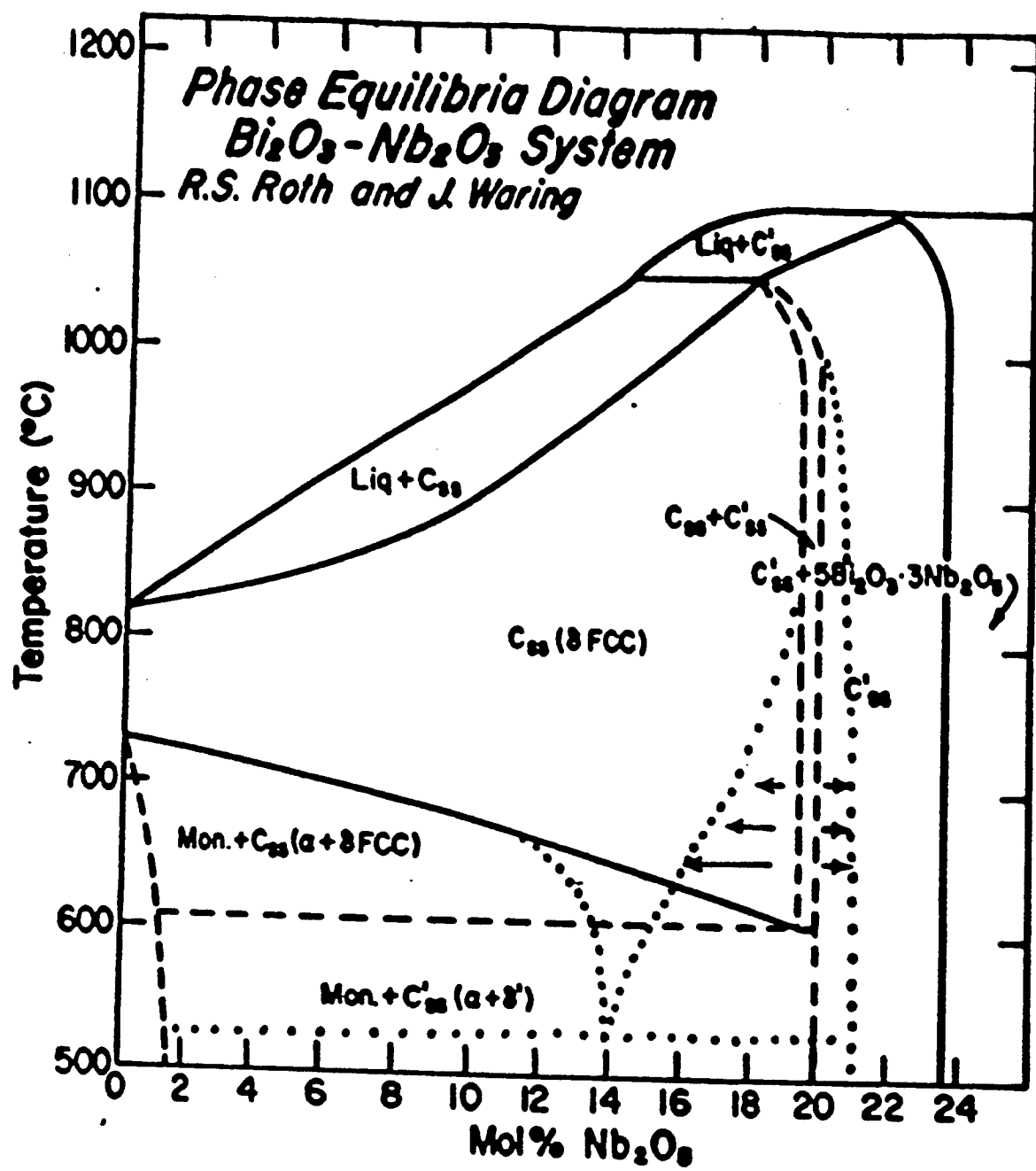


Figure 4: Revised phase diagram in the $\text{Bi}_2\text{O}_3\text{-Nb}_2\text{O}_5$ system by Powers. Ref. (14), dotted curves represent revisions by Powers.

niobia. The area of stability for the two phase region containing C_{ss} and C'_{ss} has been enlarged considerably by Powers to include a niobia range from 14 to 21 percent.

The proposed changes suggested by Powers are the result of quench studies. Figure 5 shows the subsolidus phase diagram and shows several interesting features. The most striking feature is the stability of the δ -phase down to room temperature. The phase has a range of approximately 1 mol.% centered around 14 mol.%. Another difference between Roth and Waring and Powers is the stability of the single phase region, C_{ss} , above 550°C. According to Roth and Waring this should be a two phase region between the monoclinic and C phases. This discrepancy could be due to the different processing between the sample prepared by Powers and Roth and Waring. Powers indicated that the δ -phase was preferentially formed during a sintering step prior to the quench of the material. This can account for the presence of the monoclinic phase in Roth and Warings' work and the systematic absence of the monoclinic phase in Powers' work. The heat treatment of the material is very important as the metastability of the δ -phase upon supercooling is required.

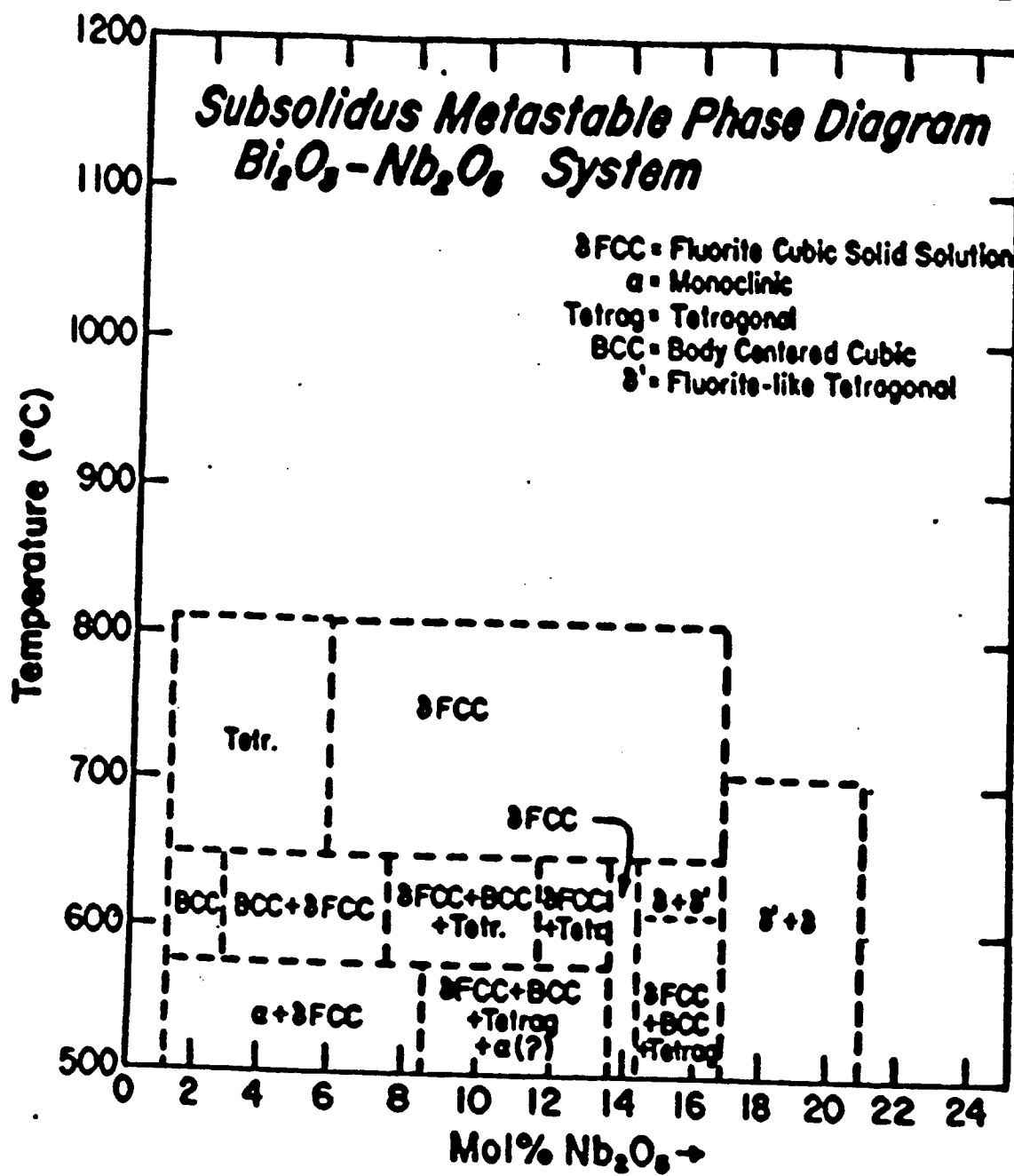


Figure 5: Subsolidus phase diagram in the $\text{Bi}_2\text{O}_3\text{-}\text{Nb}_2\text{O}_5$ system as determined by Powers. Ref. (14).

POROSITY EFFECTS ON MECHANICAL PROPERTIES

The effects of porosity on the physical properties of ceramics have been the subject of many studies. The objective of these studies has been the optimization of forming and sintering procedures for production of ceramic components that are structurally reliable. The difficulty in producing a generalized relationship between porosity and structural integrity is that changes in composition and processing produce changes in grain size, fracture toughness and other features besides porosity. These changes in microstructure can affect the structural properties of the ceramic. It is therefore difficult to evaluate the effect of porosity alone on the structural properties of a material because several other factors may be influencing the results.

The two limiting cases for porosity are: (1) the continuous phase is the solid phase with isolated pores and (2) the pores are interconnected with only a minimal amount of point contact between the solid phase. The former structure is reviewed due to the fact that most ceramic components are of the continuous solid type. The isolated pores in a solid are indirect sources of fracture. Evans et al.(15, 16) have determined that the voids themselves usually do not induce a sufficient stress

intensification to permit the fracture from the void surface. The voids produce a stress field that interacts with flaws close to the pore to produce a fracture. These flaws include other voids, microcracks and inclusions. The dependence of mechanical properties on porosity is highly dependent on the size, shape and distribution of pores throughout the material. The dependence of mechanical properties on porosity has been studied for several systems.

Fryxell and Chandler¹⁷ used three equations to describe their data on the effect of porosity on Young's modulus of sintered BeO.

$$E = E_0 (1-bP) \quad (26)$$

$$E = E_0 e^{-bP} \quad (27)$$

$$E = E_0 [1 + AP/(1-(A+1)P)] \quad (28)$$

where E is Young's Modulus at a porosity P and b and A are constants. Equation (26) describes the relationship satisfactory at low values of P , where the voids are isolated. Equation (27) is an exponential function proposed by Spriggs^(18,19) and Equation (28) is a semiempirical form from Hasselman²⁰ that takes into account the boundary condition that at $P = 1$, $E = 0$ and at $P = 0$, $E = E_0$. Fryxell and Chandler obtained a better fit to their data using Equation (28).

Coble and Kingery²¹ studied the effect of porosity on the relative elastic modulus for sintered alumina. Figure 6 shows that their data confirms the Mackenzie²² relationship. Mackenzie's relationship is a different form of Equation (28) identified by Hasselman.

Hunter and Graddy²³ studied the porosity dependence of elastic modulus on porosity for polycrystalline cubic Lu_2O_3 . The porosity ranged from 4 to 32 percent. Using a least squares fit, the data were fit to the empirical linear equation of Fryxell and Chandler (Equation 26). The data fit the linear relationship with 3.7 and 4.0 percent coefficients of variation. Dean and Lopez²⁴ compared Equations (26), (27), and (28) plus another relationship which related the modulus to the surface fraction of porosity to the 2/3 power. The latter formula involves a parameter which takes the 1/3 power of the voids per area and relates this to the slope of the relationship. This would be incorrect because the number density is proportional to the porosity and therefore would be a linear relationship. Dean and Lopez concluded that the linear relationship is the safest two-parameter method of analysis of modulus versus porosity data. Due to the lack of information on the microstructure of several of the specimens in the papers cited, the

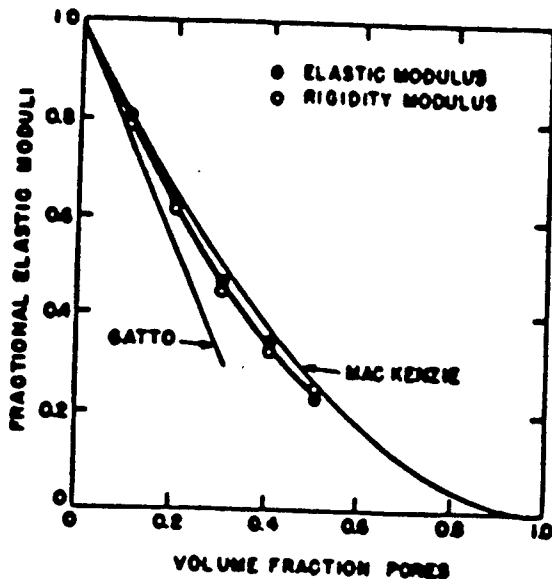


Figure 6: Relative elastic modulus vs. porosity, Coble and Kingery. Ref. (21)

determination of which model is most correct is difficult to decide. However, several models may be correct depending on the sample conditions such as amount and geometry of porosity, grain size and testing method.

A more accurate measure of the effect of porosity on the mechanical properties is the strength of a material. Knudsen²⁵ studied the mechanical strength of brittle polycrystalline materials with respect to porosity and grain size. Two prevailing relationships were examined using several different materials. The following equation has been proposed

$$S = S_0 D \quad (29)$$

where S is the strength, S_0 is the strength at theoretical density

and D is the relative density (1-porosity) raised to an empirical constant m. Experimentally the value of m was found to vary between 3 and 6 depending on the initial powder characteristics and the time and temperature of sintering. The value of m reached a limiting value of 3 for the optimum processing schedule. Ryshkewitch et al.²⁶ have observed that the strength varies logarithmically as the porosity increases linearly. The following semilogarithmic equation was obtained from Ryshkewitch's work.

$$S = S_0 e^{-bP} \quad (30)$$

where e is the actual number equal to 2.71828..., P is the porosity and b is an empirical constant.

Knudsen showed that Equation (30) can be approximated by Equation (32) if the value of b is set to 1.33m. If this approximation is made, a maximum difference between the values calculated from the two equations would be 18% when m = 6. In review of Coble and Kingery's and Knudsen's work (Figures 7 and 8 respectively), Equation (30) more closely approximates the data. Intuitive reasoning suggests that the decrease in strength due to the increase in porosity is due to the decrease in the effective load bearing area and the interaction between pores. Knudsen considered the decrease in load bearing area in a theoretical

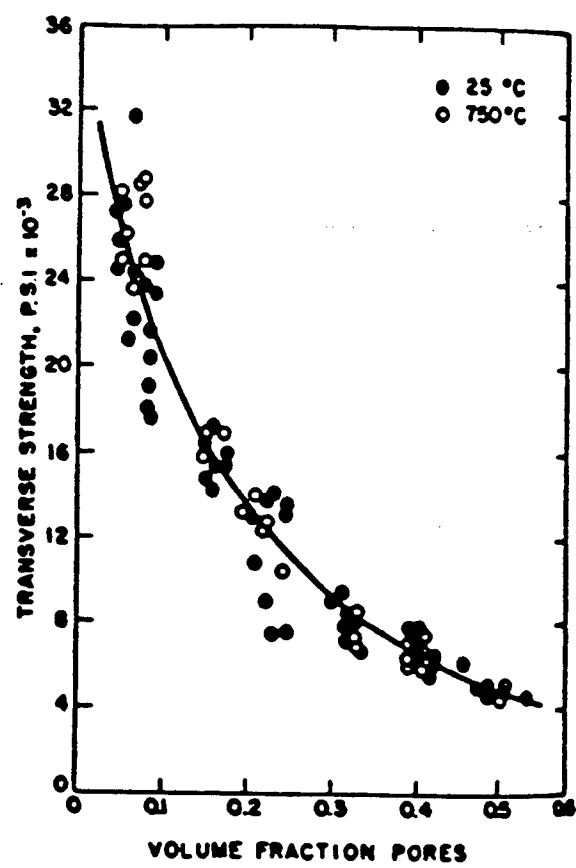


Figure 7: Effect of porosity on strength. Ref. (21).

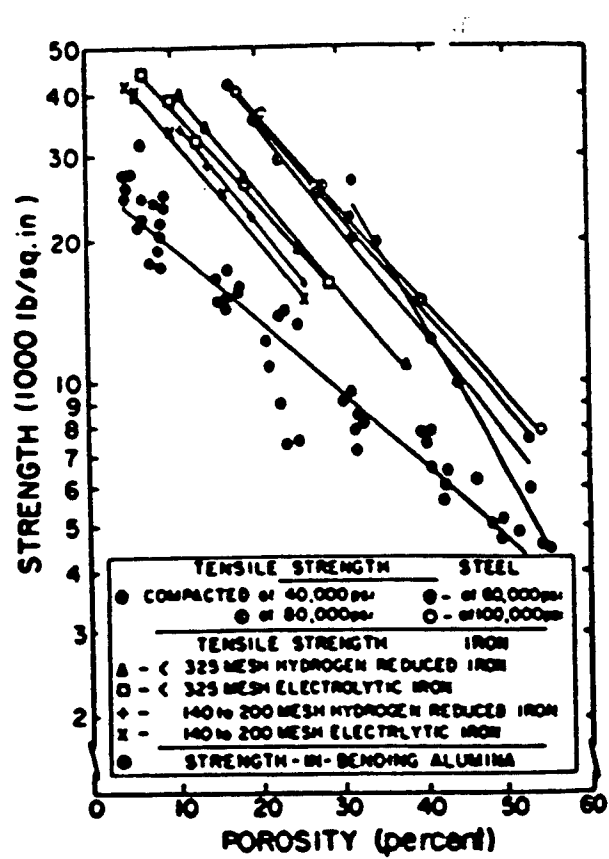


Figure 8: Strength of compacts produced by different processing methods. Ref. (25).

evaluation of the relationship. Using a highly idealized model, he obtained a similar dependence of the strength on the porosity.

BRITTLE FRACTURE

The strength of a ceramic body can be controlled by the presence of pores or flaws within the material. Upon introduction of a flaw into a stressed elastic material, a balance is obtained between the increase in surface energy from the formation of two surfaces and the decrease in potential energy due to the release of stored elastic energy. For the crack in Figure 9, the estimated surface energy term is equal to the total crack surface area ($2a2t$), and the surface energy γ . The decrease in potential energy for the case of an elliptical crack in an infinitely large plate was determined by Inglis²⁷ to be $(\pi\sigma^2a^2t)/E$. The change in potential energy is then

$$U - U_0 = -(\pi\sigma^2a^2t)/E + 4aty \quad (31)$$

where

U = potential energy of body with crack

U_0 = potential energy of body without crack

a = one-half crack length

t = thickness

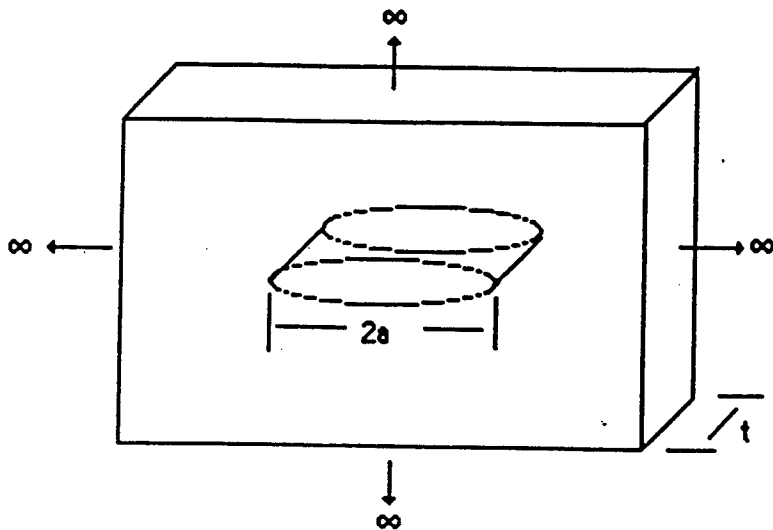


Figure 9: Crack penetrating through the thickness of a large plate. (Ref 28).

σ = applied stress

E = modulus of elasticity

γ = specific surface energy

Differentiating Equation (31) with respect to crack length and setting equal to zero for the equilibrium condition Equation (32) is obtained.

$$\delta U / \delta a = 4t\gamma - (2\pi\sigma^2 at)/E = 0 \quad (32)$$

($\delta U_0 / \delta a = 0$ because it does not vary with crack length). Equation

(32) can be rearranged to obtain the relation

$$2\gamma = \pi \sigma^2 a / E \quad (33)$$

which is for equilibrium. If the second derivative with respect to crack length is taken, a negative value is obtained which means the crack is unstable and will always grow. Rewriting Equation (33) for the case of plane strain, Equation (34) is obtained.

$$\sigma = [2E\gamma / \pi a (1 - \nu^2)]^{1/2} \quad (34)$$

where ν is Poisson's ratio. Equation (35) relates the fracture toughness to the size of the flaw

$$K_{IC} = C \sigma_f (a)^{1/2} \quad (35)$$

where K_{IC} is the fracture toughness, C is a geometrical factor approximately equal to $1.1 \pi^{1/2}$ for the case of a semicircular surface flaw, and σ_f is the stress at failure.

GRAIN SIZE EFFECT ON MECHANICAL PROPERTIES

It is generally recognized that the mechanical strength of ceramics decreases as the average grain size increases. However, there is disagreement on the apparent rate of decrease of the mechanical strength. Orowan²⁹ suggested that the dependence of strength on the grain size is an inverse relationship having the mathematical form

$$S_0 = KG^{-1/2} \quad (36)$$

where S_0 is the strength, G is the average grain diameter and K is a constant determined experimentally. Orowan based this theory on the assumptions that the initial flaw starts inside a grain and that the flaw propagates within the grain until it reaches a boundary. The grain boundary then acts as a barrier to the propagation of the flaw and their length will be on the order of the grain size. The stress required to propagate the flaw past the boundary is inversely proportional to the one-half power of the length of the crack³⁰.

Petch³¹ modified Orowan's concept to include the fact that glide planes might play a role in the initiation of fracture. The relation he proposed between the grain size and strength is shown in Equation (37).

$$S = S^* + K^*G^{-1/2} \quad (37)$$

where S is the strength, S^* is an empirical constant that is the applied stress needed to move dislocations along a glide plane in the presence of other dislocations and K^* is a proportionality constant. Knudsen determined that the Petch model fit data more often than did the Orowan model. Figure 10 shows the strength dependence of several materials on the grain size. Knudsen

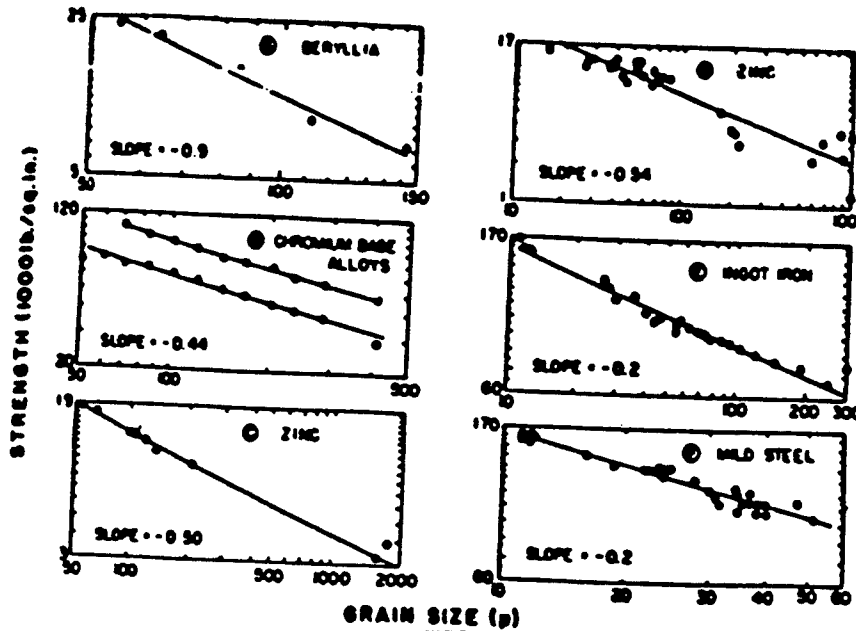


Figure 10: Grain size versus strength. Ref. (25)

proposed a model close in form to the Orowan model. The relation could be expressed as follows

$$S = kG^{-\alpha} \quad (38)$$

where k and α are empirical constants. This differs from the Orowan model in that the dependence on the grain size is not always to the $1/2$ power. From the data examined by Knudsen, the values of α ranged from 0.2 to 0.9 . This suggests that the initiation of the crack in the grain might be less favorable than propagation through the boundary. When the value of α is not $1/2$, the assumptions from Equation (38) are that the size of the flaw is controlling the strength, and that the size of the flaw is increasing

with grain size following the relation

$$F = KG^{-2\alpha} \quad (39)$$

where F is the size of the flaw, K is an empirical constant and α is identical to α in Equation (38).

Rice(32, 33) did an extensive study on the effect of grain size and compared both the Petch and the Knudsen equations. It was determined that the Petch equation was more readily adapted to the data available for ceramic materials. Rice found that the Petch equation could more easily allow for the determination of failure mechanisms within the material. The S^* term is the determining factor. When $S^* = 0$, flaw mechanisms dominate, when $S^* > 0$, microplastic behavior is dominant and when $S^* < 0$ the failure mechanism is due to internal stresses. This analysis is disputed by Evans and Tappin³⁴ in their study on alumina. They found that no simple relationship could be found for grain size and strength in alumina whereas Rice et al. have found an exponential relationship. Vasilos, Mitchell and Spriggs³⁵ performed work on pure, dense magnesium oxide. The resulting relation between the strength and grain size was found to follow the relationship proposed by Knudsen. These studies indicate that the relationship between strength and grain size can follow Equation (38) or Petch's

relationship.

Knudsen combined Equation (38) and (30) to obtain a relation involving both the porosity and the grain size.

$$S = kG^{-\alpha} e^{-bP} \quad (40)$$

This equation assumes that b is independent of grain size. Knudsen determined that the coefficient b was dependent on the firing but did not elaborate. The error involved in determining the strengths of other specimens with this equation was shown to be approximately $\pm 10\%$.

TEMPERATURE DEPENDENCE OF STRENGTH

Vasilos et al.³⁵ studied the effect of temperature on strength of dense, pure, hot pressed magnesia. They found that the strength was not affected until temperatures on the order of 600°C were reached. Above approximately 600°C, the strength of the specimens decreased as the temperature increased. They also noticed that below 600°C, Equation (38) determined by Knudsen²⁵ described the behavior of strength with grain size. But, at elevated temperatures, the dependence of strength on grain size tended to be less pronounced. The high temperature strengths of the larger

grained specimens was higher than that of the small grain samples. Vasilos et al. postulated that the decrease in strength may be strongly connected to dislocation mechanisms but a discussion on this topic is beyond the scope of this paper.

Fryxell and Chandler¹⁷ observed a different trend for the temperature dependence of BeO. Figure 11 shows that the strength of the material increases slightly as the temperature is raised. The larger the grain size, the larger the strength increase. Coble³⁶ also observed this trend and postulated that this was due to the increased internal stress of the large grained samples at room temperature. At elevated temperatures, the internal stress is released. Evans³⁴ studied alumina at elevated temperatures and observed an increase in the strength at elevated temperatures due to the decreased stress intensity around the failure causing flaw.

AGGLOMERATION EFFECTS

Powder agglomerates and aggregates are frequently encountered in active powders formed by calcination or other high temperature techniques. Agglomerates are "soft" inasmuch as they are a group of particles held together by forces such as surface charges, Van der Waals forces associated with organic molecules

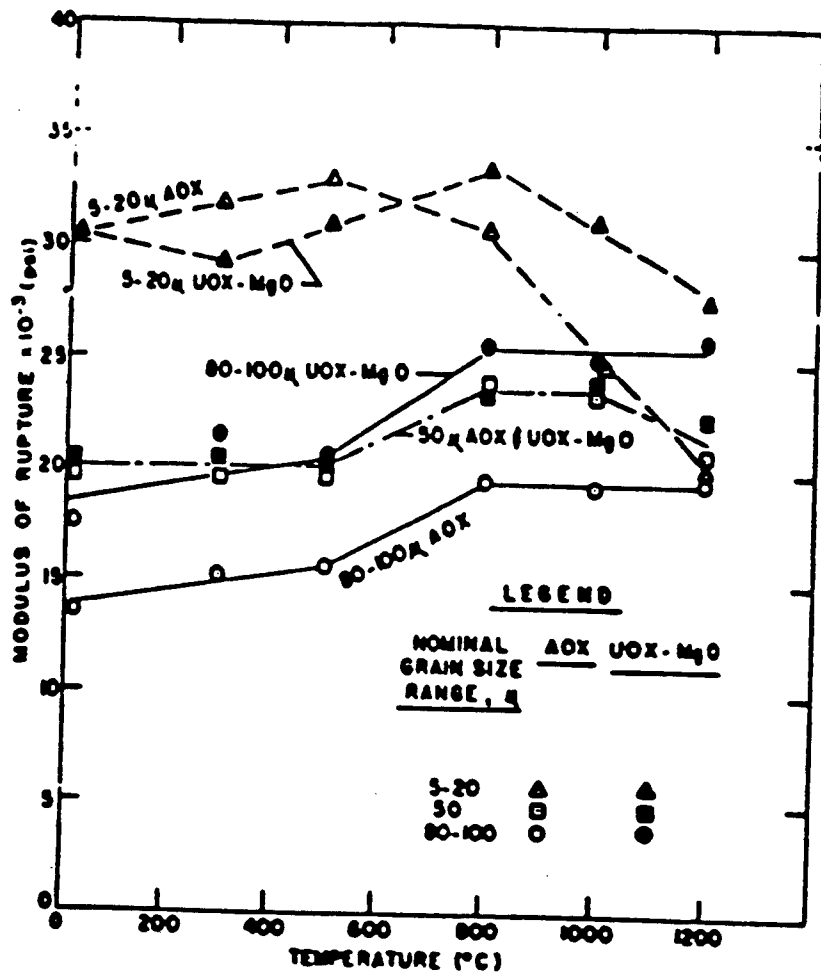


Figure 11: Modulus of rupture verses temperature for different grades of BeO. Ref. (17).

attached to the surface, hydrogen bonds and magnetic bonds in ferrimagnetic materials. Aggregates are the "hard" counterpart of the agglomerates. Aggregates are a group of particles held together by diffusional bonds formed during high temperature powder processing. The aggregate can be porous or completely dense depending on the degree of densification experienced during processing. These aggregates and agglomerates are detrimental to the formation of a defect free, strong ceramic component.

Aggregates or hard agglomerates cause a significant amount of microstructural damage during the densification process due to the differential shrinkage between the matrix and the agglomerates or aggregates. Dyns and Halloran³⁷ studied the effect of differing amounts of aggregates and pressing pressure on the density and microstructure of alumina (Figure 12). Powders pressed at the same pressure but differing in aggregate content showed a decrease in the green density with increasing aggregate content. Hsieh³⁸ et al. also saw this type of relationship between aggregates and green density. Figure 12 shows an approximately linear relationship between the percent aggregated and the green density of the alumina compacts. This is a reasonable result due to the fact that most aggregates are not

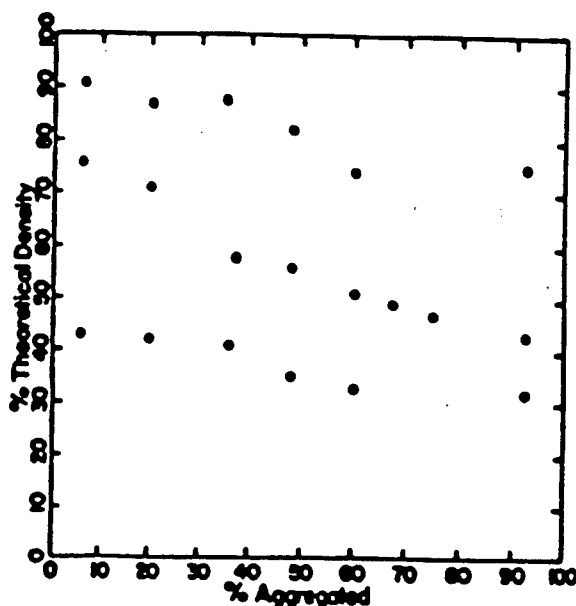


Figure 12: Green density as a function of aggregate content.
Compaction pressure = 34 MPa. Ref. (37).

being densified by the compaction procedure. As the percent of aggregation is increased, the volume of remaining powder available for compaction is decreased linearly. This is a very basic formalism but fits the data satisfactorily. The final sintered density is also affected by the amount of aggregates in the starting powders. Powders with a higher percentage of aggregates showed the same linear relationship with sintered density as with green density.

The effect of aggregates on the fracture of materials is related to the different densification rates between the matrix and the aggregate. The different densification rates are due to the

different green densities of the matrix and agglomerate. A very porous aggregate can be considered a hard agglomerate and will henceforth be called an agglomerate. Lange³⁹ showed that the densification rate of a compact formed from agglomerated powders was highly influenced by the green density although particle characteristics such as size and chemistry are the factors which have the most pronounced effect.

Agglomerates having low green densities, compared to the matrix, will densify at a greater rate than the matrix. This causes a tensile stress on the sintered agglomerate and a tangential compressive stress and a tensile radial stress within the matrix. If the agglomerate shrinks more slowly than the matrix, a compressive stress is placed on the agglomerate and a tangential tensile stress is placed on the matrix. The magnitude of the stresses would depend on the stress-strain behavior of the matrix and agglomerate. In order to relieve the tensile stress, cracks can form. Lange et al. have observed cracks formed around the surface of an agglomerate at the interface with the matrix caused by the rapid densification of the agglomerate. Radial cracks originating from the interface and extending out into the matrix can form due to the slower densification of the agglomerate.

The densification rate of the agglomerate can affect the final density by a significant amount. The pore volume surrounding the sintered agglomerate due to the differential shrinkage between the agglomerate and matrix can be analyzed geometrically.

$$P = [(\rho_{om} - \rho_{oa})/\rho_t]V_a \quad (41)$$

where P is the fraction porosity produced, V_a is the volume of low density agglomerates, ρ_{om} is the original matrix density, ρ_{oa} is the original agglomerate density and ρ_t is the theoretical density. From this simple equation it can be seen that the amount of porosity can be significant due to accelerated agglomerate densification. From a strength standpoint, the size of the agglomerate will dictate the size of the flaw. The strength is inversely proportional to the size of the flaw and therefore it would be expected that the strength is inversely proportional to the size of the agglomerates.

TOUGHENING MECHANISMS IN CERAMIC COMPOSITES

The interaction of a crack tip with a second phase particulate has been reported to increase the strength and toughness of a brittle matrix. It has been shown that the second phase particulates can provide an obstacle that impedes the motion of the crack through the material. Recent work done by Evans et al.⁴⁰ has shown that the major contribution to the strength increase in brittle matrix composites is due to a "line tension effect".

Lange⁴¹ theorized that a crack front could possess a line tension similar the analogy in dislocation theory. He based his theory on several assumptions mainly that the particles were point defects and that the crack shape at the breakaway point is semi-circular. He obtained an equation that related the fracture surface energy to the inverse of the inter-particle spacing and a linear relation to the crack line tension. Green and Nicholson⁴² et al. showed that the crack line tension which Lange assumed to be a constant was in fact dependent on the particle size.

Evans⁴⁰ discussed the bowing of a crack front due to the interaction with a pair of impenetrable obstacles from a fracture mechanical viewpoint. He compared the stress to move a semi-elliptical crack between two obstacles and the stress to

move a straight crack to the obstacle size and separation. Evans relation between these parameters showed that the ratio of the stress to move a semi-elliptical crack and the stress to move a straight crack increased as the particle separation distance decreased. Figure 13 shows the increase as a function of the ratio r_0/C where r_0 is the length of the particle and C is the particle separation.

Evans refined his model to include the effects of interaction of neighboring crack segments and variations in interparticle spacing. The results showed that the effect of variation in the particle separation was large at large values of r_0/C ie. the effect was large at small particle separation values. The effect on the ratio of the stress to move a semi-elliptical crack and the stress to move a straight crack was less important at large particle separations. The effect of interaction between neighboring cracks has been shown to decrease the stress needed to propagate an elliptical crack, but this effect is substantial at large particle separations. Figure 14 shows the effect of particle spacing and crack interaction. If the interparticle spacing is larger than approximately $40 \mu\text{m}^4$, the particles will have little or no effect on the strength.

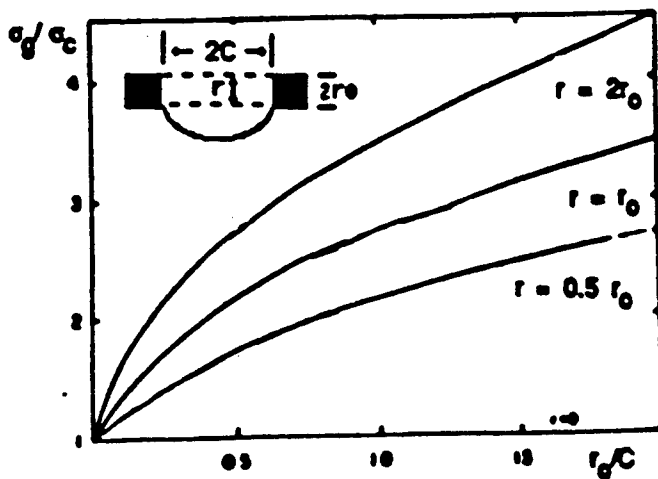


Figure 13: Magnitude of the ratio of the stress to move a semi-elliptical crack and the stress to move a straight crack versus r_0/C . Ref. (42).

Green and Nicholson⁴² considered that the increase in toughness by crack bowing was similarly related to the particle separation and geometry. Green et al. also considered the effect of a particle that was not impenetrable. Although no mathematical relation was given, it was rationalized that the stronger the particle, the larger the bowing effect on the progressing crack and hence, the increase in fracture toughness. As the particle gets more ductile, the less it impedes the crack. Hasselman and Fulrath⁴³ have proposed that the dispersed phase separation has a

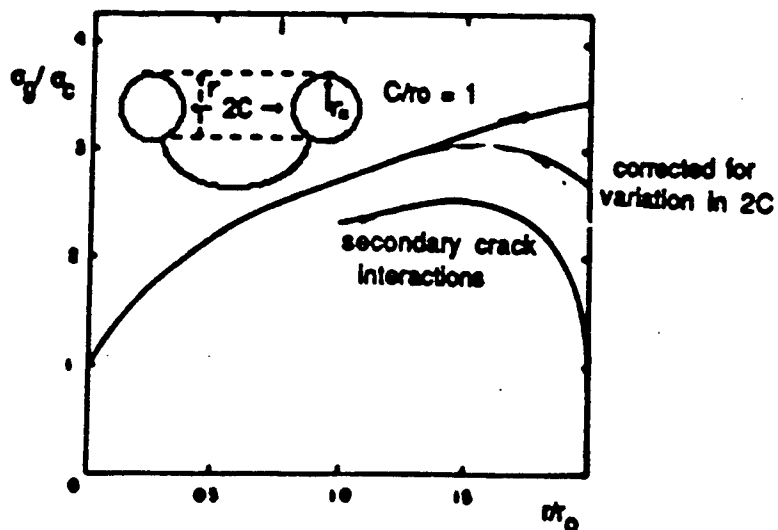


Figure 14. The effect of variation in interparticle spacing and crack interaction on the strength. Ref. (42).

limiting effect on the size of the Griffith flaws and therefore causes an increase in the strength. Both analyses agree with results of previous studies and therefore more research on the mechanism is needed. Other factors such as particle-matrix bonding and matrix-particle strength ratio will also have an effect on the strength of a composite but recent work has not indicated any research in this area.

CRACK DEFLECTION PROCESSES

Crack deflection occurs due to the presence of elastic or thermal expansion inhomogeneity. The inhomogeneity causes a

strain concentration to occur in the immediate area surrounding the defect. The interaction of a propagating crack and the strain field may cause the crack to deflect from its original plane of travel. The resulting deflection causes an enhancement in the toughness of the material by increasing the propagation energy. The strain field is usually caused by a particulate phase in the matrix with a thermal expansion coefficient that is different from the matrix. If a particulate has a larger thermal expansion coefficient, a tangential compressive force is placed on the matrix and cracks tend to be deflected around the particulate. Alternately, if the particle has a smaller coefficient of thermal expansion a tangential tension is experienced around the circumference the crack will be deflected into the particle. The latter mechanism may also produce a toughening effect from the bowing of the crack around the particulates as discussed in the previous section.

Faber et al.⁴⁴ have used a model assuming spherical particles separated by a uniform distance to determine the relative toughness increase in a specimen. Figure 15 shows the two

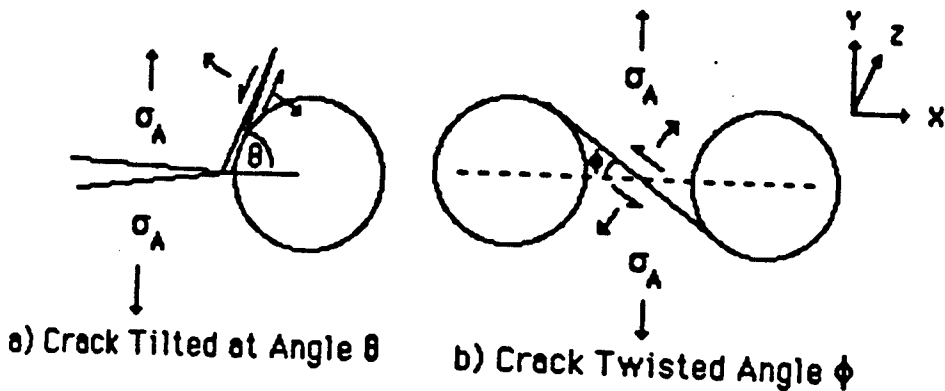


Figure 15. Examples of particle-crack interaction a) tilt and b) twist. Ref. (44).

mechanisms by which the crack can interact with the particle. The greater the angular deflection due to particle-crack interaction, the greater the strain energy required to propagate around the particle. This leads to an increase in the toughness of the material. An increase in the volume fraction increases the relative strain energy by the relation:

$$G^t/G^m = 1 + 0.87V_f \quad (42)$$

where G^t is the critical strain energy release rate of the deflected crack, G^m is the critical strain energy release rate of the

undeflected crack and V_f is the volume fraction of the particulate.

The deflected crack increases the surface area and this causes the increase in toughness.

The part of the crack that does not intercept the second phase particulate sees a component of twisting due to the deflection of the crack by the particulate. Faber et al.⁴⁴ have done extensive modeling of the crack tip motion and forces due to the twisting of the crack. They showed that the energy of propagation increases as the tilt angle increases which one would expect intuitively. The tilt angle, in turn, can be shown to depend on the interparticle spacing.

Figure 16 shows the dependence of the relative toughness on the volume fraction of second phase particulates and on the interparticle spacing distribution. The spacing distribution is based on a standard normal distribution. The amount of toughening is predicted to increase as a function of the deflecting particle volume fraction and be invariant with the size of the particle. Comparing this to the increase in toughness due to the increase in the surface area of the crack (Figure 17) shows that the increase is much smaller than the increase predicted for the strain energy release rate.

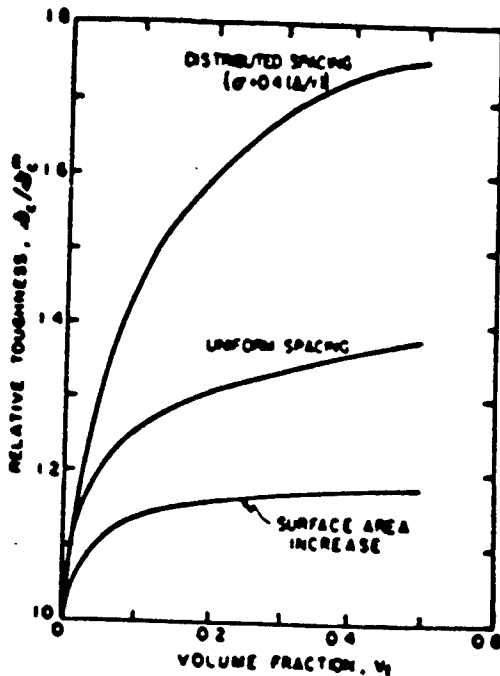


Figure 16: Relative toughness as predicted from crack deflection model including interparticle spacing. Also compared to surface area increase model. Ref. (44).

In comparison to the crack bowing model of toughness increase, the crack deflection model discussed predicts a much smaller effect on the toughness. Figure 17 shows the relative dependency with respect to the volume fraction of impenetrable particles. Experimental results from Faber and Evans⁴⁵ and Green et al.⁴² show that the increase in toughness falls between the predictions from the two models. This is an indication that the true mechanism is a combination of crack bowing and crack tip deflection.

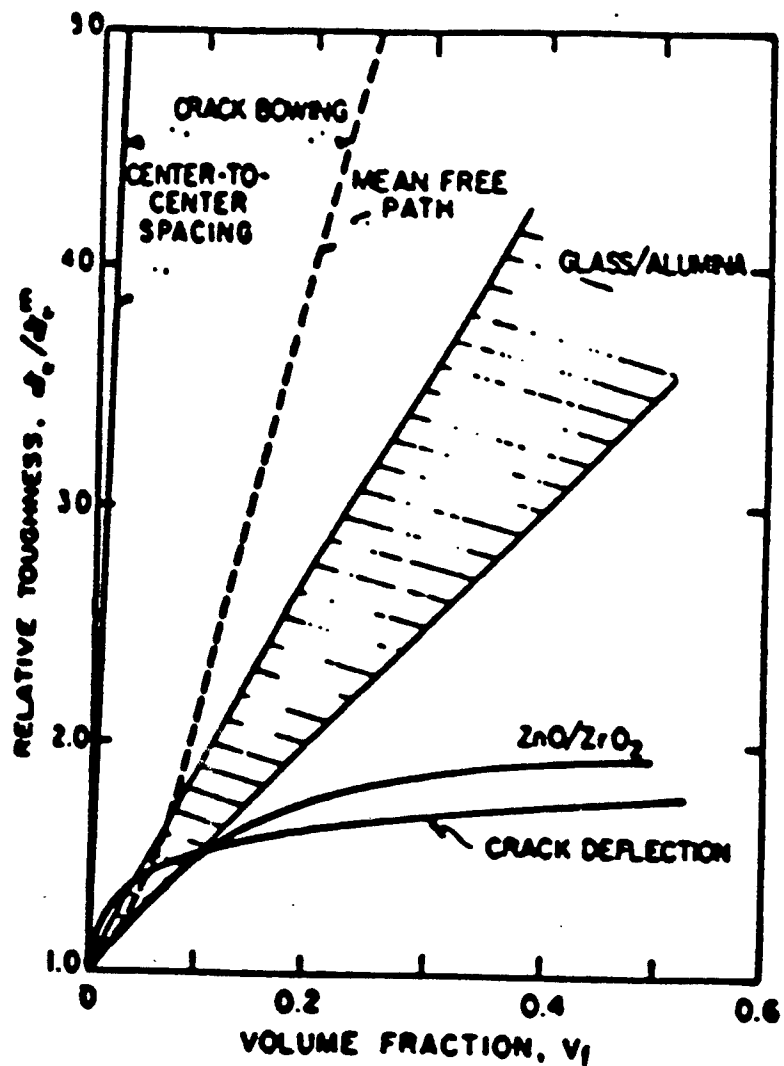


Figure 17: Crack deflection and crack bowing predictions for relative toughness. Also compared to experimental data from glass/alumina and ZnO/ZrO₂. Ref. (46)

TRANSFORMATION TOUGHENING

Transformation toughening has been extensively studied in the past several years due to the significant effect it has on the toughness of brittle materials. During the past ten years, it has been established that stress induced martensitic transformations can enhance the toughness of ceramic materials. The most extensively studied transformation effect is in ZrO_2 and in systems containing ZrO_2 as a second phase. Similar phase transformations occur in HfO_2 and possibly quartz and cordierite. The transformation in ZrO_2 is a phase change from the tetragonal to the monoclinic phase accompanied by a volume change of approximately 4-6%. Toughness values on the order of 18 MPa- $m^{1/2}$ are possible with a more likely value around 10-12 MPa depending on the matrix material^{4,6}.

Transformation toughening increases the toughness by the development of a zone of transformed material around the crack tip. The transformed zone produces stress and displacement disturbances that tend to shield the crack tip from the applied stress. The toughening is therefore dependent on the dimensions of the transformed zone and the amplitude of the disturbance.

Figure 18 shows the dependence of toughness on the

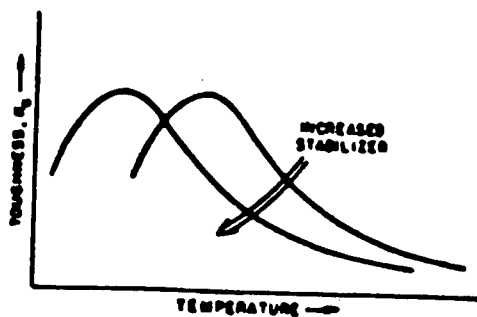


Figure 18: The effect of temperature on the toughness of a transformation toughened composite. Ref. (46).

temperature and the stabilizer content. The temperature dependence is due to the critical transformation temperature of the tetragonal second phase. At just above the critical transformation temperature, the toughening effect is the greatest because the transformation zone around the crack will be the largest and exert the greatest compressive forces on the crack surface. Below the critical temperature, the thermally transformed material does not result in a long range compressive forces over the crack surface and therefore does not contribute to crack shielding.

The size of the transformation zone is dependent on the amount of second phase material that transforms. The more sensitive the second phase is to the local strain field, the greater

the volume of material that transforms. Figure 18 indicates that there is a decrease in the toughness at constant temperature as the amount of stabilizer is increased. The sensitivity of the tetragonal-monoclinic phase transformation of zirconia is decreased as the amount of stabilizer is increased i.e. the tetragonal phase becomes more stable with increasing stabilizer. This reduces the size of the transformation zone by a significant amount due to the decrease in the stress as distance to the negative one half powder from the crack tip. A greater amount of stress is required to transform the tetragonal particles as the content of stabilizer is increased. Figure 19 shows the toughness as a function of stabilizer content in the Al_2O_3 - ZrO_2 system.

Figures 20 and 21 show the influence of second phase particle size on the fracture toughness. The increase in toughness is due again to the relative stability of the tetragonal phase. The particles become less stable as their size increases as Figure 21 shows. It therefore follows that the toughness increases with increasing particle size but only to the point where the particle is stable in the tetragonal phase.

Fracture toughening of ceramics is a relatively new area but extensive work has been done. Evans et al. have done extensive modeling of the forces and energies associated with the

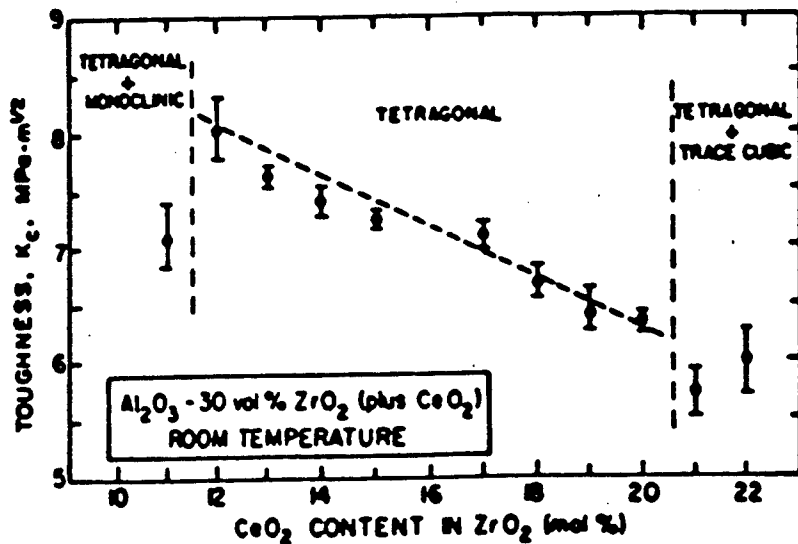


Figure 19: Effect of zirconia stabilizer on the toughness of an Al_2O_3 - ZrO_2 composite. Ref. (43).

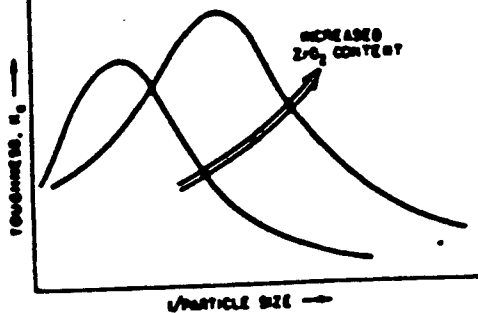


Figure 20: Particle size and concentration effect on toughness. Ref. (43)

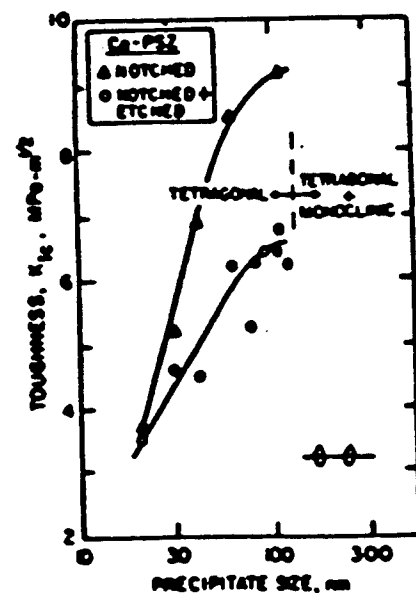


Figure 21: Toughness as a function of precipitate size. Ref. (46).

transformation toughening of ceramics. Their modeling has agreed satisfactorily with experimental observations but more study in the area of combined toughening mechanisms is needed.

CHAPTER III

EXPERIMENTAL PROCEDURE

RAW MATERIALS

The Bi_2O_3 used was obtained from the J.T. Baker Corp. The average particle size was reported to be 2 μm . The powder was 99.5% pure and had a classification of 1160 - R electronic grade. The Nb_2O_5 was obtained from Metron, Inc. and was 99.95% pure and was classified by sieve analysis to be < 325 mesh. The partially stabilized zirconia was obtained from Z Tech and was stabilized with 4.5 wt.% Y_2O_3 and classified to be 90% less than 0.49 μm . The SiC whiskers were purchased from American Matrix, Inc., Tennessee CAS # 409-21-2.

POWDER PREPARATION

The powder used for this study was prepared in several steps. The raw bismuth and niobium oxides were dry milled in the proper mole percentages in one gallon ball mills lined with

porcelain. The ball mill was half filled with milling media. The milling media were porcelain balls with diameters ranging from approximately 1.0 cm to 2.0 cm. The ball mill was then charged with 7lbs. of raw material and operated for 2 hours. The milled powders were then placed into zirconia crucibles and calcined at 700°C for eight hours to form a complete solid solution.

Milling studies were performed on powders undergoing wet ball and vibratory milling. The ball milling containers and media were identical to the ones used for the precalcining mixing. But before any milling could occur, the chunks of calcined material had to be crushed. This was accomplished in a porcelain-lined pan by hand using the bottom of a porcelain mortar as a hammer. This worked very well and reduced the large chunks of calcined material down to approximately 0.5 cm pieces. X-ray diffraction of the powder showed no indication of contamination from the mortar. The ball mills were then charged with seven pounds of the crushed material and enough media to half fill the ball mill. Six hundred milliliters of double distilled deionized water was then added; this was sufficient to fill the mill to a point just above the milling media and powder.

Five samples were taken during milling intervals of 30, 180,

350, 580 and 1500 minutes. The mill was fitted with a strainer that would prevent the milling media from escaping but allow a sample of material to pass through. After the samples were taken, they were dried completely and placed in a desiccator until examination took place. Each sample contained approximately 100 to 150 grams of powder.

Vibratory milling studies were also done using a Sweco twenty gallon vibratory mill. The mill was lined with a polymer coating to reduce contamination due to wear of the mill. The milling media consisted of alumina cylinders 10 cm in diameter by 13 cm long. The mill contained forty pounds of milling media. Fifteen pounds of BNO material was added to the mill along with 3000 ml of double distilled deionized water. Samples were taken initially and at intervals of 15, 30, 165, 620 and 1230 minutes during the grinding process by opening a discharge valve during operation. Each sample contained approximately 200 - 300 grams of powder. The samples were then dried and stored in a desiccator.

The samples taken during both milling procedures were very large with respect to the sample size needed for study. In order to reduce the size of the dried samples without causing a bias in the results, a simple mechanical splitting device was used (Figure 22). This device effectively reduced the size of the powder sample

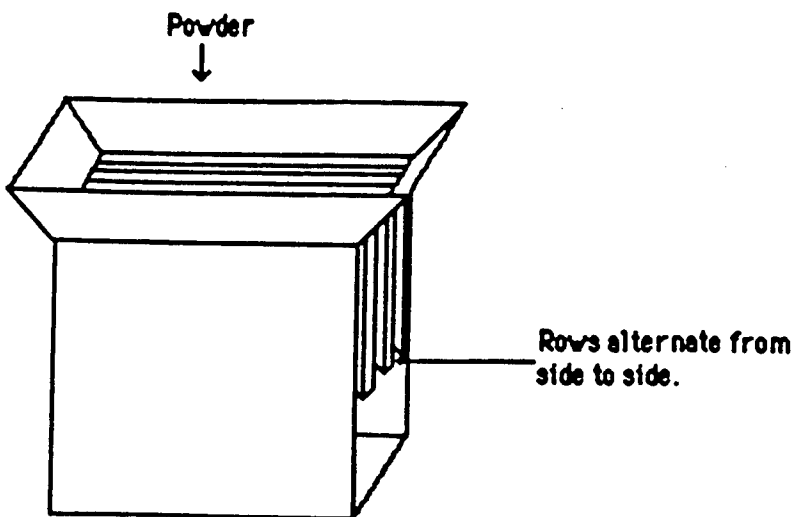


Figure 22: Mechanical splitting device used for producing representative powder samples.

down to approximately 10 - 20 grams. Two identical samples were produced from each of the initial samples.

COMPOSITE PROCESSING

Several methods of increasing the mechanical properties was attempted. The first involved the introduction of partially stabilized zirconia into the matrix. Several different compositions were prepared in an attempt to obtain the highest strength possible. The zirconia had been stabilized in the tetragonal form with 4.5 percent yttria. The second technique used to increase the strength of the BNO matrix was by fiber reinforcement. Silicon carbide whiskers were introduced into the

BNO matrix in proportions of 3, 5 and 7 weight percent. The BNO material used as the matrix material for all the composite specimens was the 15 mole percent niobia doped bismuth oxide. The BNO material had been processed by the technique previously outlined in powder processing.

The two powders were mixed in a one pint plastic container with approximately 51.5 grams of milling media, or enough to fill the container half way. The milling media used were the alumina cylinders used in the vibratory milling study. The container was charged with 50 grams of the zirconia-BNO powder and approximately 150 ml double distilled deionized water and milled for two hours. This was to insure that proper mixing occurred. The mixed material was then removed from the containers and dried in an oven set at 98°C.

Mechanical and microstructural evaluations were performed on sintered bars produced from powder produced from each milling technique. The dried powders were mixed with three weight percent of a polyvinylalcohol (PVA) solution. The PVA solution was composed of ten grams of Dupont Elvanol grade 51-05G PVA dissolved into ninety grams double distilled deionized water. The powder and binder were mixed in a porcelain mortar and pestle for

about 15 min. The powder was then passed through a 20 mesh screen to form evenly distributed powder agglomerates. If the powder was not immediately processed, it was placed into a glass beaker and covered tightly. The powders were not stored for more than a few hours before being processed.

The processed powder was pressed into rectangular bars with dimensions of 0.2 by 1.62 inches. The die was made of a low carbon steel alloy. Each bar weighed approximately five grams and was pressed under a load of 2500 pounds or a pressure of 7700 PSI for five seconds. The pressure was then slowly released to avoid forming laminations in the bars. Using this procedure, bars were produced that had enough structural integrity to be handled routinely and were free from any visible defects such as laminations.

The dry pressed bars were sintered in air on a zirconia setter covered by several layers of coarse zirconia sand. The spherical sand particles allowed the bars to shrink as they densify. The sintering took place in a programmable furnace designed by L&L Furnace Co., Inc. The sintering schedule is given in Table 1.

This sintering schedule was later modified by Kenny and Associates⁴⁷. Kenny and Associates performed Rate Controlled

Table 1. Initial sintering schedule for BNO samples

Start Temp (°C)	End Temp (°C)	Ramp Time (hours)	Hold Time (hours)
25	550	15	00.0
550	750	40	00.0
750	870	10	20.0

Sintering studies on bismuth niobium oxide and determined an optimum schedule that would give the highest density while maintaining a small grain size. Table 2 gives the rate controlled sintering schedule. In order to accommodate such a complicated sintering schedule, a different furnace was required. A CM RapidTemp furnace with a Eurotherm controller capable of holding the program was required to produce this sintering schedule.

PRECIPITATION TOUGHENED SPECIMEN PROCESSING

Precipitation toughened samples were processed in a similar way to the composite samples. The precipitation toughened samples were composed of bismuth oxide doped with smaller amounts of niobia than that typically used (15 mole%). The samples were processed on a much smaller scale than the larger extrusion batches. A typical sample size was 100 grams. The raw powders were weighed out on an analytical balance in plastic

Table 2: Sintering schedule as determined by rate controlled sintering studies done by Kenny and Associates. Ref. (47).

Heating rate (°C/min)	Final Temperature (°C)	Time Required (min)
5.0	80.0	12.5
0.5	500	852.5
10.0	640	866.5
6.1	696.7	875.8
0.2	697.1	878.1
2.4	733.0	893.1
0.8	740.8	902.7
2.2	790.1	925.3
-1.1	782.8	932.1
2.1	812.2	946.4
3.5	836.1	953.2
3.1	915.3	978.9
-15	800.0	986.5

sample dishes. The powders were then mixed in one pint plastic containers filled half way with grinding media (vibratory mill media). The powders were dry milled for two hours to insure a homogeneous mixture.

The powder was separated from the media and placed into zirconia crucibles for calcination. The calcination schedule for the precipitation toughened samples followed the same schedule as the large BNO batches. The calcined powders were removed from the crucibles and broken up in a mortar and pestle before milling. The milling took place in the one quart plastic containers that were used to mix the raw powders. The containers were half filled with grinding media and charged with the calcined powder. Enough double distilled water was added to just cover the media and the powder (\approx 150 ml). The powders were milled for twenty four hours before being dried, weighed and pressed into bars in an identical procedure to the composite samples.

The bar samples were sintered using a modified Kenny Associates schedule shown in Table 3. The modification was needed because as the niobia content is lowered, the melting temperature is also reduced. The maximum sintering temperature of the modified schedule is 820°C.

Table 3: Modified RCS sintering schedule to accommodate the samples with the lower niobia contents.

Heating rate (°C/min)	Final Temperature (°C)	Time Required (min)
5.0	80.0	12.5
0.5	500	852.5
10.0	640	866.5
6.1	696.7	875.8
0.2	697.1	878.1
2.4	733.0	893.1
0.8	740.8	902.7
2.2	790.1	925.3
-1.1	782.8	932.1
2.1	812.2	946.4
3.5	820.0	948.6

The samples were annealed at 625°C to precipitate out a second phase. Samples were annealed at different times to try and determine the rate of precipitation. Annealing times were 50, 75, 105 and 120 hours. Each sample was later examined using x-ray diffraction techniques.

MECHANICAL TESTING

Mechanical tests on samples produced by precipitation and composite studies were conducted on a model 4201 Instron. The samples were tested using a four point bend arrangement and a crosshead speed of 1.5 mm/min. Figure 23 depicts the four point bend testing conditions. The complex geometry of the honeycomb shown in Plate 1 does not permit any machining of the surface of the channels. Therefore, the samples were tested as fired to approximate the true condition of the honeycomb after sintering.

The surface treatment of a ceramic can determine the fracture strength of a part. Because the samples were sintered on a bed of zirconia, the samples had to be tested in a manner that would reflect the true strength of the material. A problem that occurred during testing arose from defects in the surface of the bars caused by contact with the coarse zirconia bed on which they were sintered. A solution to this problem was to test the surface

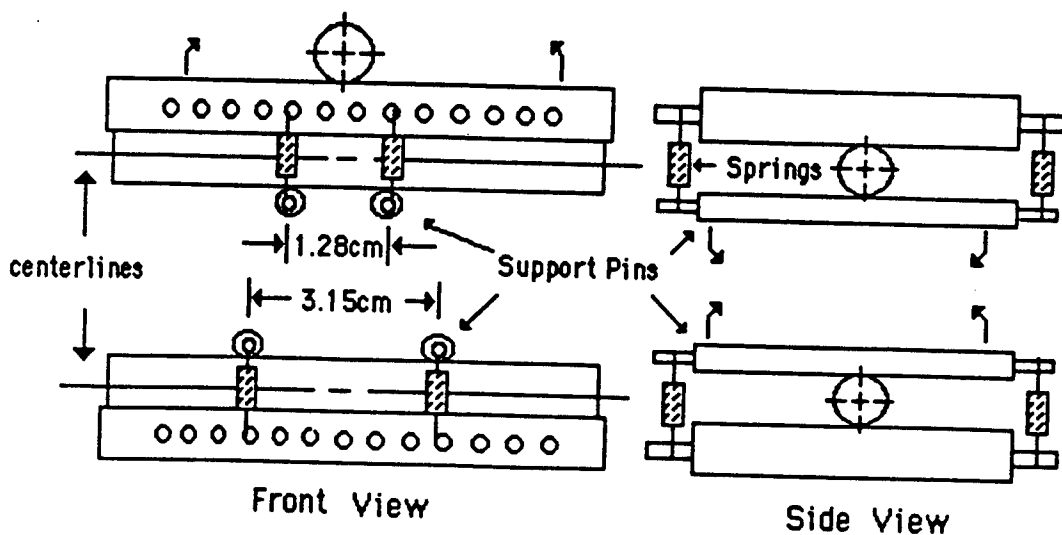


Figure 23: Mechanical testing design used for modulus of rupture testing. Four point bend design.

of the bar exposed to the atmosphere in tension and not the surface in contact with the sand. This insured that no bias due to contact with the coarse zirconia bed occurred.

HIGH TEMPERATURE MECHANICAL TESTING

High temperature mechanical tests were performed on bar specimens pressed from the vibratory milled powder. Figure 24 shows the experimental setup. The furnace was allowed to heat up to the desired temperature for at least one hour. Once the temperature had stabilized, the top of the furnace was lifted and a sample was placed on the lower supports. The top was then

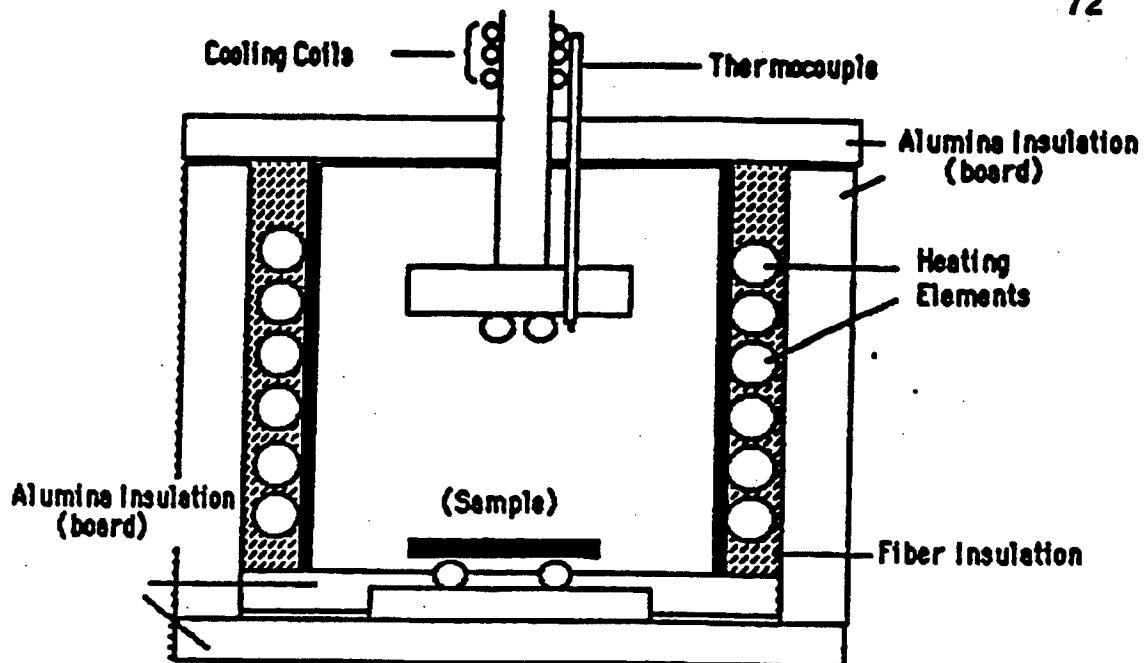


Figure 24: Experimental arrangement used for high temperature modulus of rupture tests.

replaced and the furnace was allowed to reestablish thermal equilibrium. This usually took between five and fifteen minutes depending on the temperature at which the experiment was conducted. The testing temperatures were 200, 400 and 600°C. The testing dimensions and crosshead speed was identical to the room temperature tests.

FRACTURE TOUGHNESS

Fracture toughness measurements were conducted on specimens prepared using the same process as the four point bend

specimens. The bars were tested as sintered because the surface was adequate for testing and visible irregularities in the surfaces were very uncommon and similar to those in the honeycomb sections. The measurements were done using two different techniques. The first technique was indentation fracture toughness. A Vickers indenter was used to make indents in the center of the samples using a load of 2.2 Kg. The indenter head was aligned in such a way that the radial cracks would occur parallel and perpendicular to the longitudinal axis of the bars. The indents were made in a heavy mineral oil to retard any slow crack growth. The bars were immediately transferred from the indenter to the Instron and tested in a four point configuration. The four point configuration was identical to the previously mentioned arrangement for modulus of rupture testing. The fracture toughness was calculated using the following empirical formula:

$$K_c = N_R (E/H)^{1/8} (\sigma P^{1/3})^{3/4} \quad (43)$$

where N_R is a geometrical constant, E and H are the Young's modulus and hardness respectively, P is the indentation load and σ is the modulus of rupture. Chantikul and Anstis^{4,8} determined experimentally that the assumption that $N_R(E/H)^{1/8}$ is equal to 0.88 would introduce no more than 10% error in the evaluation of K_c .

The second method uses the same four point bend geometry but instead of a crack induced by an indentation, the crack is machined into the bar. The machined crack is one order of magnitude larger than the cracks produced by the indent. The cracks were machined into the bars using a Buehler diamond wafering blade and an isomet low speed saw. The crack was machined at the center of the bar perpendicular to the longitudinal axis. The fracture toughness was related to the load at failure by the following equation:

$$K_c = \sigma(\pi a)^{1/2} F(a/b) \quad (44)$$

where a is the notch length, b is the sample height, σ is the modulus of rupture as determined in four point bending and $F(a/b)$ is a value obtained from Figure 25.

HONEYCOMB EXTRUSION.

The extrusion process required approximately fifty to sixty pounds of material. This meant that several small batches had to be processed and mixed together prior to extrusion. The entire process took several weeks to accomplish. The calcined and vibratory milled BNO material was mixed in seven pound batches with methylcellulose binder. The mixing took place in the one gallon porcelain lined ball mills used for mixing the raw powders.

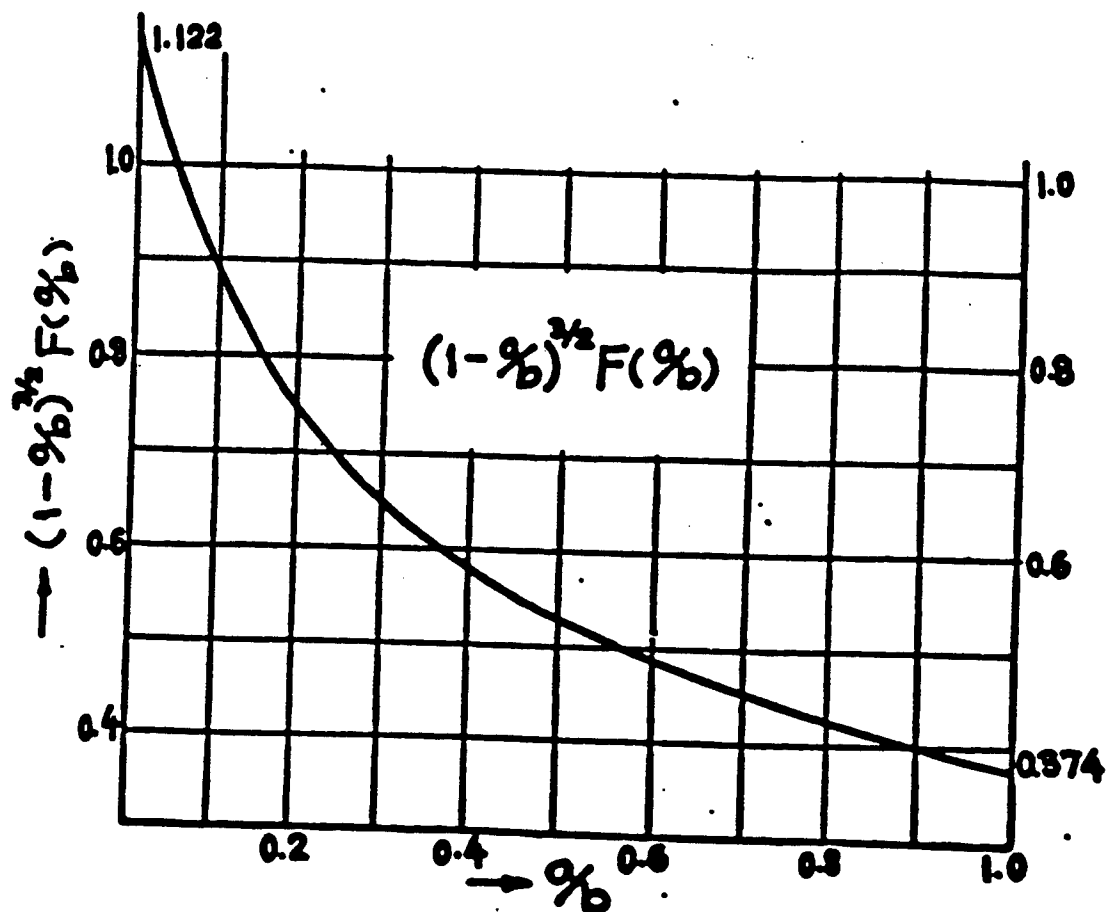


Figure 25: Graph of the exponential function $F(a/b)$ used in determining the fracture toughness on notched beam specimens. (Ref. 49).

The mills were filled to approximately 50% capacity with the porcelain balls. The methocel and BNO powder was added and was allowed to mill for two hours. The balls and powder were separated using a 20 mesh screen. Due to the large amount of material needed and the relatively small mixing capabilities of the ball mills, this fifty pounds of material was further homogenized using a V-blender. The batch was blended overnight to insure a homogeneous distribution.

The basic composition of the extrusion batch contains 100 grams BNO powder, 15 grams water, 4 grams methocel and 4 grams liquid Ivory soap. The methocel is a cellulose ether obtained from Dow Corning. In order to dissolve methocel into water, it must be heated to approximately 95°C. Therefore the dry powder and methocel that had been mixed previously was placed into a convection oven and heated to 98°C. The soap was mixed with water and placed on a hotplate to heat the mixture to 98°C. The soap does not dissolve completely at room temperature and therefore the water and soap were mixed an elevated temperature. The soap and water were mixed together after heating the water to the boiling point. The proper amounts of soap and water were measured and mixed together after heating to eliminate the water

loss. When the soap dissolved, the mixture went from a milky white to a clear solution.

The powder/methylcellulose and soap/water mixtures were combined in a Hobart bowl mixer with a 20 lb capacity. The powder was placed into the Hobart bowl and the mixer was turned on. The soap solution was then slowly added to the powder. As the solution was added to the powder it would become very fluid with a viscosity close to that of water. During this period, the sides of the bowl were scraped constantly to remove any powder left distributed to the sides. As the temperature of the batch decreases, the methocel begins to form a gel and the viscosity increases. Mixing continues until the viscosity has increased to a point where BNO particles will no longer settle to the bottom. The batch is then transferred to a sealed container and placed into a water bath to maintain a temperature of 15.5 °C. The viscosity of the batch is temperature controlled. It is vital that the temperature of the batch be controlled closely from this point. A recirculating water bath at a temperature of 15.5°C was used in this capacity. This temperature produces an optimum batch viscosity.

The batch at this stage contains large amounts of trapped air

and is not yet ready to be extruded. Deairing and final mixing of the batch was done using a Johnson and Thomas #2619 pug mill. Figure 26 is a diagram of the pug mill. The batch was de-aired by passing the batch through the pug mill in a specific pattern. The material that passed through the pug mill first was passed through the mill at the end of the second de-air process. Material selected randomly was then passed through the pug mill during the third de-air run. This helped insure that the batch was evenly mixed and deaired. Following the deairing process, the batch was sealed and returned to the water bath. The batch was ready to extrude after this step.

Figure 27 shows a simplified version of the hydraulic press and the die arrangement used to extrude the honeycomb geometry which were designed at The Ohio State University. The extrudate material is placed in the extrusion chamber and a vacuum pulled on it. The material then passes through a series of separated homogenizer plates. The homogenizer plates, shown in Appendix A, help mix and homogenize by separating and recombining the material. The material then encounters a backer plate which controls the thickness of the outer skin on the honeycomb by controlling the amount of material that encounters the outer edge of the mask. A beveled edge on the mask plate forms the solid skin

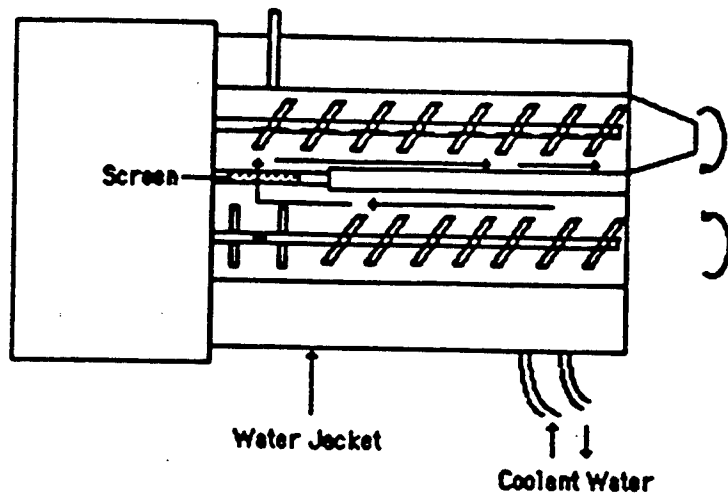


Figure 26: Diagram of a pug mill.

from the material allowed through by the backer plate. The larger the backer plate, the more material is allowed through to the outer edge of the mask plate. The extruded honeycomb is dried by placing it into a microwave oven, set at the maximum power level, in which it is heated for approximately thirty to sixty seconds. The piece is then rotated and heated again for the same length of time. This procedure is carried out several times until the part is dry enough so that it will stand on its own without deforming. The piece was then placed in a convection oven set at 98°C and allowed to completely dry overnight.

The honeycomb samples were very difficult to sinter because the complicated geometry of the honeycomb leads to severe cracking. During sintering, the ceramic part would completely disintegrate due to the intense cracking that occurred. The lack of

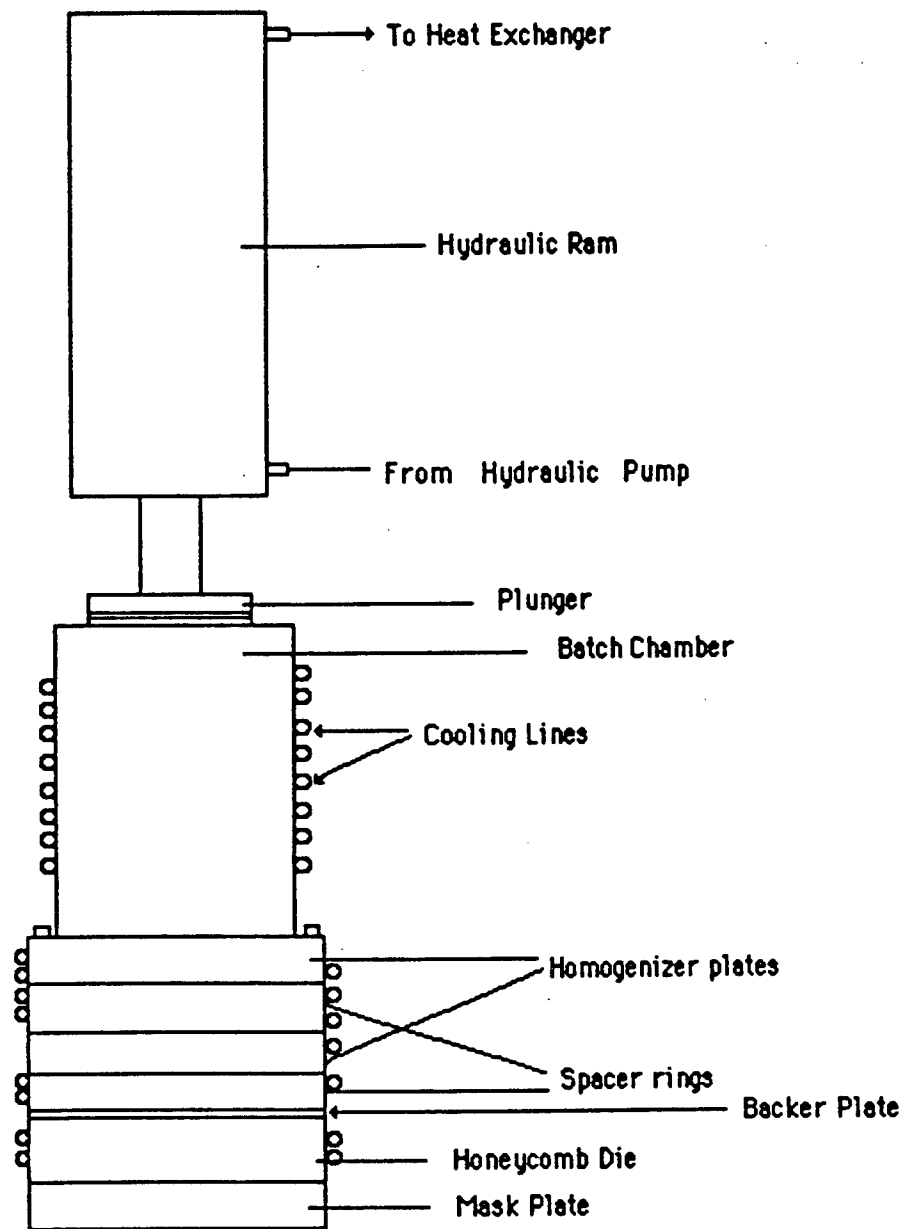


Figure 27: Experimental design used for the extrusion of honeycombs.

structural integrity of the component rendered the part useless. A solution to the cracking problem involved the use of zirconia sand which produces a constant compressive force on the part during sintering. The honeycomb part was placed into a large zirconia crucible. The honeycomb was placed on two sections of green honeycomb material approximately one quarter inch in thickness. The zirconia sand was then added around the crucible until the level of the sand was even with the top of honeycomb part. A thick layer of fiberfax was placed on top of the crucible to reduce thermal gradients within the part. The crucible was then placed into a furnace and sintered using the schedule found in Table 2.

CHARACTERIZATION TECHNIQUES

The particle size of the vibratory and ball milled powders was determined by two different methods. The first procedure used a method which took a two dimensional area of a particle from a photograph and converted it into an equivalent diameter of a circle. The powder was ultrasonically dispersed in acetone for thirty minutes, mounted on an aluminum SEM stub using an eye dropper and then photographed using a scanning electron microscope. A Carl Zeiss Videoplan was used to determine the area of the particle in a photograph using the outline of the particle.

The area contained in the outline of the particle was then converted by the videoplan into a diameter for a circle of equal area. Approximately eighty particles from each photograph were used as data points.

The second method used to determine the particle size was by BET or nitrogen adsorption. The remaining identical sample was used for this procedure. A Micromeritics Flowsorb II 2300 surface area analysis machine was used to determine the average particle diameter.

Sintered microstructures were examined using an Olympic optical microscope. The samples to be examined were mounted in an epoxy resin and ground using silicon carbide grit. The samples were ground with successively finer grits ranging from 240 grit down to 600 grit followed by polishing with a 3.0, 1.0 and 0.3 micron alumina/water suspension.

Chemical etching of the sintered material was used to reveal the grain boundaries. The chemical etchant was a solution of 6.25 volume percent concentrated nitric acid, 31.25 percent concentrated hydrochloric acid and 62.5 percent double distilled deionized water. The polished sample was swabbed with the solution for ten seconds and rinsed with distilled water.

The grain size measurements were conducted on the Zeiss Videoplan in a manner identical to that used for the particle size measurement. A photocopy of a photograph was placed on the magnetic pad and the grain boundaries were traced with the pen. The results were given in terms of an equivalent circle diameter.

Density measurements were made on sintered samples using the Archimedes principle. The sintered specimens were washed for ten minutes in acetone using an ultrasonic bath. The samples were then dried at 98°C and weighed to +/- 0.0001 grams. The samples were immersed in water and placed back into the ultrasonic bath for 20 minutes. This helped remove any entrapped air from the outer pores. The weight in water was then recorded to 0.0001 grams and the density calculated.

X-ray analysis was conducted on several samples throughout the course of this work. Two different x-ray units were used to determine phases present. The first unit was a Phillips GEX 3200. The sample used in this machine was ground under acetone in a porcelain mortar and pestle. The ground powder was then placed into several drops of acetone on glass slide. A razorblade was used to even the powder out on the slide. Once the sample had completely dried, it was ready to be analyzed.

The second x-ray unit to be used was a Scintag PAD V unit. The sample had to be mounted so that it was in a vertical position. In order to do this the ground powder was mixed with Dow Corning vacuum grease and smeared onto a plastic sample holder. The mixture was then smoothed out until flat.

Thermogravimetric analysis was performed using a Perkin-Elmer 7 Series Thermal Analysis System. Approximately 150 mg of powder was placed into a platinum crucible. The TGA runs were performed in air at sample heating rate of 5⁰C/min.

CHAPTER IV

RESULTS

PARTICLE SIZE REDUCTION

Initial particle size reduction after calcining took place using ball and vibratory milling techniques. The two techniques were examined using particle size analysis versus time. The results of the milling study showed that a significant decrease in particle size resulted from both the ball and vibratory milling techniques. The average starting particle size of the powder was 2.506 μm as determined by BET analysis. The two techniques used to determine the average particle size (BET and area equivalent circular diameter) gave very different results. The area equivalent circular diameters were found to be much larger than the results from the BET analysis. Figure 28 shows a typical photograph of the powders after mounting on an SEM stub.

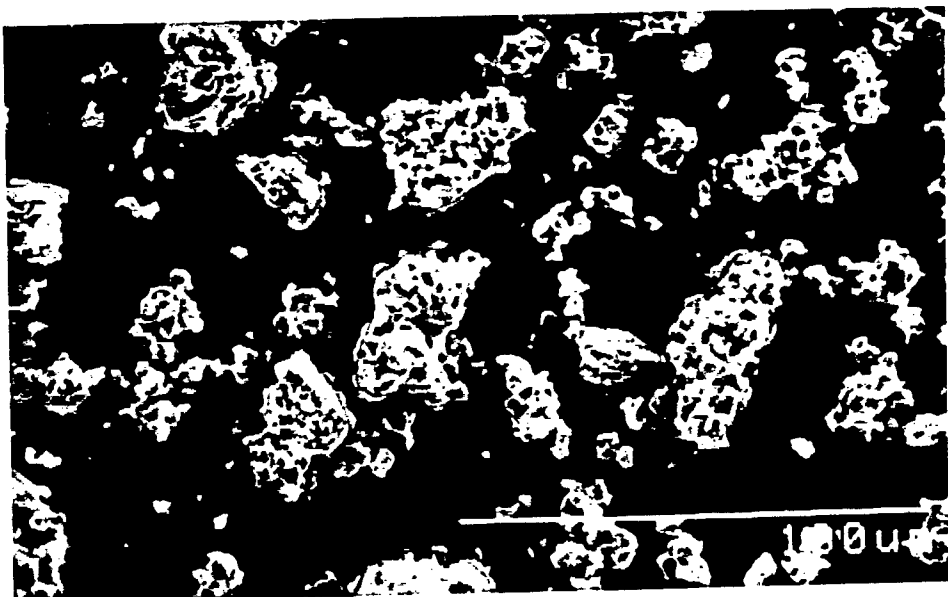


Figure 28. SEM photograph of BNO powder showing the large amount of agglomeration.

The small particles were found to be in agglomerate form and were very hard to distinguish even at high magnification.

Table 4 lists the particle size as a function of time for both milling and measurement techniques. As expected, reduction in particle size occurs at a much greater rate in the vibratory mill procedure than in the ball mill. The final average particle sizes obtained using vibratory and ball milling techniques

Table 4: Particle size as a function of milling time for the ball and vibratory milling techniques. Data from both of the measurement techniques is given.

Time(min)	Particle Size		Vibratory Milled	
	Ball Milled		Videoplan	BET
	Videoplan	BET		
0.0	---	---	---	2.506
15	---	---	3.1785	2.0635
30	7.8928	2.2394	---	1.315
165	---	---	2.1303	0.6981
180	2.1429	2.0305	---	---
350	2.2799	1.7532	---	---
580	1.9109	1.4706	---	---
620	---	---	1.1273	0.3051
1230	---	---	0.9362	0.1617
1500	1.5388	1.2163	---	---

were 0.1617 μm and 1.2163 μm respectively. The milling time for the respective final powder sizes was 20.5 hours for vibratory milling as compared to 25 hours for ball milling. Figure 29 shows the reduction in particle size versus time for both milling and measurement techniques. The graph indicates that the grinding rate is an exponential function of milling time. This is consistent with the work of Smith et al⁵⁰.

Figure 29 also indicates that a point of diminishing returns is approached. The milling process is much more efficient at the onset of grinding than at the end. Rose et al.⁵¹ have explained this in terms of the decrease in the rate of interaction with the grinding media. As the particle is reduced in size, the probability that it will encounter a collision between two grinding media is decreased dramatically. This leads to a decrease in the rate of grinding and a point where increased grinding time is very inefficient. The longer grinding times result in an increase in the contamination with only a minimal decrease in the particle size. Figures 30 and 31 give an indication of the particle size distributions resulting from the two grinding techniques. Examination of the powders under SEM suggests that the particle size distribution obtained by ball milling is broader than in the

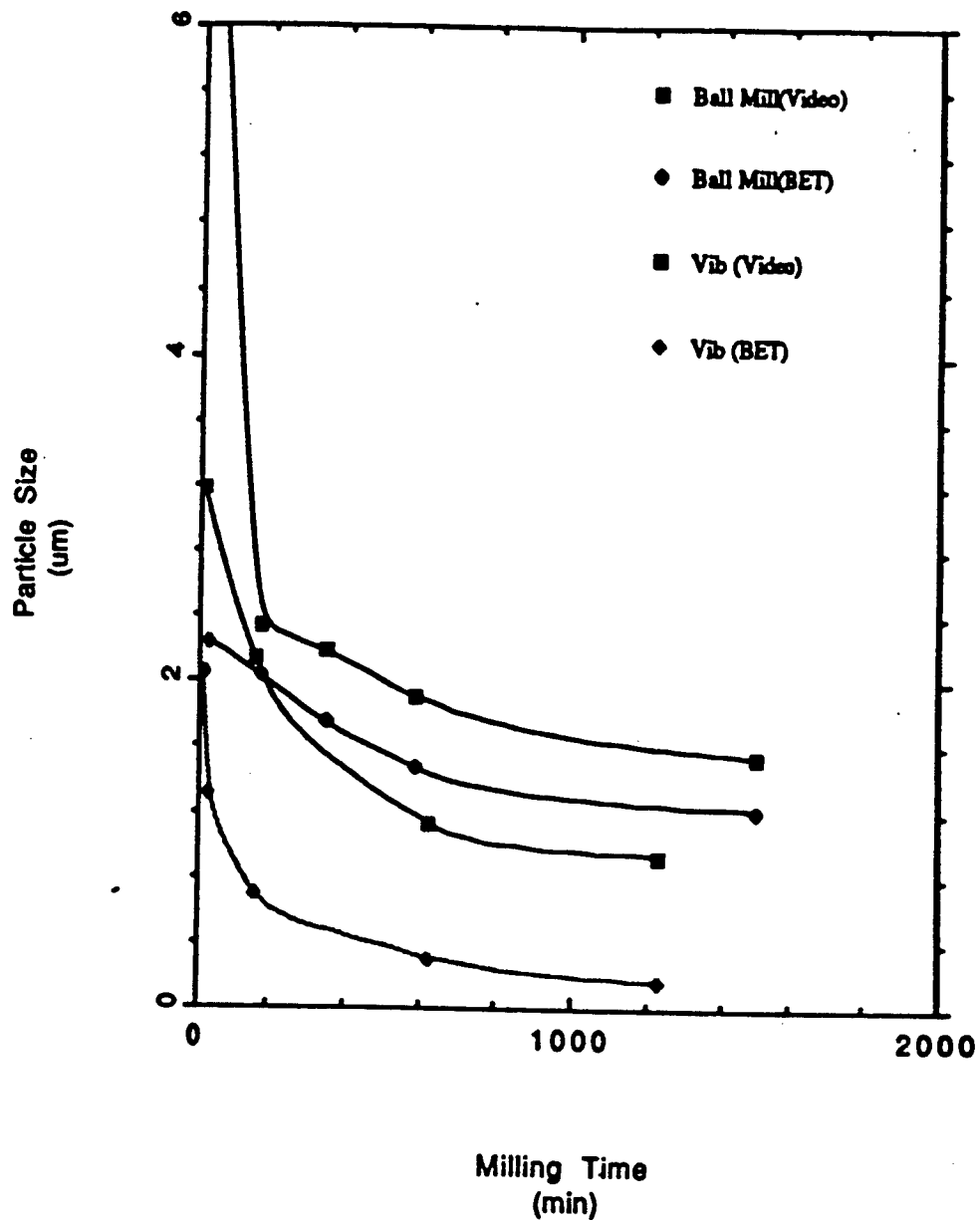


Figure 29: Particle size verses milling time for the vibratory and ball milling techniques.



Figure 30: Typical ball milled powder. Magnification 4,000X.

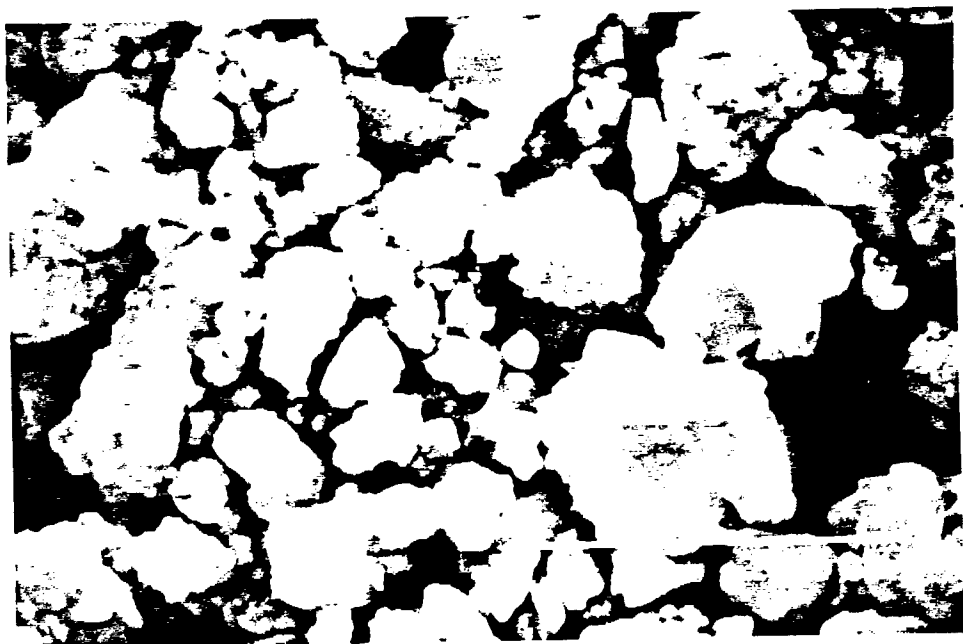


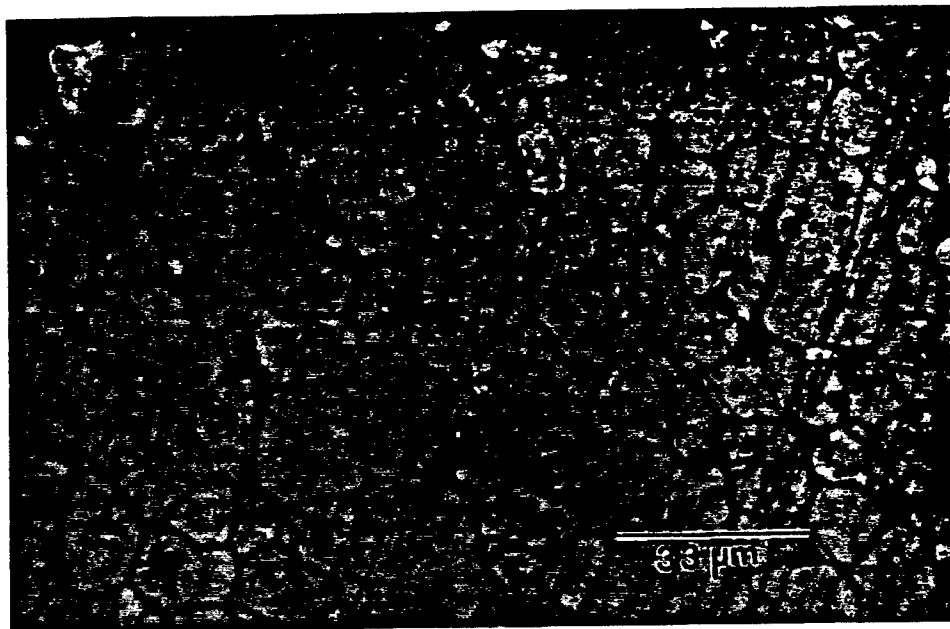
Figure 31: Typical vibratory milled powder suggesting a narrow particle size distribution. Magnification 4,000X.

particle size distribution of the vibratory milled powder.

PARTICLE SIZE EFFECT ON STRENGTH AND MICROSTRUCTURE

The reduction in particle size had a profound effect on the mechanical and microstructural characteristics of the niobia doped bismuth oxide. The average grain size was determined for bar samples produced from both vibratory and ball milled powder sintered using the schedule in Table 1. The grain size was reduced by a significant amount in the vibratory milled powder. The average grain size was 26.17 μm in the bars made from ball milled powder. The grain size was reduced to 15.41 μm in bars made from vibratory milled powders. The decrease in grain size is in agreement with Cooper et al.⁵² who saw an decrease in grain size with decreasing initial powder particle size. Figures 32 and 33 show the microstructures of the bars after etching. The decrease in the grain size is evident from examining both microstructures. The sample in Figure 32 was etched for a longer time to enhance the grain boundaries and does not accurately reflect the size of the porosity.

Another interesting feature is the location of the porosity in the two materials. The porosity is located within the grains in the



92

Figure 32: Microstructure of bars produced from ball milled powder. Dark areas are pores. Grain size = 26 μm .

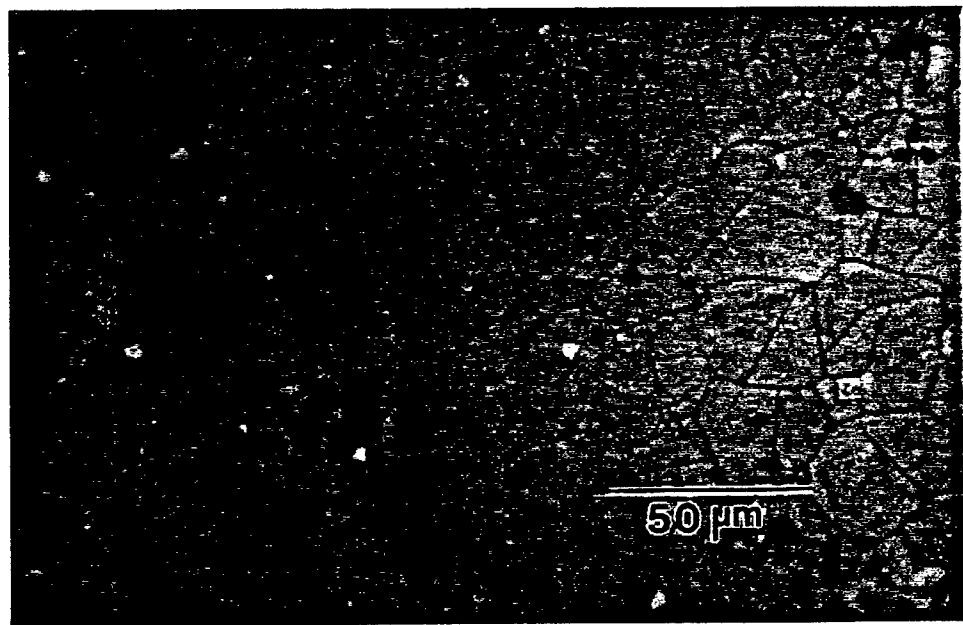


Figure 33: Microstructure of bars produced from vibratory milled powders. Magnification 400 X. Grain size = 15 μm .

samples produced from the ball milled powder. This implies that the grain boundary motion was rapid in the compacts produced from the ball milled material because the pores are trapped within the grains. This limits the densification process because only volume diffusion can remove the pores. The bars made from the vibratory milled powder showed porosity primarily at the grain boundaries. Both of the samples exhibited normal grain growth during the densification step. No evidence of secondary grain growth was present throughout the entire study.

Another indication of the enhancement of the microstructure was the greater density of the sintered compacts produced from the vibratory milled powder. The density of the sintered compacts was 8.113 g/cm^3 and 8.4117 g/cm^3 respectively for the compacts produced from the ball and vibratory milled powders. The increase in density from 95% to 98.3 % theoretical density is evident from the reduction in porosity in Figures 34 and 35. The theoretical density from X-ray diffraction is 8.557 g/cm^3 (53).

Modulus of rupture (MOR) measurements were made on specimens prepared from ball and vibratory milled powders (Appendix B and C). The samples prepared from the ball milled powder had an MOR of 13.13 MPa with a standard deviation of

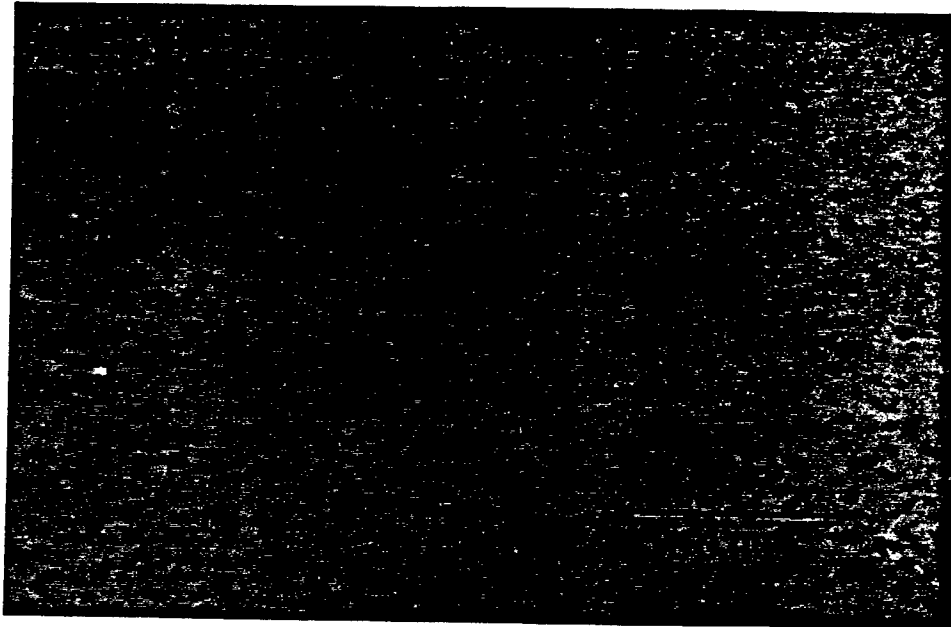


Figure 34: Porosity in sintered of bars produced from ball milled powders. Magnification 200 X.

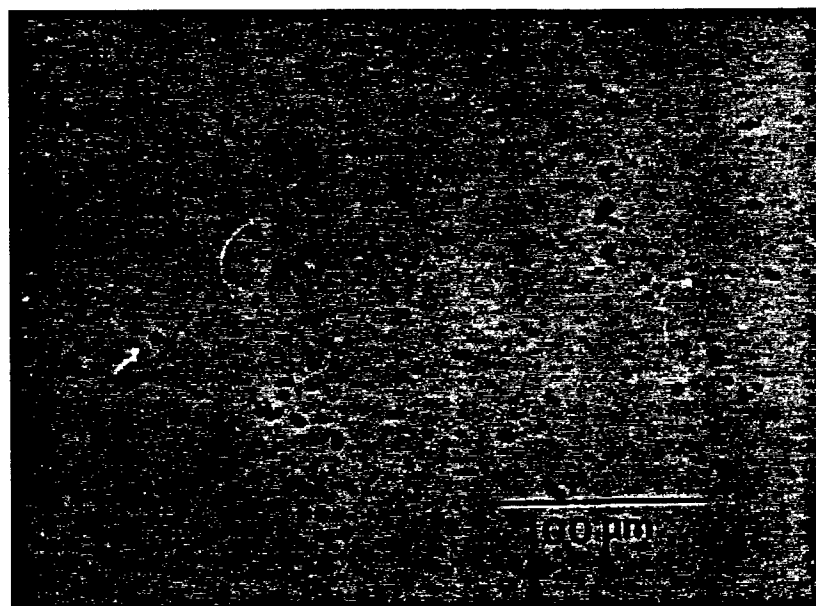


Figure 35: Porosity in bars produced from vibratory milled powders. Magnification 200 X.

0.2716 (40 samples tested). The MOR of samples made from powder that had been vibratory milled was 30.15 MPa with a standard deviation of 0.764 (40 bars tested).

EXTRUSION OF HONEYCOMB GEOMETRIES

The extrusion of honeycomb compressors was initiated on a smaller scale than outlined in the experimental procedure. Batch sizes were on the order of 150 to 200 grams as opposed to 50 or 60 pounds for the large scale extrusions. Because the initial powder was of a different particle size than in work done previously by Powers⁵⁴, a small scale extrusion was done to determine if the water content of the extrusion batch had to be modified. Batches of 14.0, 14.5 and 15.0 percent water were processed and extruded using a smaller die ($\approx 1"$ diameter). The walls and the skin of the batch containing 14.0 percent water showed signs of damage due to insufficient water content. The skin of the honeycomb had tears and the walls were not connected to each other in several places. The batch containing 14.5 percent water still showed signs of damage but at a reduced level. However, the batch containing 15.0 percent water showed no signs of skin tearing and the walls knitted together completely.

It was therefore decided to use a water content of 15 percent in the large scale extrusion batch. The first large scale extrusion run produced honeycombs that had several problems. Upon exit from the die mask, the skin immediately pulled away from the interior of the honeycomb. This indicated that the flow rate was faster near the center of the die than at the surface, due to die wall friction. Several screws were placed into the homogenizer plate that blocked the flow of material through the holes in which they were placed. The screws were placed near the center of the plate in order to slow the flow in the center of the die. This did not result in the elimination of the problem. The skin still continued to pull away (termed "peeling") from the rest of the honeycomb. Along with these problems, the water content of the batch was too high. The honeycomb batch was very adhesive and this undoubtedly contributed to the skin pulling away from the interior cells. No usable honeycombs were produced in this run.

Several more full scale extrusion runs were performed and encountered some of the same problems as the previous runs. The water content of these batches were 13.5 and 14.0 percent. The previously extruded honeycombs had a problem with the cells not knitting (unconnected to one another) which was attributed to the increased water content. This did not happen in the batches

containing 13.5 or 14.0 percent water. The decrease in water content also caused the peeling severity to decrease by a small amount. Good results were obtained from both batches and it is apparent that both water contents produce satisfactory results. In order to decrease the peeling of the skin, a flow restrictor plate was machined and used in the later extrusions to increase the friction in the center of the die. Appendix D shows the geometry of the plate. Using the flow plate did not reduce the amount of peeling significantly.

SINTERING OF HONEYCOMB COMPONENTS

The large shrinkage encountered during densification caused the honeycombs to crack extensively when sintered in an unsupported fashion. Figure 36 shows the experimental apparatus used to sinter the honeycombs. This placed a hydrostatic compressive force on the components during the entire sintering schedule. The first honeycombs sintered using this design held together very well but cracks at the bottom of the component at the interface between the honeycomb and the setter piece were present. This was attributed to the friction between the two parts and the different rates of shrinkage.

Several arrangements of the encasement technique were tried in an attempt to decrease the frictional forces between the honeycomb and the setter. Figure 37 shows an arrangement used to sinter a honeycomb sample that reduces the force between the setter and component. The size and thickness of the setter pieces were also varied in an attempt to prevent the cracking of the honeycombs but these changes had minimal effects. None of the methods employed decreased the extent of cracking. The plastic flow (creep) of the material at sintering temperatures prevented any attempt to sinter the material by supporting it on movable objects or by point objects. If supported in this manner, the material would creep extensively.

Measured values of densification shrinkage were large. The average shrinkage ranged from 18 to 21 percent. The reduction in the shrinkage of the component was a possible solution to avoid cracking at the part/setter interface. Because the calcining schedule produces a large amount of shrinkage, it was examined to determine if the Bi_2O_3 and Nb_2O_5 had reacted completely to form a solid solution. Figures 38 and 39 are the respective x-ray patterns for material calcined at 700°C and 800°C . It is clear from these patterns that the monoclinic Bi_2O_3 phase from the starting bismuth

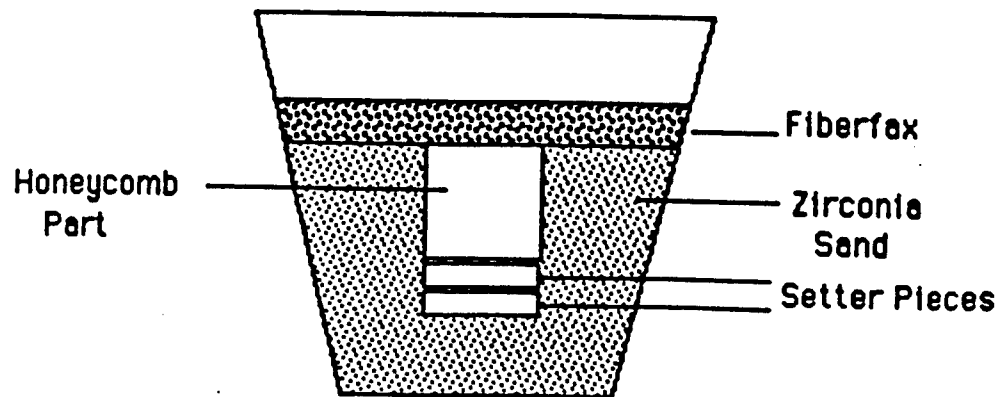


Figure 36: Sintering arrangement placing the honeycomb in hydrostatic compression.

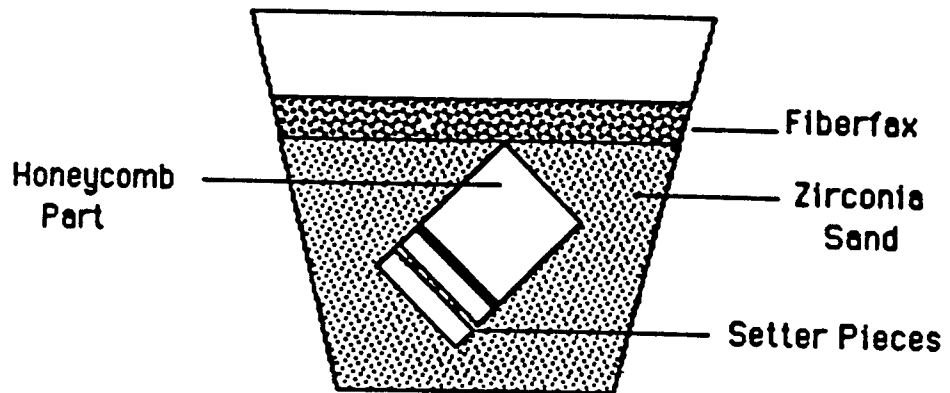


Figure 37: Sintering arrangement reducing component-setter friction.

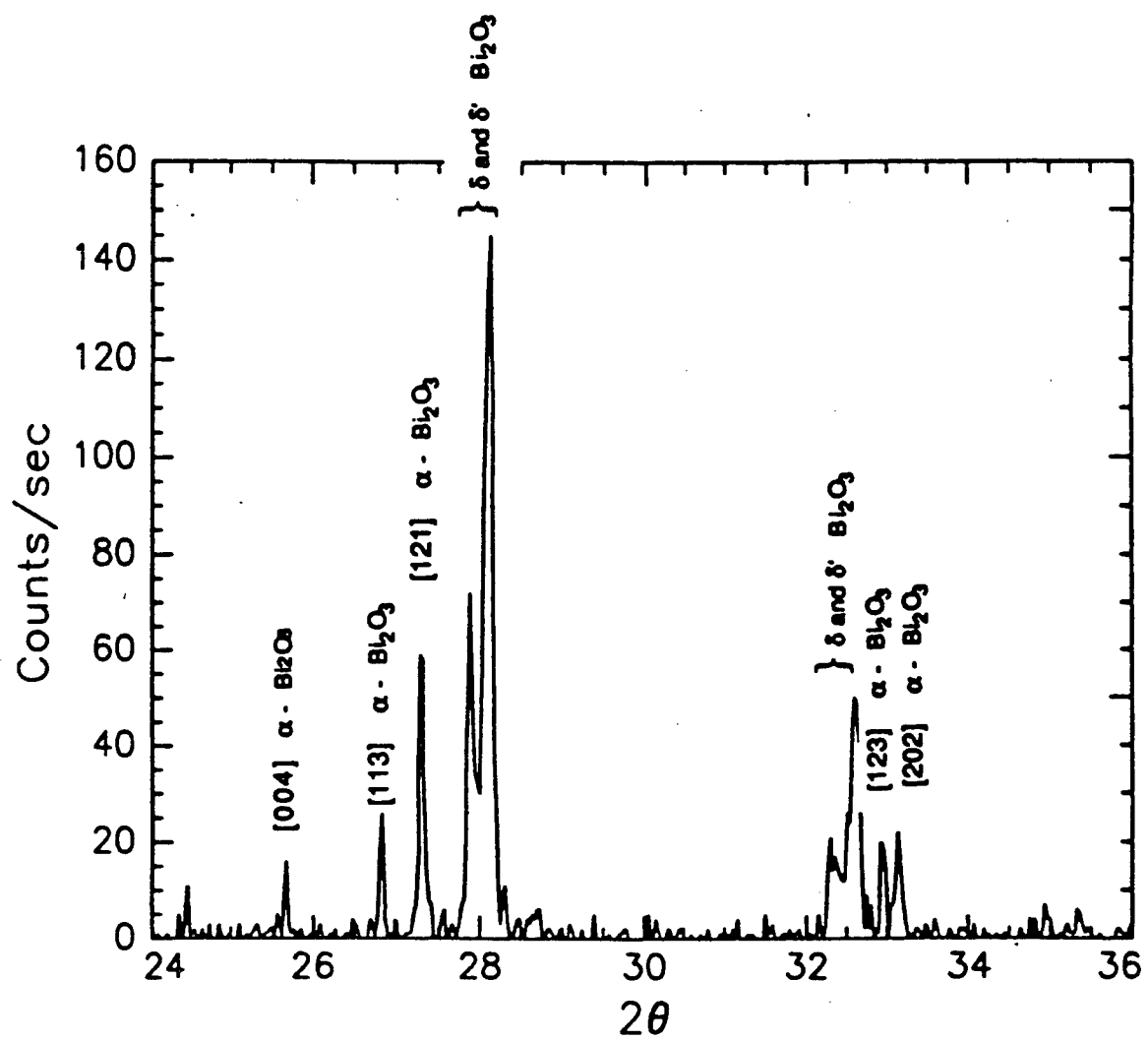


Figure 38: X-ray pattern from BNO material calcined at 700°C showing the monoclinic Bi_2O_3 phase.

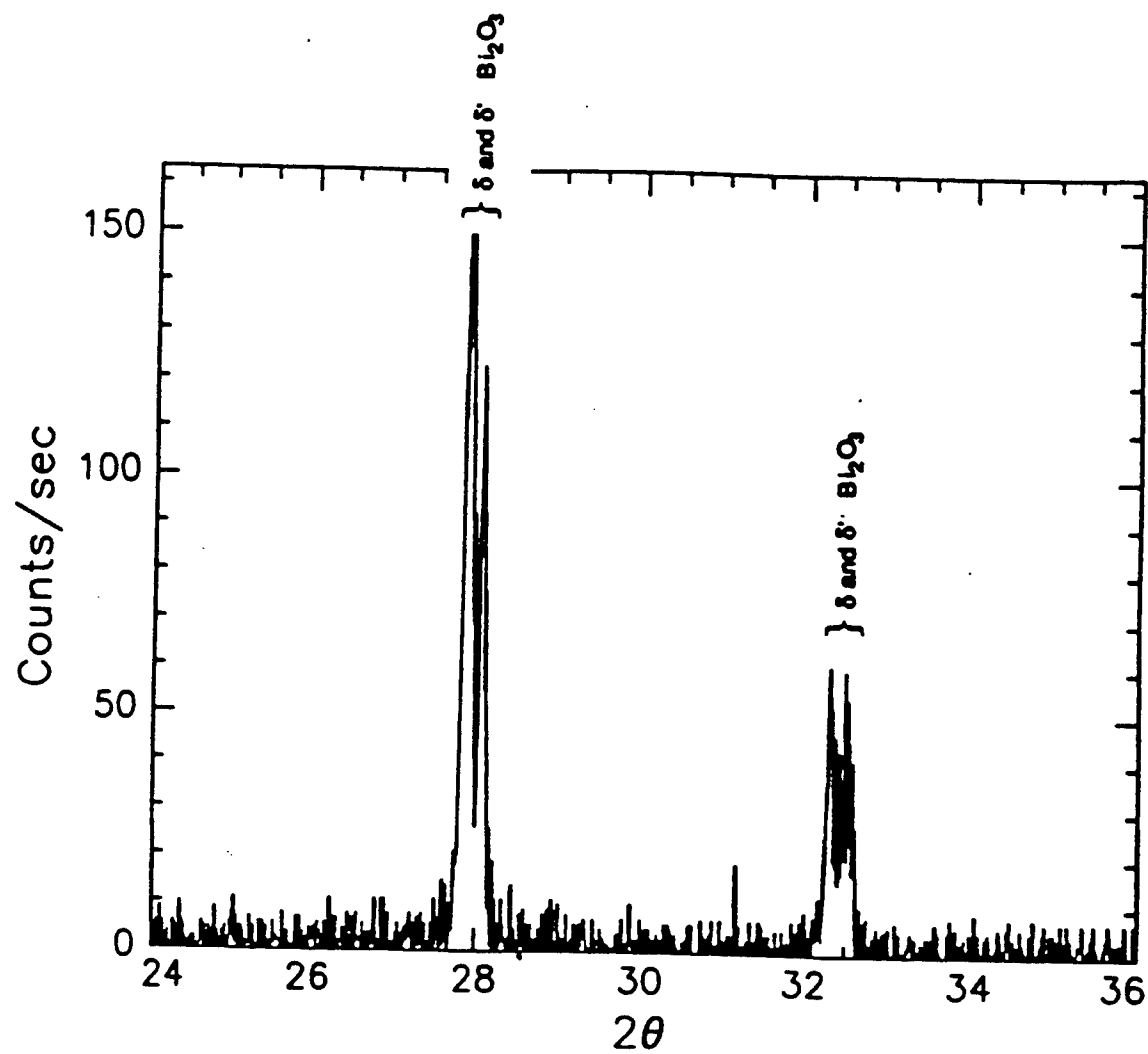


Figure 39: X-ray pattern of material calcined at 800°C showing the cubic phase.

powder is still present after calcining at 700°C, indicating that the reaction to form the cubic $(Nb, Bi)_2O_3$ solid solution was incomplete. The pattern at 800°C shows only the cubic solid solution $(Bi_{.85}Nb_{.15})_2O_{3.30}$ indicating that complete dissolution of niobia into Bi_2O_3 had occurred (i.e., the reaction is complete).

After increasing the calcining temperature, the powder became much more dense than that previously obtained. This led to an increase in the final particle size after vibratory milling. The average particle size increased from 0.1616 μm to 2.0 μm as determined by nitrogen adsorption measurements. This had a large effect on the densification of the final honeycombs. The honeycombs produced from this powder were sintered using the arrangement shown in Figure 36 without any signs of cracking. The shrinkage of the parts decreased from 18 to 21 percent to approximately 16 percent.

Microstructural observation of the honeycomb samples revealed an increase in the porosity and grain size. Figures 40 and 41 show the microstructures of honeycomb samples produced from powders insufficiently calcined and completely calcined respectively. The pore size shown in Figure 41 is exaggerated because the etching time was 20 seconds while the etching time

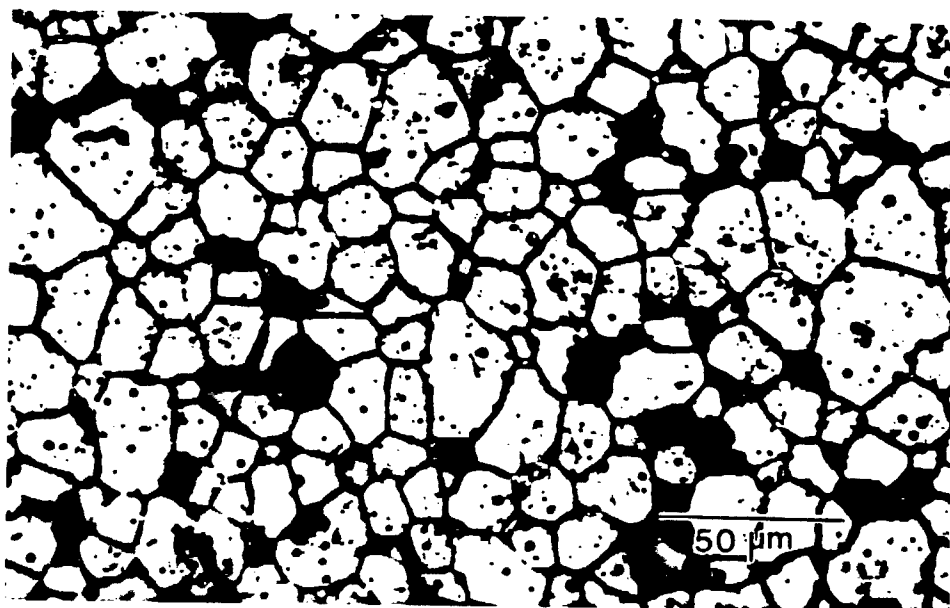


Figure 40: Optical micrograph showing grain size and porosity of a honeycomb sample produced from powder calcined at 700°C. Etching time 5 sec. Dark areas are heavily etched grains.

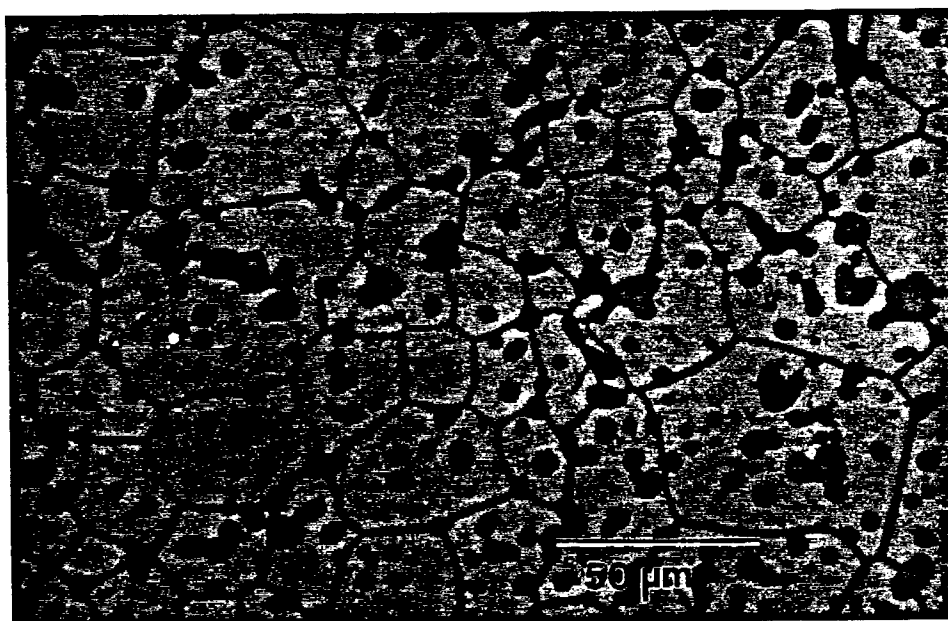


Figure 41: Optical micrograph showing grain size and porosity of a honeycomb sample produced from fully calcined material. Etching time 20 sec.

for the material in Figure 40 was 5 seconds. The average grain size did not increase dramatically but the porosity increased significantly. The average grain size increased to 20 μm from 15.4 μm while the porosity increased to approximately 4.0% from 1.7 %.

Thermogravimetric analysis on the honeycomb material (dry) confirmed that the methycellulose decomposes at approximately 250°C. The TGA results shown in Figure 42 indicate that the weight loss continues to 700°C but at a greatly reduced rate. The total weight loss occurring from the binder burnout is approximately 4.5 % which is in agreement with the amount of binder added (4.0%). The other 0.5% is from the volatilization of the soap. The weight loss from 270°C to 700°C is 0.2 %.

HIGH TEMPERATURE MODULUS OF RUPTURE

The effect of elevated temperatures on a material can have positive or negative effects on the strength of a material. High temperature MOR tests were performed on several sets of bars to determine the effect on the BNO material (data in Appendix E). It was found that the strength decreased as the temperature increased when the samples were brought up to the testing temperature over a five minute period. The rapid heating may have

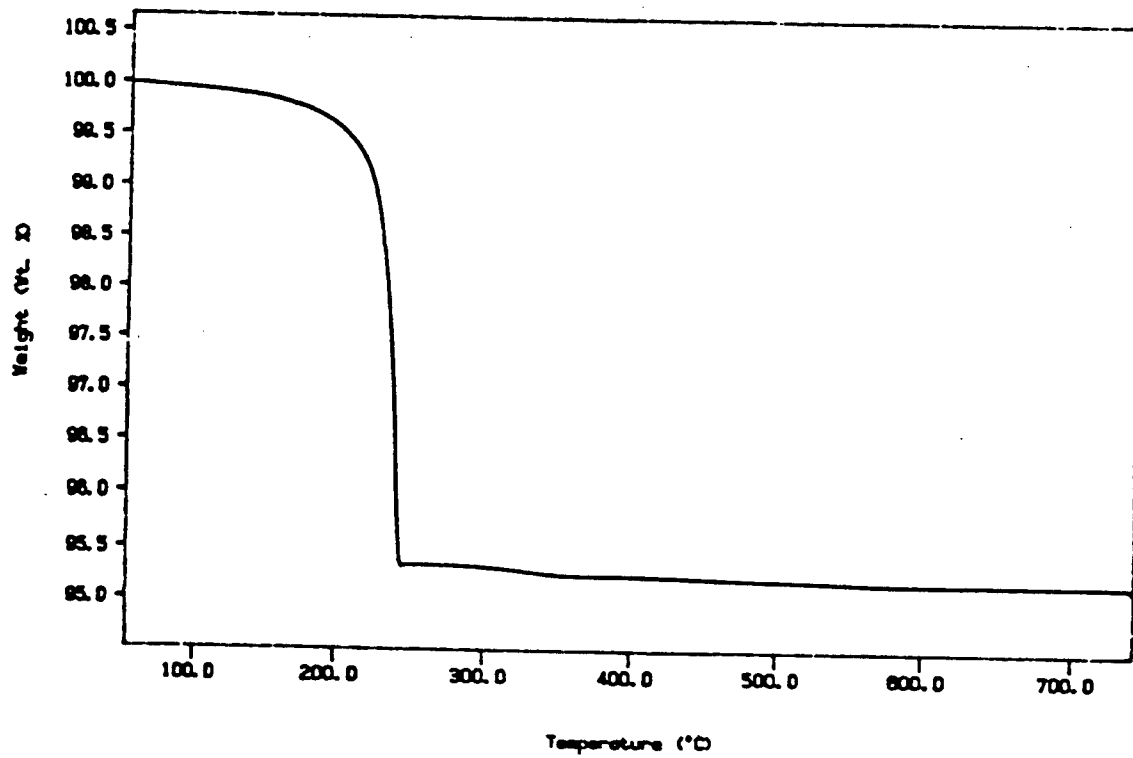


Figure 42: TGA curve for honeycomb material showing weight loss as a function of temperature. The material was dried thoroughly at 98 °C before the TGA test.

caused thermal shock of the material, but this was not pursued due to time constraints. The strength decreased 18 % from 33 MPa at room temperature to 27 MPa at 600⁰C. Figure 43 shows the decrease in strength as a function of temperature. The graph implies that the rate of decrease in strength is reduced at elevated temperatures possibly indicating that creep deformation is starting to have an effect in reducing stress concentration at crack nucleation sites. The tests were carried out at relatively fast rates of loading in order to suppress the effect of creep deformation.

TRANSFORMATION TOUGHENING

Due to the relatively low modulus of rupture and fracture toughness values, partially stabilized zirconia was added as an aid to increase the strength and toughness of the BNO material. Increases in strength on the order of several hundred percent have been observed in some materials. Figure 44 shows the strength of the composites in four point bend as a function of weight percent zirconia. The strength of the composites increased as the amount of stabilized zirconia was increased to 11.6 wt.% (Appendix F). The peak strength occurred at 11.6 wt% zirconia and was 37.5 MPa.

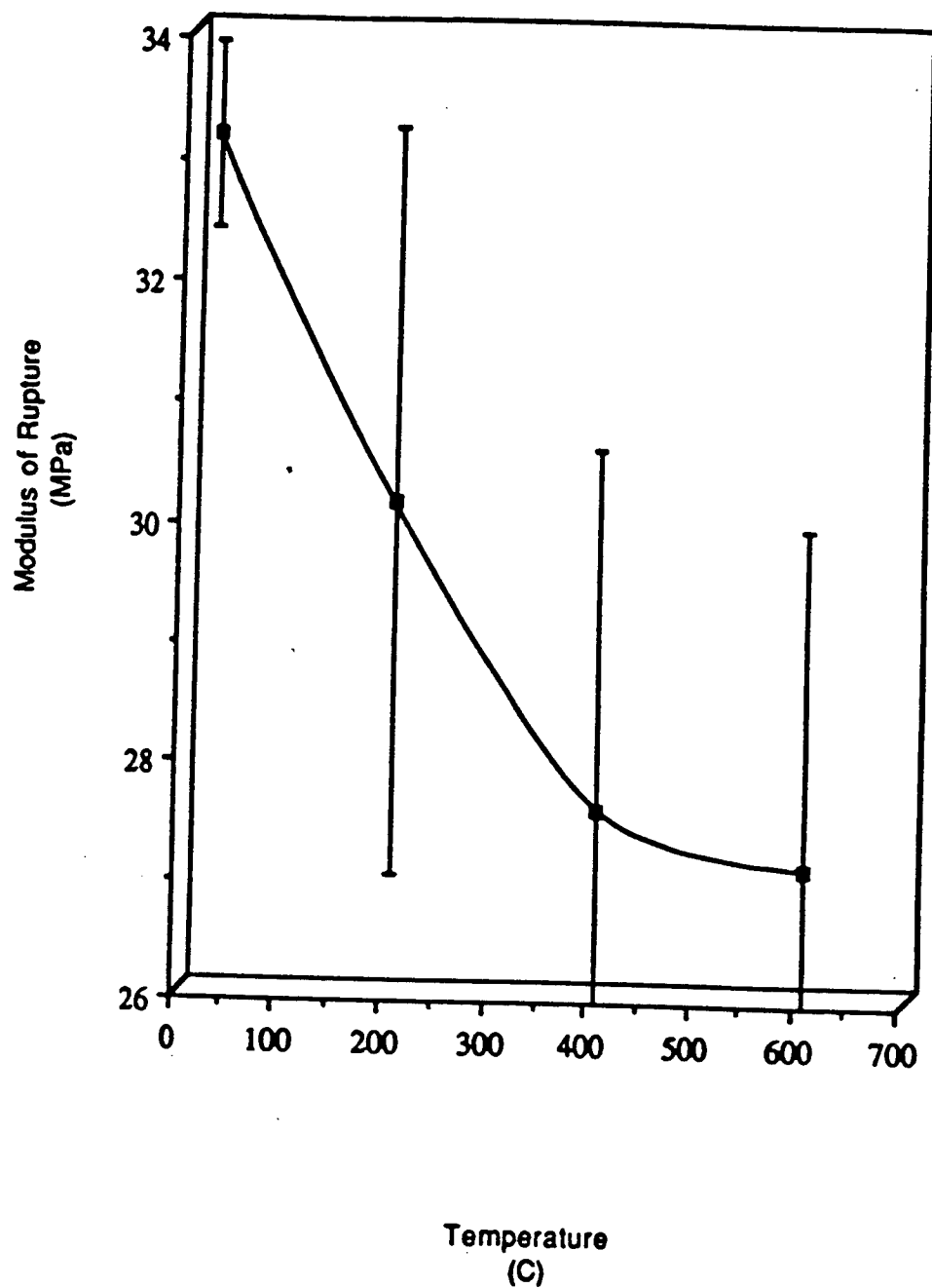


Figure 43: Strength of sintered BNO bodies as a function of temperature. Initial powder was produced by vibratory milling.

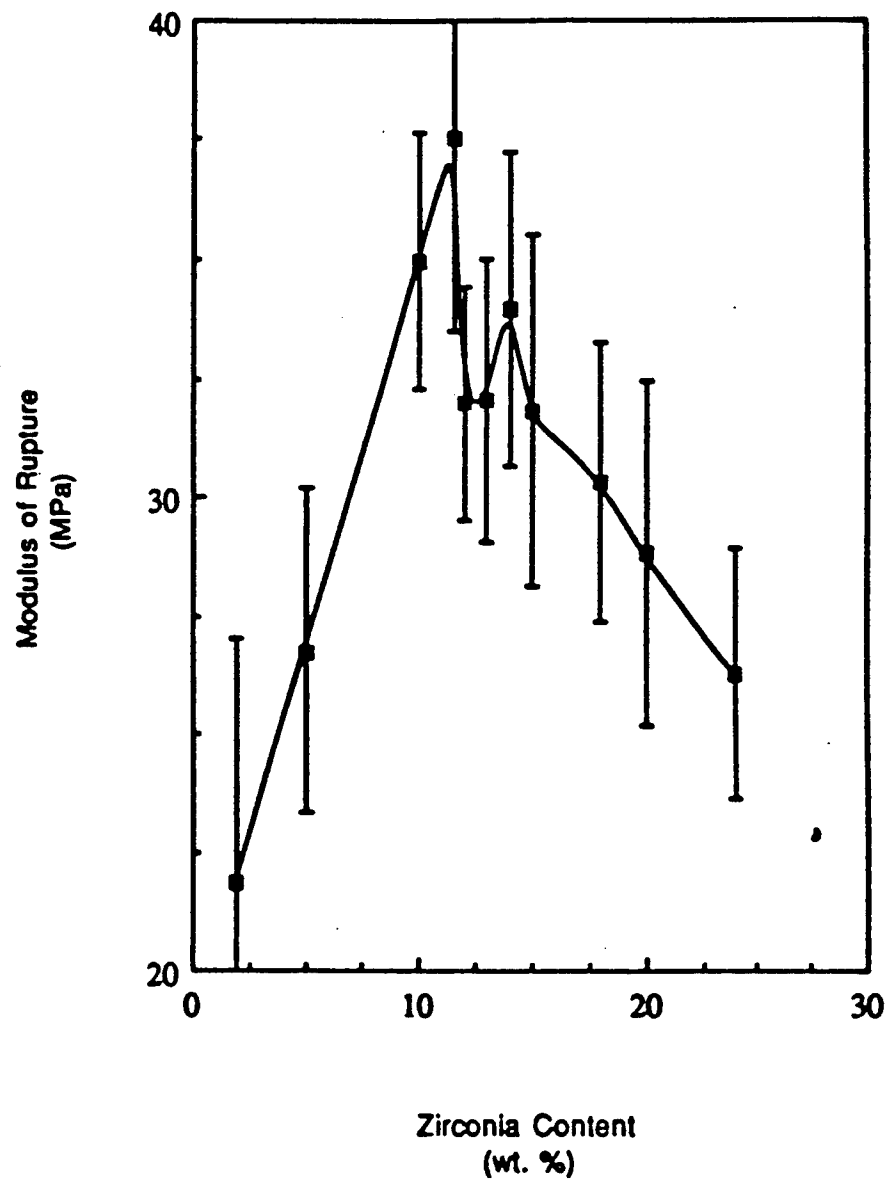


Figure 44: Strength versus weight percent zirconia. Matrix material is the 15 mole% niobia doped bismuth. Error bars indicate one standard deviation.

The increase in modulus of rupture was approximately 25%. The strength then decreased as 24 wt.% zirconia was approached. The modulus of rupture was approximately 26 MPa at a composition of 24 wt.% zirconia.

Representative microstructures are shown in Figures 45 through 48. Several effects on the microstructure can be observed with all the zirconia additions. The large black areas in the photographs are pores ranging in size from 50 μm to several millimeters in length. Areas are present that have an increased amount of porosity relative to the rest of the microstructure. These areas are zirconia rich sections that have not densified during sintering and contain a significant amount of porosity.

These regions are in contrast to areas that appear dense, and are surrounded by an area of increased porosity. The dense regions are bismuth-niobia rich areas that have sintered more rapidly than the surrounding matrix and pulled away from the matrix due to the different shrinkage rates. The extent of areas that are BNO or zirconia rich is large and gets larger as the amount of zirconia is increased. Figures 45 - 48 show several areas of BNO and zirconia rich sections.

The results of electrical conductivity measurements are

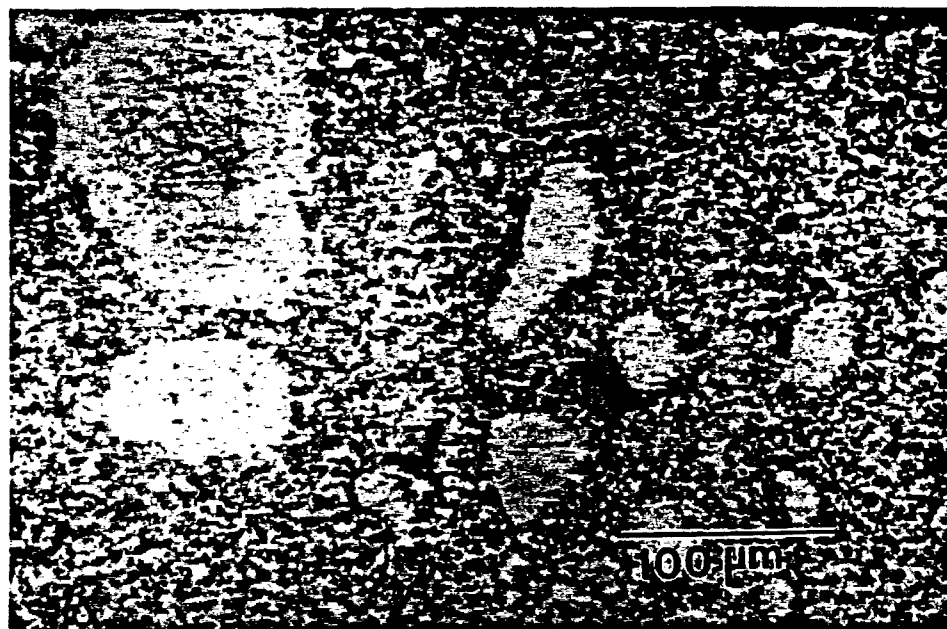


Figure 45: Optical photograph of a BNO bar containing 20 wt. % zirconia. Areas of high BNO concentration are clearly shown.

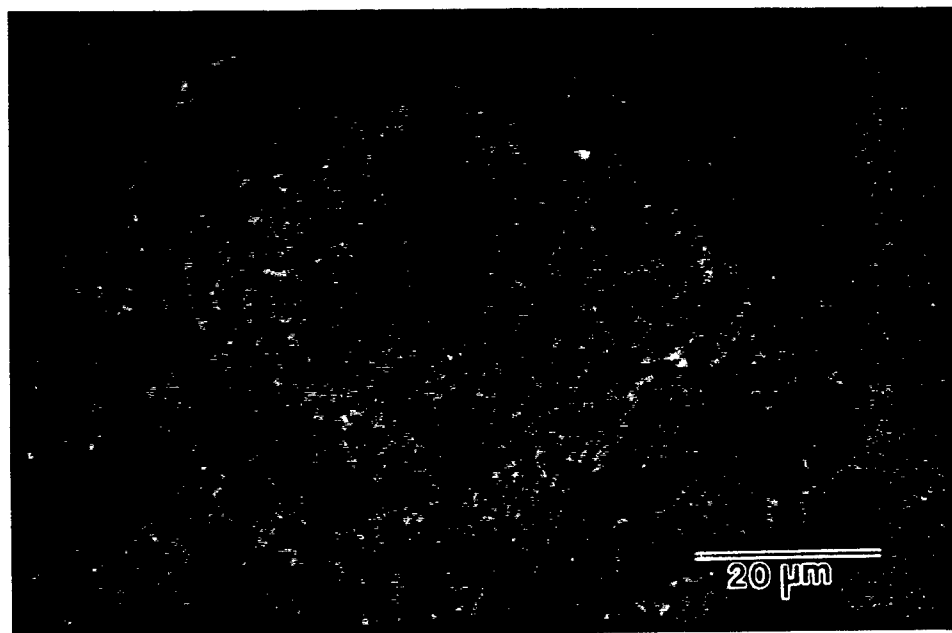


Figure 46: Photograph showing an area of high zirconia concentration (lighter area) in BNO doped with 11.6 wt.% zirconia. Photographed using polarized light.

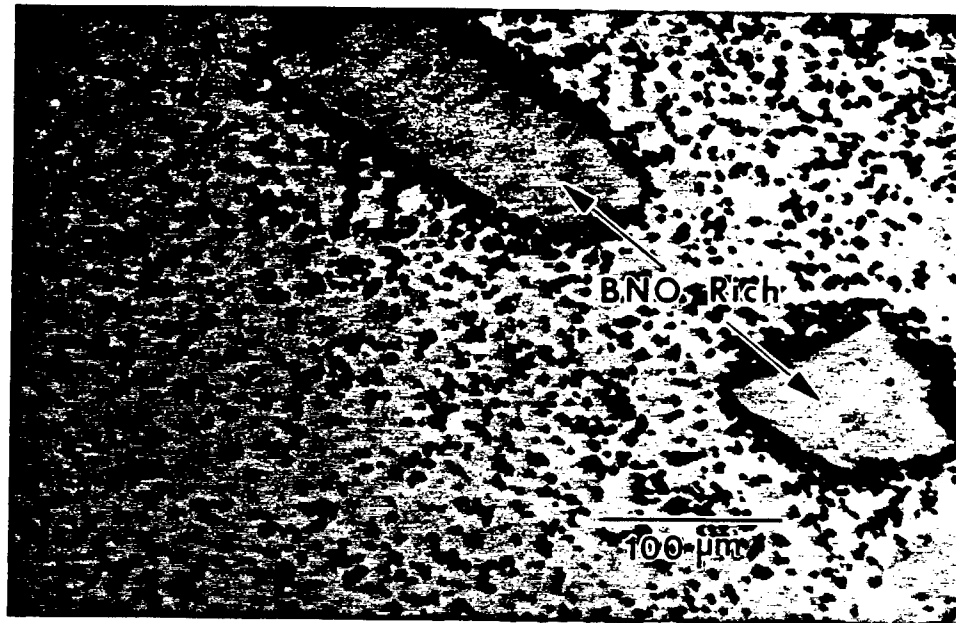


Figure 47: Optical photograph indicating BNO rich areas encompassed by porosity. (11.6 wt. % zirconia).

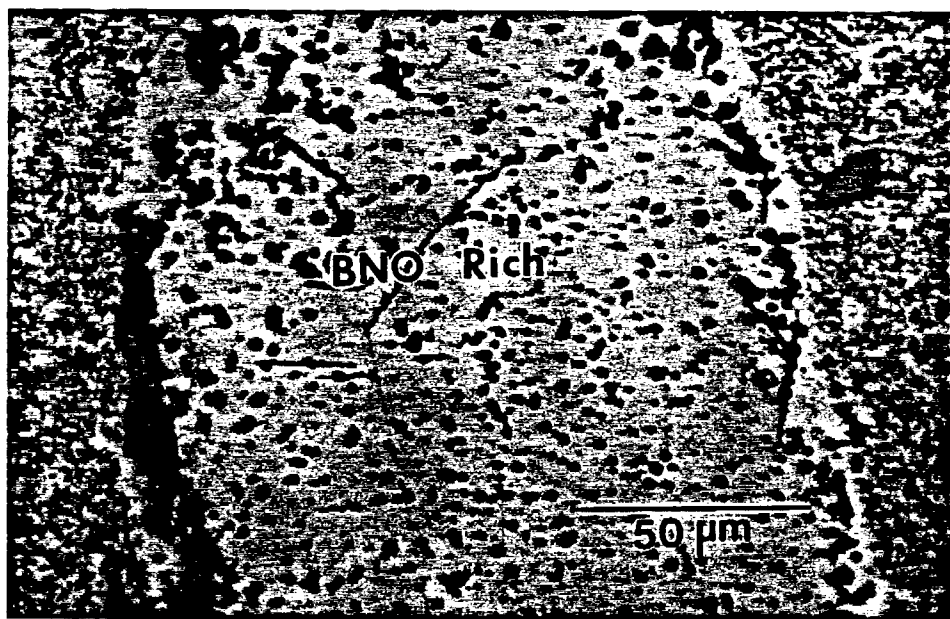


Figure 48: Zirconia doped BNO (20 wt. % zirconia). BNO rich area is indicated.

shown in Figure 49⁵⁵. The conductivity of the BNO is approximately 4-5 times greater than the sample with 11.6 wt.% partially stabilized zirconia. Both plots of conductivity follow an exponential relationship with temperature. The conductivity of other samples were not measured because the main purpose of this study was to determine the maximum strength achievable by the addition of zirconia without degradation of conductivity.

PRECIPITATION TOUGHENING

Reducing the amount of niobia in bismuth oxide reduces the stability of the cubic phase. Compositions containing 6.7, 10, 13, 16.3 and 19.3 mole% niobia were examined for second phase precipitates. These compositions produced similar phases as a result of the heat treatments. The initial calcining of the raw materials was done using a maximum temperature of 700⁰C. The samples were all sintered at 820⁰C except the 12, 13, 14 and 19.3 mole% compositions which were sintered at 915⁰C. The phases found in the samples after heat treatment are listed in Table 5. All samples contained a cubic phase which decreased in concentration as the concentration of niobia decreased. All compositions except

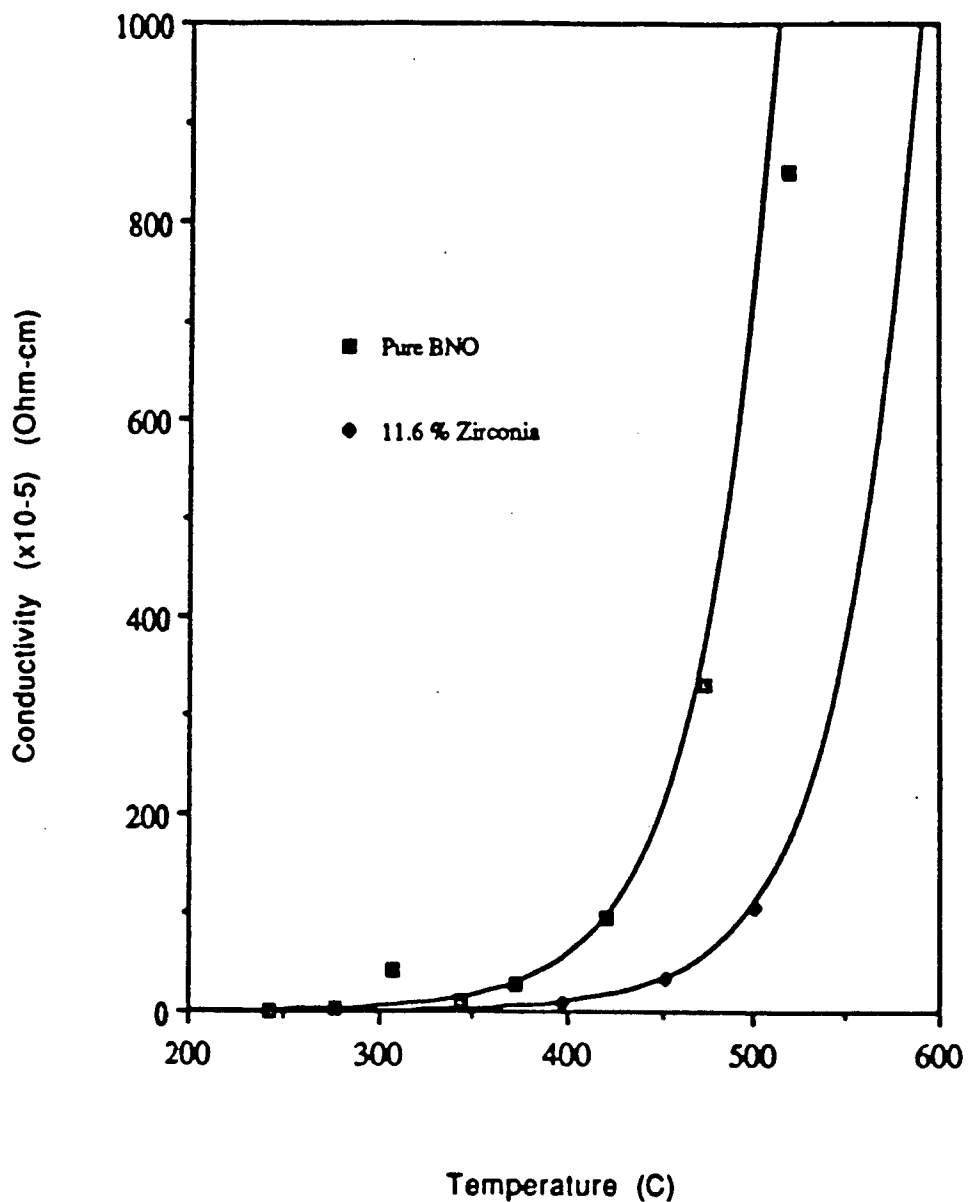


Figure 49: Conductivity versus temperature for pure BNO and BNO doped with zirconia. (measurements performed at CeramPhysics, Westerville, Ohio, Ref. 55)

Table 5: Results of the precipitation toughening study.

Composition (mole% Nb205)	Sintering Temp. (C)	Annealing Time (hours @ 625)	Phases Present*	Strength (MPa)
6.7	820	25	$\alpha, \delta,$	26.38
		50	$\alpha, \delta,$	
		120	$\alpha, \delta,$	
10.0	820	25	$\alpha, \delta,$	25.82
		75	$\alpha, \delta,$	
		105	$\alpha, \delta,$	
		120	$\alpha, \delta,$	
12.0	915	120	δ	32.15
13.0	915	0.00	δ	25.64
		50	δ	
		105	δ	
		120	δ	
14.0	915	120	$\delta,$	29.38
16.3	820	75		40.00
		105	α, δ, δ'	
		120	α, δ, δ'	
19.3	915	75	δ, δ'	23.38
		105	δ, δ'	
		120	δ, δ'	
α is the monoclinic phase δ, δ' are the two cubic phases				

* MOR samples annealed for 120 hrs at 625 C.

those containing 12, 13, 14 and 19.3 mole% niobia also contained at least a small amount of the monoclinic phase. This was most likely carried over from the calcination step.

The highest concentration of niobia contained both the δ and δ' cubic solid solution phases as did the 16.3 mole% composition. The 16 mole% composition contained the cubic phase with some monoclinic and possibly a trace of the tetragonal phase. The 6.7 and 10 mole% niobia compositions contained the monoclinic and cubic phases and possibly a small amount of the tetragonal phase. Compositions having 12, 13 and 14 mole% niobia contained only the FCC (δ) phase when sintered at temperatures of 820 or 915°C.

The strengths of bars made from all compositions were measured using the previously outlined four point bend test. The data is in Appendix G and the strengths of the composites did not exceed the strength of the 15 mole% material (Table 5). The only exception was the 16.3 mole% composition which showed a MOR of 40 MPa with a standard deviation of 10 MPa. Examination of the microstructure of several fracture surfaces of these specimens revealed that defects were the cause of the failure. These flaws were a result of poor processing. Figures 50 and 51 show large flaws on the fracture surface in two samples. The average particle



Figure 50: Surface void causing failure in bismuth doped with 16.3 mole % niobia. Fracture surface of the strongest bar tested. (strength = 60 MPa).

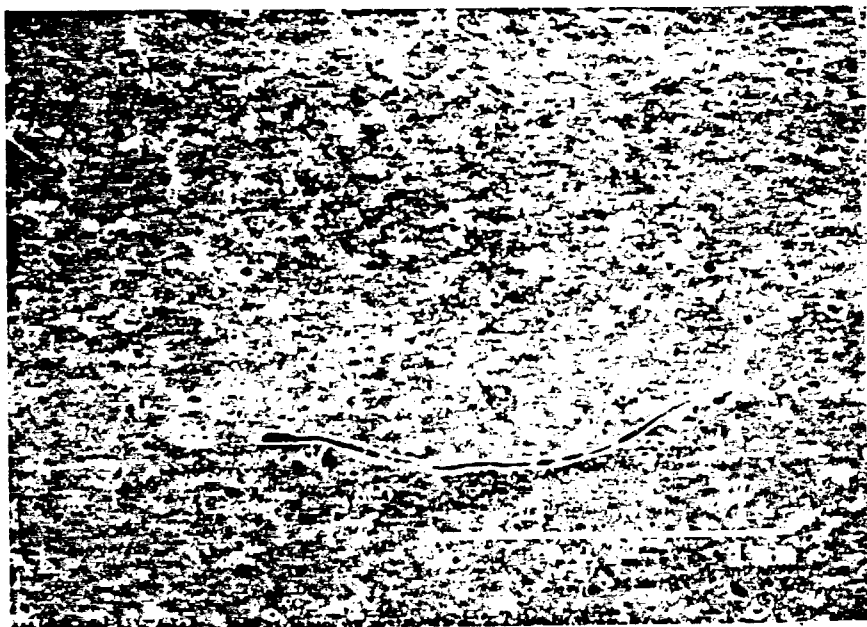
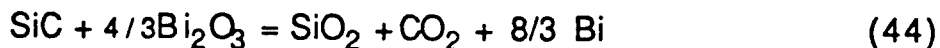


Figure 51: Flaw initiating failure in bismuth doped with 16.3 mole % niobia. Fracture surface of the lowest strength bar pictured (strength = 22 MPa).

size for the starting powder was approximately 20 μm as determined by BET analysis. The ionic conductivity decreased by two orders of magnitude from 3.33×10^{-3} ohm-cm for the 15 mole % BNO to 6.21×10^{-5} ohm-cm in the 16.3 mole% niobia doped bismuth oxide. The drop in conductivity necessarily makes this an unsatisfactory solution even if the microstructure could be improved.

WHISKER REINFORCEMENT

Four weight percent SiC whiskers were added to 15 mole % BNO as a crack tip inhibitor. The results of this study were immediately apparent upon removal from the furnace and were very disappointing. The SiO_2 layer that forms on SiC whiskers reacted with the bismuth oxide to form a eutectic at approximately 800°C . This caused extensive damage to the bars. The release of CO_2 from the reaction



caused foaming of the liquid material and resulted in a hard cake after firing. X-ray diffraction showed that bismuth metal was present after firing. No further studies were done on samples containing the SiC whiskers because of the effects noted above.

FRACTURE TOUGHNESS

Two types of tests as described earlier were used to determine fracture toughness of the sintered bars. The results from the notched beam test gave a toughness of $0.425 \text{ MPa}\cdot\text{m}^{1/2}$. The fracture toughness obtained from the indentation technique is $0.412 \text{ MPa}\cdot\text{m}^{1/2}$, and is almost identical to the value obtained from the notched beam technique. The toughness of ceramics ranges from $0.9 \text{ MPa}\cdot\text{m}^{1/2}$ for a weak material like ZnS to $16.0 \text{ MPa}\cdot\text{m}^{1/2}$ for the composite material WC/Co (12%Co). The fracture toughness for BNO is well below normal values for structural ceramics.

Figure 52 shows the fracture surface of a bar that was tested using the indentation technique. The Vickers' indentation is located at the left side of the photograph. The fracture surface is extremely smooth with only minimal features. Hackle marks, formed by two parallel crack segments traveling on different planes breaking through from one segment to another, were observed periodically throughout the fracture surface and are pointed in the direction of the indent. Hackle marks typically indicate the direction of crack propagation or point toward its source. These hackle marks therefore support the assumption that

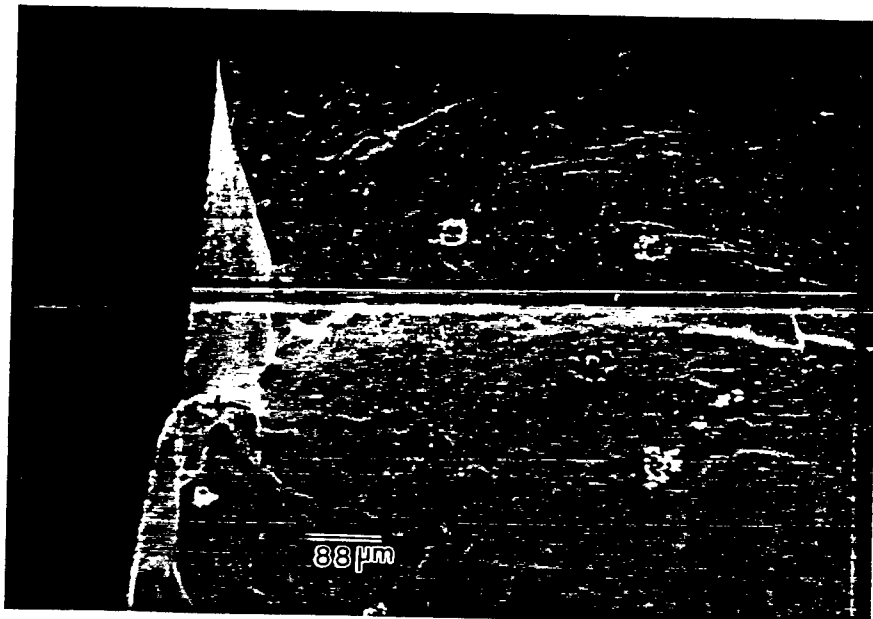


Figure 52: Scanning electron micrograph of a typical fracture surface obtained during fracture toughness measurements. Indentation technique.

the crack originated at the indentation. The magnitude of the hackle marks produced is much larger than the average grain size of 15 μm . This implies that grains do not produce hackle marks and therefore do not interfere with the propagation of the crack.

The theoretical size of the flaw causing failure in several of the materials tested was calculated using Equation (35), an average value of fracture toughness of 0.42 MPa- $\text{m}^{1/2}$ and MOR data. Table 6 shows the results of the calculations and also provides pore and grain sizes as measures of the largest flaws observed. The calculated flaw sizes for the samples produced from ball and vibratory milled powders are much larger than the flaws observed through microscopy. The calculated flaw sizes for the

Table 6: Calculated values for failure causing flaw sizes in several of the materials tested. Also shown are the largest observed defects in the material.

Sample <u>Description</u>	σ_f (MPa)	Flaw Size(μm) (calculated)	Flaw Size(μm) (observed)
Initial Powder - Ball Milled	13.13	270.0	Pore Size = 15-20 Grain Size = 26
Initial Powder -Vib. Milled	33.00	42.6	Pore Size =10-15 Grain Size = 15
Transformation Toughening Samples (lowest MOR)	22.00	95.0	BNO Rich area = 200
Precipitation Toughened Samples (lowest MOR)	23.38	85.0	Processing = 1000 Defect

samples produced from the transformation and precipitation toughened samples were 22 and 23 μm respectively and are much smaller than the largest observed defect. This suggests that the addition of zirconia and the precipitation of a second phase produced a toughening effect because the predicted flaw size is much smaller than the observed defect size. The observed flaw sizes from samples made from ball and vibratory milled powders were smaller by an order of magnitude than the calculated flaw

sizes. This suggests that the failure causing flaws are large processing defects and not the grains or pores.

FINITE ELEMENT ANALYSIS

This section contains a brief review of joint research with P. M. Anderson^{5,6} on the stress analysis of a honeycomb geometry through finite element analysis and analytic elastic methods. This represents a separate part of the overall project to produce solid state oxygen compressors. It is included here because it provides the best criteria on which to judge the adequacy of the strength of the BNO materials for use in an oxygen compressor having a honeycomb geometry. The analysis^{5,7} included the distribution of stress throughout the entire shape and predicted the points of greatest stress where fracture is most likely to occur. Under an internal pressure, the points of maximum stress will be at the corner of the cell (fillet). Figure 53 shows the dimensions of the honeycomb section used in the determination of the stress state.

Under operating conditions, the honeycomb channels will be pressurized in parallel rows. The pressurization of the honeycomb will produce a stress on the walls proportional to the magnitude of the applied pressure. This work determined that the stress

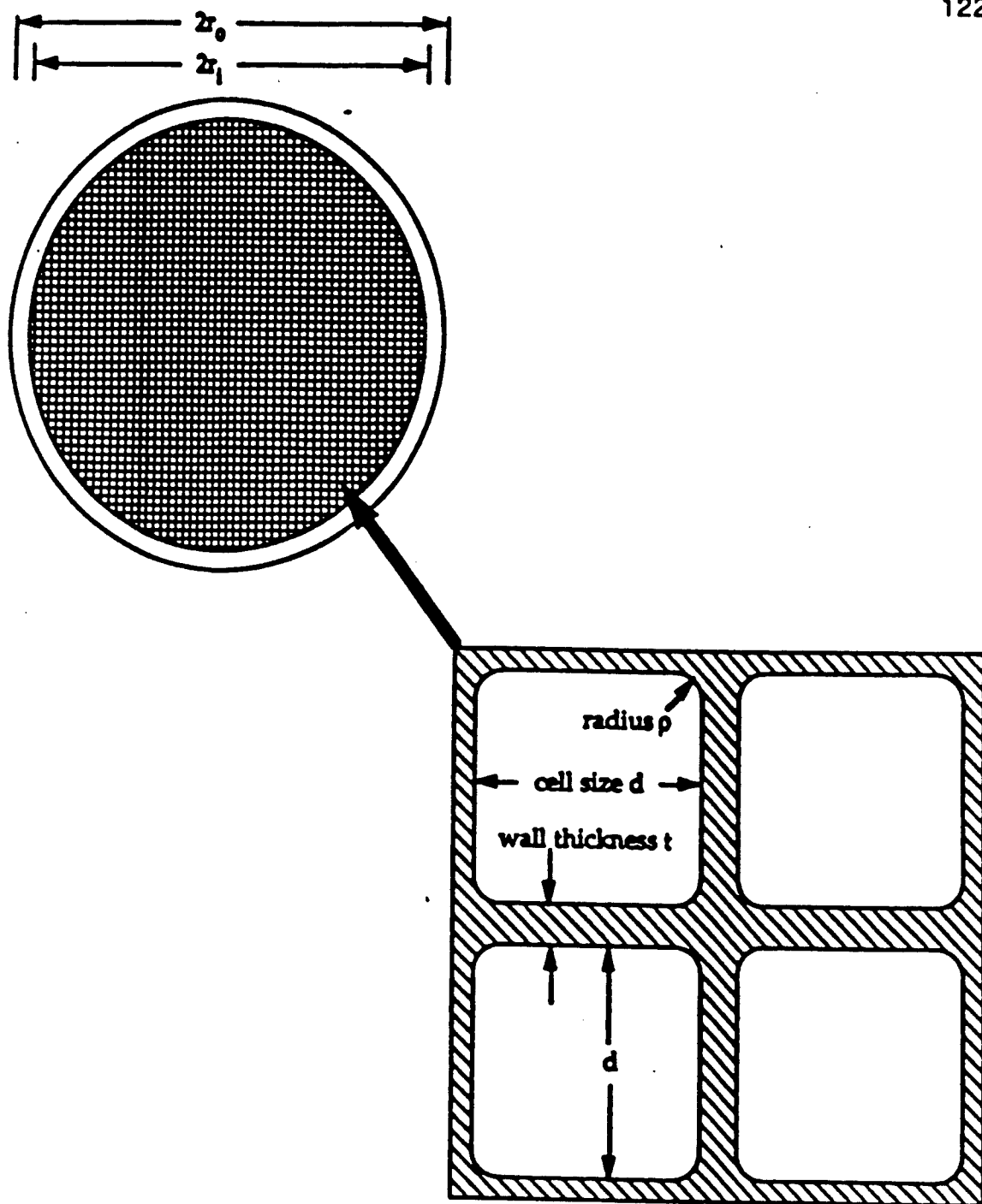


Figure 53: Honeycomb geometry and dimensions.⁵⁶

produced under an applied pressure is dependent on the position and dimensions of the structure. The maximum stress concentration factor will occur on the surface and at the corners of the pressurized cells. The stress concentration factor is defined as the ratio of the maximum principle stress to the applied pressure.

An idealized maximum operating pressure would be defined as the strength of the material divided by the stress concentration factor. The dependence of the stress concentration factor (SCF) at the corners on the normalized cell wall thickness, $\delta = t/d$, and normalized corner radius, p/t , is illustrated in Figure 54. The SCF decreases rapidly as the thickness of the walls increases and more slowly as the radius of the corners are increased. Decreasing the cell width will also decrease the SCF.

Examination of actual extruded honeycombs yielded the cell dimensions and the values are stated in Table 7. The ratios of p/t and t/d vary between 0.042 to 0.063 and 0.41 to 0.43 respectively. Using these values, the calculated SCF at the corners is approximately 16.1. This value represents the SCF at the lowest values of p/t and $\delta = t/d$. The maximum pressure obtainable using the BNO material is calculated by dividing the strength by the stress concentration factor. Using a strength of 33.0 MPa the

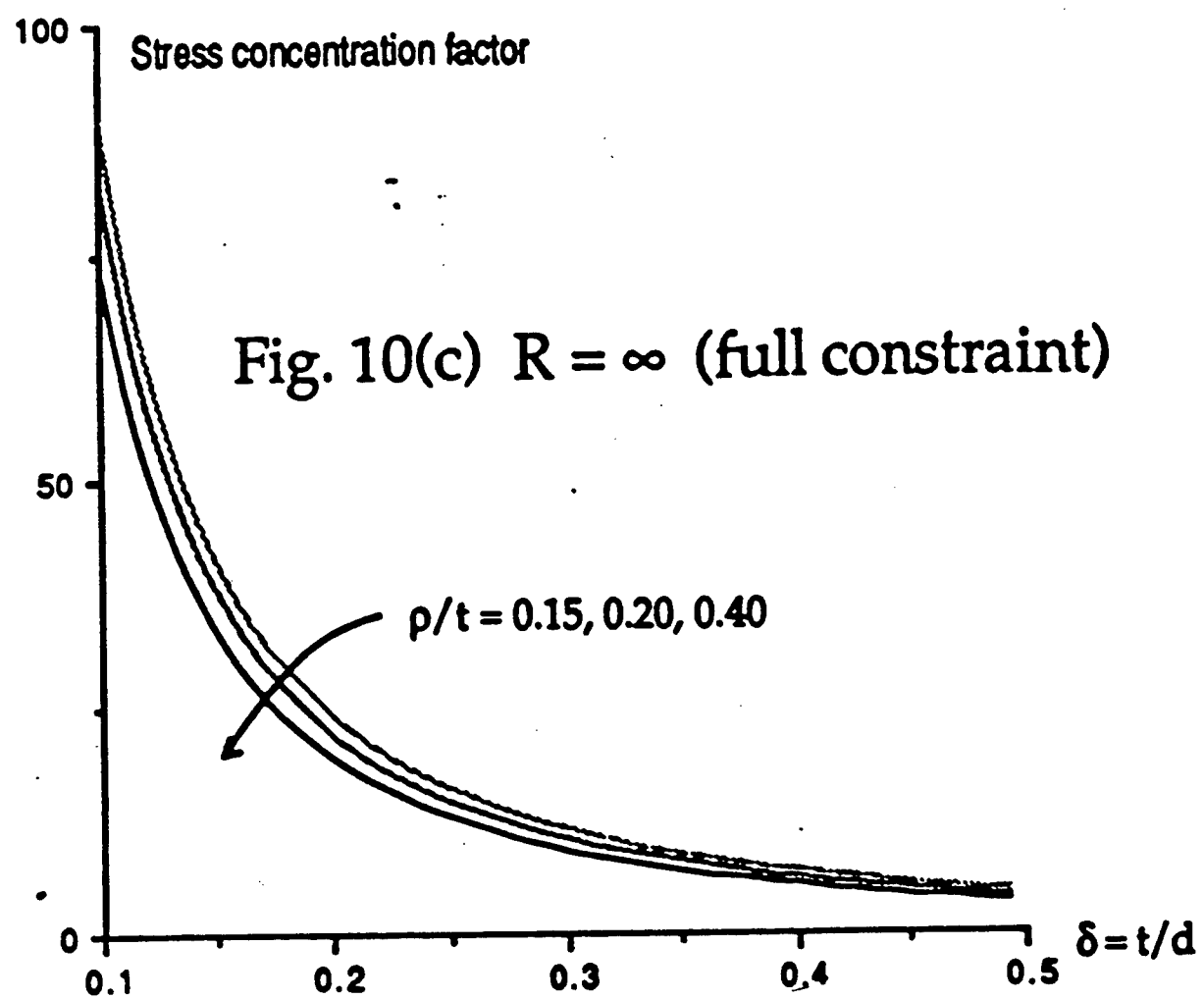


Figure 54: Stress concentration factor as a function of cell dimensions.

Table 7: Measured values for the cell dimensions in the sintered honeycombs. Honeycombs produced from vibratory milled powder and sintered using the rate controlled schedule.

$381.0 \times 10^{-6}m$	$> t >$	$366.0 \times 10^{-6}m$
$8.9 \times 10^{-4}m$	$> d >$	$8.85 \times 10^{-4}m$
$22.5 \mu m$	$> \rho >$	$16.0 \mu m$

maximum pressure obtainable would be approximately 2 MPa or 20 atmospheres. The maximum pressure sustainable at 600°C would be approximately 1.7 MPa or 17 atmospheres. According to Lawless², pressures on the order of 50 - 150 atmospheres are required.

CHAPTER V

DISCUSSION

PARTICLE SIZE REDUCTION

The reduction in particle size was shown to be much more efficient using the vibration milling technique as opposed to the ball milling technique. During the same grinding period the same starting powder was reduced to an average size of $0.16 \mu\text{m}$ in the vibratory mill but only to $2.17 \mu\text{m}$ in conventional ball mills. This is in agreement with Rose et al.⁵¹ who obtained a much greater rate of grinding using vibration milling than conventional ball milling techniques. The particle size versus grinding time followed an exponential function which is in agreement with Smith et al⁵⁰. The rate of grinding, however, had not been optimized in this study and it is possible to increase the effectiveness of the grinding in several ways. Rose found that by (1) using rod shaped

grinding media (2) by increasing the fill volume of the mill to approximately 85% and (3) by increasing the frequency of the mill that the effectiveness of the mill could be improved. These factors were, at the time of this study, unable to be manipulated to obtain the optimum conditions. It is also worth mentioning that the reduction in particle size was sufficient for our needs and that x-ray diffraction showed no detectable contamination due to the grinding media.

The measurement techniques used to determine the particle size were biased in different ways. Using the videoplan, it was very difficult to differentiate between aggregates, agglomerates and single particles due to the small size of the particles. This caused the data to be biased toward a larger average particle size. The BET analysis however, was not influenced by the presence of hard or soft agglomerates due to their open structure and the ability of nitrogen to wet the entire surface area of the particles. The large difference between the two measurements suggests that the amount of agglomeration is relatively high. This is expected due to the tendency of small particles of powder to agglomerate by Van der Waals forces. It is possible that a significant number of hard agglomerates were carried over from the calcination step.

The observed particle size distributions from both techniques

indicated that the vibratory milling produced a narrower distribution than the ball milling. This is in agreement with experimental work done by Summers et al.⁵⁸ who obtained narrow particle size distributions with low amplitude, high frequency vibratory milling methods. The decrease in the particle size and the narrower distribution of vibratory milled powder led to an increase in the firing shrinkage of the components produced from vibratory milled powder. The linear shrinkage for the ball milled powders was approximately 16 percent while the vibratory milled powders produced shrinkages of 18 to 21 percent. The reduction in particle packing efficiency as the distribution narrows reduces the green density. The reduction in green density in turn increases the final firing shrinkage.

The effect of the decrease in particle size on the microstructure and mechanical properties was apparent. The microstructure of the sintered bodies was improved by using vibratory milled powder. The grain size decreased and the density increased when vibratory milled powder was used instead of ball milled powder. Rice et al.³² have shown that the density of a sintered body can depend strongly on the initial particle size. Results of this study showed that bars made from vibratory milled

powder reached a theoretical density of approximately 98.3 % as opposed to 95.0% for those made from ball milled powder.

It has also been shown⁵² that the grain size of sintered specimens is dependent on the initial powder particle size. The microstructure (i.e. grain size, porosity) of the sintered bars improved due to the use of vibratory milling. These improvements can have substantial effects on the mechanical properties. For ball milled material, the average starting particle size of the powder was 2.16 μm , which yielded a grain size of 26 μm in sintered bars. Corresponding values for the vibratory milled powder were 0.1617 μm and 16 μm respectively. The approximately 10:1 difference in particle size had a noticeable effect on the final sintered microstructure.

Improvement of the mechanical properties of the material was a goal of this project. Several authors predicted that a decrease in grain size and porosity can have a positive effect on the mechanical properties. The increase in strength from 13 to 33 MPa as the porosity and grain size decrease is therefore expected. The change in strength in our samples was a result of the change in both the porosity and grain size. According to Knudsen et al.²⁵, the strength decreases with increasing grain size and porosity

according to the relationship given in Equation (47). This relationship describes the variation in strength of several materials with changing grain size and porosity, but the relationship between the strength of BNO and grain size and porosity could not be expressed in this form. The reason the data is poor is because only two data points were taken. Only a general comparison between the strength and grain size and porosity can be made for BNO.

EXTRUSION OF HONEYCOMB GEOMETRIES

The initial batches produced results that did not concur with those later, larger batches. This is not surprising when processing differences are considered. The initial assumption that the water content would be identical throughout the processing of the two batches was in error. The small laboratory scale extrusion runs were done using a hotplate to bring the water to the boiling point (the water was weighed prior to heating). At this point the soap was added and allowed to dissolve completely while on the hotplate. During this time, the water was allowed to boil causing a reduction in the amount of water in the beaker. On this smaller scale, the loss of water quickly becomes significant.

The extrusions requiring large batches used a convection oven

to heat the water to 95°C. The water and soap were then weighed, mixed together and placed back into the convection oven with a cover until the soap dissolved. This eliminated a great deal of the water loss during heating of the separate components. The batch was also kept at a reduced temperature throughout the extrusion process which reduced the vapor pressure of the water during handling and extrusion. The estimated water loss during small scale processing relative to the full scale production is approximately 1 - 1.5 percent. This is the reason it was necessary to optimize the water content by iterations of large batches. Three batches were made which contained 13.5, 14.0 and 15.0 % water. The batches containing 13.5 and 14 % water produced satisfactory results while the batch containing 15 % water produced poor results.

DENSIFICATION OF HONEYCOMB SAMPLES

The encasement of the honeycomb samples by zirconia sand eliminated the severe cracking of the samples during sintering. However, the sand failed to eliminate all the cracking problems encountered. The large firing shrinkage of the honeycomb samples caused cracking problems at the interface between the bottom of

the honeycomb and the setter piece. The cracks were caused by the frictional force between the setter and the honeycomb. As the honeycomb densified, the part was dragged across the surface of the setter causing a tensile force on the honeycomb part. Attempts to reduce the force on the interface by using different sintering arrangements were unsuccessful and even detrimental in some cases. The only other alternative was to reduce the shrinkage of the honeycomb sample to a point were the cracks no longer occurred. This was a result of the increase in particle size. The particle size increased from 0.1617 to 2.0 μm by increasing the calcination temperature from 700 to 800°C. This increase in particle size reduced the shrinkage from approximately 19.5 percent to 16 percent. The decrease in firing shrinkage is in agreement with Cooper⁵² who also saw a reduction in firing shrinkage with an increase in initial particle size. As expected, the grain size and porosity increased as a result of the particle size change.

HIGH TEMPERATURE MODULUS OF RUPTURE

The area of high temperature strength is controversial at the present moment. Some authors have observed a decrease in

strength in alumina above certain temperatures while others predict and observe increased strengths in other materials at elevated temperatures. The decrease in strength in alumina is attributed to the formation of cracks in the material from anisotropic thermal expansion of the grains. The increase in strength is due to crack tip blunting. The material studied in this work showed a decrease in the strength of approximately 18 percent at 600°C. The strength decrease is sharp at first, then appears to level off at 600°C.

Several authors reported a lack of any temperature dependence on strength until temperatures above 600°C were reached. The discrepancy between the literature and our results can be explained by normalizing the testing temperatures to the melting points of the materials. The melting point of BNO is much lower than the melting points of the materials studied in other works. The testing temperatures represent 22, 44 and 66 percent of the melting point. The reported effects of temperature on strength in the literature begin at approximately 400-600 °C which is only 14 to 21 percent of the melting point of pure MgO (2800°C) and 22 - 33 percent of the melting temperature for Al_2O_3 .

(1800°C). It therefore follows that under these conditions one would expect to see a temperature effect on strength in BNO.

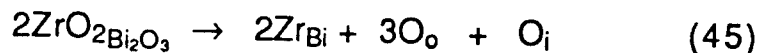
FRACTURE TOUGHNESS

The results of the fracture toughness tests on the BNO material, performed using two different techniques, were surprisingly close. The average values obtained from the indentation and notched beam techniques were 0.4118 and 0.425 MPa-m^{1/2} respectively with a difference of only .013 MPa-m^{1/2} which for all practical purposes is insignificant. Petersson and Bergman⁵⁹ reported that the same two fracture toughness techniques yielded significantly different results on alumina-zirconia materials. Furthermore, Petersson et al. determined that the indentation method developed by Anstis⁴⁸ was the most reliable method available. This method was used in the current study and the value obtained seems reasonable due to the very fragile nature of the material. In comparison with other materials such as a lead borate glass (20.3 mole% PbO) and a soda lime silicate glass with fracture toughness values of 0.906 and 0.8 MPa-m^{1/2} and modulus of ruptures of 55 and 44 MPa respectively⁶⁰, BNO

has physical properties closer to glasses than a structural ceramic such as magnesia or alumina. Magnesia and alumina have MOR values of approximately 130 and 275 MPa and fracture toughness values of approximately 4.5 and 5.0 MPa-m^{1/2} respectively⁶¹. No data was available in the literature concerning the toughness or strength of bismuth oxide.

TRANSFORMATION TOUGHENING

The results from the transformation toughening study gave little hope for application of this material. The strength did increase but not without decreasing the conductivity significantly. The reason behind the lowering of the conductivity is several fold. First, as the zirconia substitutes into the BNO lattice, the oxygen vacancy concentration decreases as follows.



The oxygen interstitial interacts by Equation (46) with the vacant oxygen sites and reduces the concentration of these sites. This lowers the mobility of the conducting oxygen remaining in the lattice since the probability of finding a vacancy into which the

oxygen ion can jump is reduced.

The addition of zirconia to the matrix of BNO caused a serious degradation in the microstructure. Large porous zones formed due to zirconia rich sections while highly dense regions of BNO were surrounded by void space. The defects in the microstructure caused by the zirconia additions are very large.

Lange and Hirlinger⁶² reported the hindrance of grain growth due to the addition of zirconia particles in alumina. They stated that the zirconia additions exerted a dragging force at four grain junctions which limited the grain growth. A similar mechanism may be the case for the BNO material. The observation of the microstructure indicates that densification is greatly inhibited in these composites. Figures 45 through 48 show SEM photographs of the microstructures of several zirconia doped samples. Notice the extreme amount of porosity contained in the sample.

The mechanism by which strengthening is increased is not one that is easily understood. Transformation toughening is not a likely possibility because of the microstructure. The formation of a transformation zone is dependent on the crack tip stress zone. The relative magnitude and size of the zone is highly dependent on the surrounding material which in this case is very porous and

therefore the crack would propagate through the pores as often as possible. The ability of the second phase zirconia to deflect the crack would also be of little importance due to the overwhelmingly large percentage of porosity. Much more work is needed in this area to determine the cause of the porosity and the mechanical properties of zirconia doped BNO. This work, however, is outside the scope of this research and is a major project in itself. Due to the decrease in conductivity and the relatively small increase in strength, further studies were not carried out.

PRECIPITATION TOUGHENING

The results of the precipitation study agreed more closely with Powers¹⁴ work than that of Roth and Waring¹². The 6.7, 10 and 16.3% niobia compositions all contained the monoclinic Bi_2O_3 phase. This phase was expected from both the Roth and Waring and Powers phase diagrams for samples having 10% or less niobia. The 16.3 mole% niobia composition contained the monoclinic Bi_2O_3 phase which was not expected from the phase diagram. This was most likely a carryover of the monoclinic Bi_2O_3 phase from the incompletely calcined material. The agreement with Powers is attributed to the similarities in the processing of

the samples. The decrease in conductivity in the 16.3 mole% niobia composition may be due to the presence of monoclinic phase, which is not an oxygen ion conductor.

The strength of the material was a disappointment. The tetragonal phase did not precipitate out as was hoped and the conductivity decreased by a factor of two in the strongest material. The precipitation of a tetragonal second phase may hold promise but it seems unlikely. Firstly, the tetragonal phase is metastable and it exists only over a small range of compositions and temperatures. The operating temperature of the compressor would be around 600°C, a temperature at which the monoclinic phase is stable. Thus there is a problem in obtaining bodies with significant amounts of the tetragonal phase. Secondly, the phase transformation from tetragonal to monoclinic may not occur under the same conditions as the strengthening transformation in zirconia. At this point, the application of precipitation strengthening is not a promising solution because of the significant decrease in the conductivity.

WHISKER REINFORCEMENT

The idea of reinforcing the matrix with SiC whiskers had

disastrous results. The formation of the eutectic at 800⁰C assured that this will not work. This will most likely be the case with any second phase particulate or whisker in contact with the matrix. Bismuth oxide is very reactive at elevated temperatures, so much so, that a reaction with platinum was observed at approximately 800⁰C. At this point in time, all of the second phases introduced into the BNO matrix have been detrimental to the conductivity or to the mechanical properties.

FINITE ELEMENT ANALYSIS

Using approximate analytic elasticity methods, honeycomb cell dimensions and finite element analysis, it was possible to determine the pressure which the honeycomb geometry could sustain during operation. The pressure sustainable at room temperature is predicted to be approximately 2.0 MPa while at a temperature of 600⁰C this is reduced to approximately 1.7 MPa. This is approximately five to seven times lower than the operating pressures of 10 to 15 MPa that are required for satisfactory performance of the cryocoolers. The maximum operating pressure can be increased by altering the geometry of the honeycomb cells. Increasing the wall thickness and the radius at the corners will

effect the maximum SCF. The increase in wall thickness is not an option because of conduction problems. The resistivity is a function of the wall thickness and an increase in the wall thickness would mean an increase in the power needed to generate oxygen.

The fillet radius where cell walls meet, may be enlarged with only a minimal effect on the conductivity. Several attempts have been made to increase the fillets by honing the die. An abrasive extrudable material* was passed through the smaller die layout to determine if it would be effective in increasing the radius at the corner of the cells. The properties of the honing material produced a problem during the extrusion. Under normal circumstances, the material would pass into half of the cells first and then knit to form the full honeycomb geometry before exiting the die. The extrudehone material did not knit and thus came into contact with only half of the cell corners. Several attempts were made to hone the die with different grades of the abrasive material. All test runs produced the same results where only half of the cell corners were in contact with the abrasive media.

* Extrudehone Inc., Irwin, Pa.

CHAPTER VI

RECOMMENDED FUTURE WORK

The work presented here has shown the incompatibility of BNO with several different materials. Additional studies should be done on the compatibility of BNO with other materials for possible use as toughening agents. Ceramics with matrix strengths comparable to BNO have seen increases on the order of three hundred percent when a second phase has been introduced. It has been reported that Al_2O_3 has a failure strength of 40 MPa without reinforcement⁶¹. The introduction of PSZ (partially stabilized zirconia) with an average particle size of 0.2 to 1.0 μm increased the strength to 120 MPa⁶³. Although the reaction between BNO and zirconia reduces the conductivity to an undesirable point, other materials remain to be tested. Silicon nitride, boron carbide and others are readily available and warrant study. An increase in strength by three hundred percent would increase the working pressure of the compressor to 60 atmospheres which would still be below optimum pressures but sufficient to produce adequate

cooling.

It would be useful to examine other ways to improve the mechanical properties of the BNO material. Kenny Associates have hot isostatically pressed BNO samples. They observed an increase in density to 100% theoretical with no decrease in conductivity. This preliminary work implies that the improvement of the microstructure through hot isostatic pressing holds promise. It is felt that hot isostatic pressing will only be a partial solution to the problem because the improved microstructure most likely will not produce a large enough increase in strength.

Additional studies on the relationship between flow patterns and die design and material properties should be performed. The information on flow patterns would have significance in designing future dies for other compositions and materials.

Stability of BNO compositions is an important issue. The extended application of the compressor at elevated temperatures and atmospheres will depend on the relative stability of the phases present. A closer look at phase stability in different oxygen activities would be very important in this type of application. Further study in this area is needed to assure reliability of the oxygen compressor.

APPENDIX A

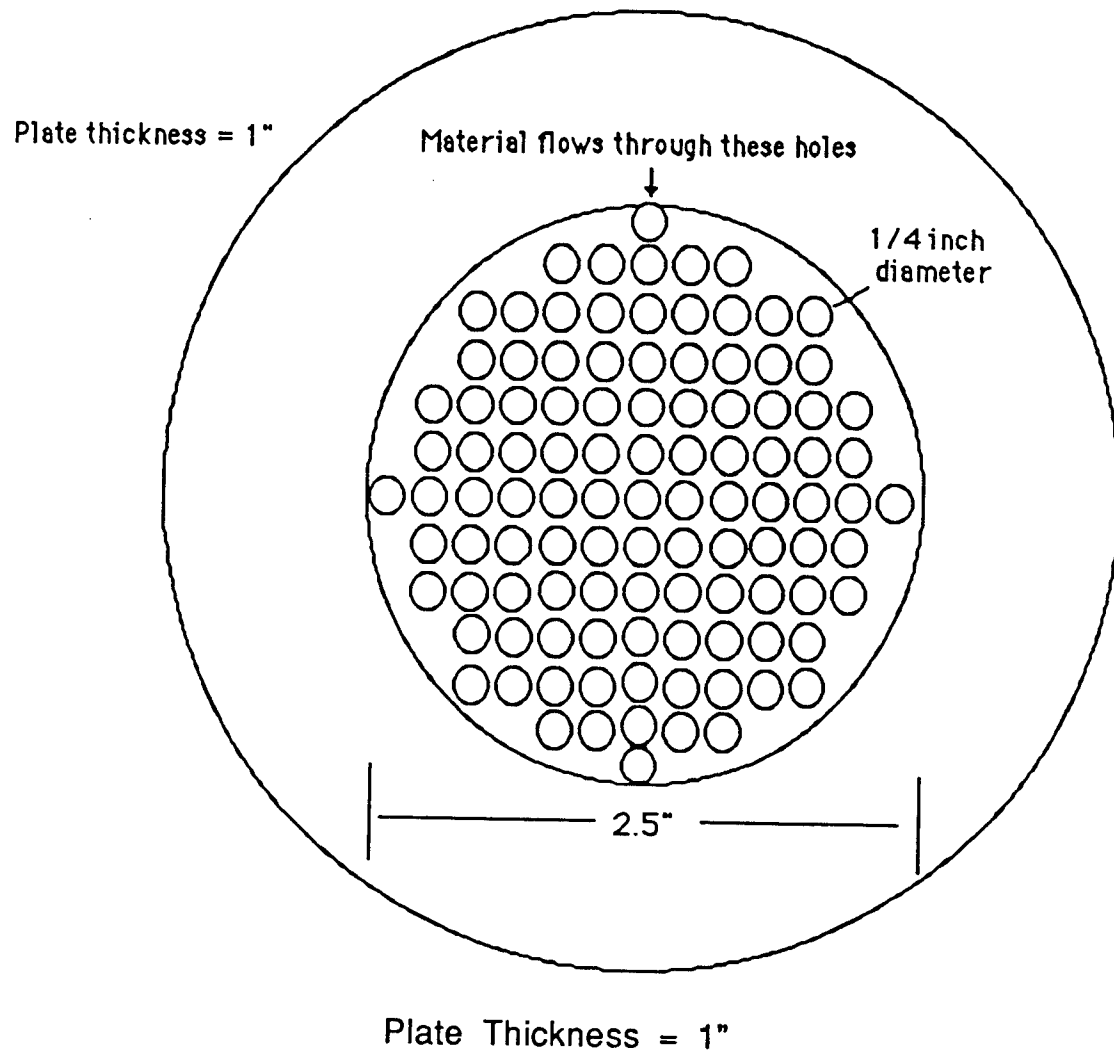


Figure 55: Homogenizer Plate

APPENDIX B

Raw Data for Modulus of Rupture Measurements

Samples made from ball milled powder

Sample Thickness (mm)	Sample Width (mm)	Load at Failure (Kg)	MOR (MPa)
3.61	4.58	3.11	14.36
3.58	4.59	1.91	8.90
3.64	4.59	3.00	13.52
3.65	4.66	2.89	12.80
3.64	4.57	3.07	13.87
3.70	4.59	3.14	13.76
3.72	4.59	2.82	13.49
3.64	4.55	3.15	12.21
3.63	4.59	2.78	12.80
3.64	4.55	2.82	14.41
3.67	4.58	5.02	12.81
3.65	4.55	2.93	12.76
3.64	4.53	2.91	22.40
3.70	4.56	2.85	13.29
3.65	4.55	2.58	13.33
3.68	4.59	3.15	12.55
3.64	4.54	2.95	11.70
3.67	4.59	3.77	13.96
3.68	4.57	3.14	13.51
3.64	4.57	2.64	16.70
3.61	4.54	2.95	13.97
3.67	4.54	3.17	12.02
3.73	4.59	2.55	13.74
3.63	4.54	2.77	14.27
3.68	4.55	2.89	11.04

APPENDIX B (cont.)

Sample Thickness (mm)	Sample Width (mm)	Load at Failure (Kg)	MOR (MPa)
3.60	4.57	3.17	12.74
3.68	4.59	3.52	12.90
3.65	4.58	2.67	14.73
3.67	4.50	2.67	15.58
3.67	4.59	1.67	12.05
3.69	4.66	3.69	12.13
3.69	4.52	2.89	7.41
3.72	4.58	2.83	16.01
3.70	4.50	3.24	12.91
3.72	4.58	3.02	12.29
3.68	4.58	3.64	14.46
3.68	4.61	2.43	13.12
3.68	4.58	2.97	16.15
7.28	4.59	11.27	10.27

APPENDIX C

Raw Data for Modulus of Rupture Measurements

Samples made from vibratory milled powder

Sample	Sample		
Thickness (mm)	Width (mm)	Load at Failure (Kg)	MOR (MPa)
3.98	4.31	7.41	25.30
4.02	4.33	6.01	23.15
3.96	4.29	6.53	26.35
4.02	4.33	7.49	28.98
4.06	4.31	8.04	21.00
4.00	4.31	5.58	21.90
3.96	4.31	9.74	21.80
3.92	4.34	5.31	40.85
3.94	4.34	10.05	43.51
3.89	4.34	10.49	29.54
3.91	4.33	7.12	28.63
3.89	4.39	6.90	25.41
3.96	4.35	6.39	38.14
3.93	4.34	9.34	26.25
3.87	4.33	6.24	35.22
3.91	4.34	8.55	45.08
3.91	4.34	9.37	35.89
3.93	4.36	11.22	30.45
3.93	4.33	8.79	33.14
4.01	4.33	7.74	40.04
3.93	4.35	8.17	37.49
3.97	4.31	9.92	48.00
3.93	4.33	9.15	32.05
3.91	4.34	11.77	23.19
3.91	4.33	7.79	44.66

APPENDIX C (cont.)

Sample Thickness (mm)	Sample Width (mm)	Load at Failure (Kg)	MOR (MPa)
3.97	4.31	5.77	36.08
3.92	4.33	10.83	44.37
3.92	4.31	8.77	28.36
3.91	4.34	10.76	34.37
3.94	4.31	6.95	31.18
3.96	4.34	8.51	25.78
3.96	4.34	7.73	32.56
3.93	4.30	6.23	44.08
3.88	4.33	7.61	30.58
3.86	4.34	10.44	33.58
3.89	4.35	7.33	45.97
3.93	4.30	8.13	29.34
3.91	4.31	11.05	35.48
3.98	4.35	7.38	34.90
3.94	4.35	8.75	35.61

APPENDIX D

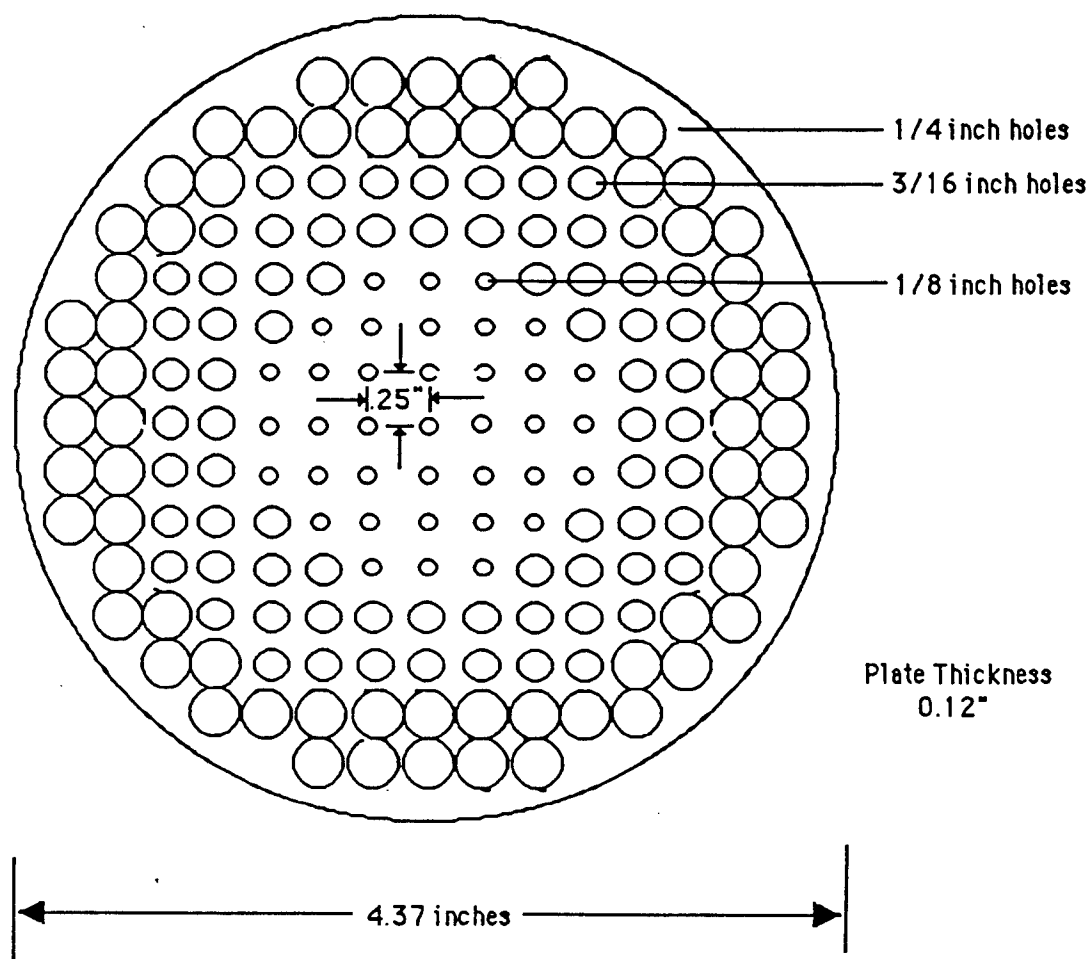


Figure 56: Flow restrictor plate

APPENDIX E

Raw Data for Modulus of Rupture Measurements

High Temperature Tests

Testing Temperature = 200°C

Sample Thickness (mm)	Sample Width (mm)	Load at Failure (Kg)	MOR (MPa)
4.88	4.43	9.82	26.20
5.09	4.36	13.83	34.50
4.85	4.40	9.49	25.83
4.74	4.41	9.37	26.64
4.86	4.35	14.70	40.31
5.01	4.40	9.46	24.13
5.08	4.40	12.48	30.97
4.94	4.40	14.94	39.20
5.13	4.43	11.30	27.31
4.99	4.44	13.09	33.36
3.72	4.38	4.34	20.16
4.59	4.36	10.59	32.48

Testing Temperature = 400°C

Sample Thickness (mm)	Sample Width (mm)	Load at Failure (Kg)	MOR (MPa)
4.91	4.41	10.11	26.79
4.17	4.44	6.90	25.18

APPENDIX E (cont.)

400°C (cont.)

Sample Thickness (mm)	Sample Width (mm)	Load at Failure (Kg)	MOR (MPa)
3.70	4.41	6.19	28.88
5.08	4.38	12.54	31.47
4.68	4.38	7.01	20.86
4.86	4.43	11.34	30.54
5.11	4.44	13.36	32.47
4.85	4.47	8.90	23.85
4.72	4.41	12.91	37.02
4.17	4.31	5.71	21.45
5.33	4.36	10.63	24.18

Testing Temperature = 600°C

Sample Thickness (mm)	Sample Width (mm)	Load at Failure (Kg)	MOR (MPa)
4.82	4.39	10.72	29.61
3.78	4.43	6.60	29.40
5.02	4.39	10.86	27.66
4.36	4.43	9.75	32.65
4.52	4.41	9.06	28.33
5.01	4.40	11.18	28.52
4.52	4.45	5.28	16.35
3.75	4.41	6.03	27.40
3.97	4.40	5.11	20.78
4.95	4.41	11.48	29.93

APPENDIX F

Raw Data for Modulus of Rupture Measurements

Transformation toughened samples

2 wt. % Zirconia additions

Sample Thickness (mm)	Sample Width (mm)	Load at Failure (Kg)	MOR (MPa)
3.91	4.22	6.07	26.84
4.07	4.20	6.67	27.36
4.11	4.20	4.71	18.95
4.02	4.19	5.30	26.56
4.07	4.20	4.44	18.22
4.02	4.19	3.93	16.56
3.92	4.21	6.36	33.17
4.03	4.20	3.77	15.77
4.07	4.20	4.43	18.17

5 wt. % Zirconia additions

Sample Thickness (mm)	Sample Width (mm)	Load at Failure (Kg)	MOR (MPa)
4.19	4.21	8.26	31.87
4.14	4.20	6.05	24.00
4.34	4.19	6.60	23.87
4.25	4.20	6.80	25.60
4.21	4.21	8.26	31.62

APPENDIX F (cont.)

Sample Thickness (mm)	Sample Width (mm)	Load at Failure (Kg)	MOR (MPa)
4.05	4.22	6.06	25.01
4.19	4.25	7.73	29.57
4.11	4.19	7.04	28.41
4.12	4.19	5.43	21.81
4.12	4.20	6.64	25.78

10 wt. % Zirconia additions

Sample Thickness (mm)	Sample Width (mm)	Load at Failure (Kg)	MOR (MPa)
4.57	4.19	9.34	30.46
4.38	4.21	9.05	31.97
4.50	4.21	10.15	36.82
4.54	4.22	11.81	38.75
4.59	4.24	10.44	33.35
3.96	4.22	8.23	35.48
4.43	4.17	9.80	34.17
4.39	4.15	10.21	36.43
4.50	4.16	10.97	37.16

11.6 wt. % Zirconia additions

Sample Thickness (mm)	Sample Width (mm)	Load at Failure (Kg)	MOR (MPa)
4.35	4.19	11.25	40.49
4.36	4.20	8.34	29.80
4.36	4.20	10.38	37.12
4.43	4.17	10.48	36.55
4.40	4.16	10.89	38.59
4.44	4.16	12.51	43.53
4.36	4.20	11.48	41.03

Sample Thickness (mm)	Sample Width (mm)	Load at Failure (Kg)	MOR (MPa)
4.41	4.19	10.09	35.33
4.43	4.19	9.52	33.03
4.22	4.22	10.28	39.04

12 wt. % Zirconia additions

Sample Thickness (mm)	Sample Width (mm)	Load at Failure (Kg)	MOR (MPa)
4.53	4.35	9.53	29.42
4.38	4.38	8.73	28.61
4.39	4.35	9.62	31.63
4.43	4.35	9.95	32.10
4.58	4.36	10.42	31.40
4.47	4.35	10.40	32.97
4.57	4.36	11.11	33.62
4.44	4.38	10.70	34.18
4.39	4.43	11.30	36.47
4.43	4.36	9.10	29.31

13 wt. % Zirconia additions

Sample Thickness (mm)	Sample Width (mm)	Load at Failure (Kg)	MOR (MPa)
4.44	4.40	9.65	30.66
4.35	4.39	8.40	27.88
4.17	4.40	9.03	32.53
4.31	4.41	9.43	31.74
4.35	4.38	8.57	28.52
4.31	4.40	8.73	29.42
4.29	4.43	9.67	32.66
4.27	4.40	10.50	35.71

APPENDIX F (cont.)

Sample Thickness (mm)	Sample Width (mm)	Load at Failure (Kg)	MOR (MPa)
4.29	4.43	10.34	34.94
4.40	4.41	11.23	36.25

14 wt. % Zirconia additions

Sample Thickness (mm)	Sample Width (mm)	Load at Failure (Kg)	MOR (MPa)
4.35	4.41	9.95	32.84
4.53	4.43	11.70	45.47
4.35	4.47	10.86	35.38
4.33	4.43	8.42	27.92
4.39	4.41	10.36	33.59
4.39	4.43	9.99	32.23
4.35	4.40	11.50	38.06
4.38	4.41	11.79	38.40
4.34	4.43	9.58	31.60

15 wt. % Zirconia additions

Sample Thickness (mm)	Sample Width (mm)	Load at Failure (Kg)	MOR (MPa)
4.41	4.45	8.95	28.50
4.58	4.48	12.13	35.57
4.55	4.43	9.71	29.16
4.58	4.47	9.34	27.46
4.58	4.45	9.34	27.57
4.58	4.44	12.12	35.83
4.45	4.45	11.57	36.18
4.72	4.44	11.70	32.60
4.40	4.45	10.46	33.46

18 wt. % Zirconia additions

Sample Thickness (mm)	Sample Width (mm)	Load at Failure (Kg)	MOR (MPa)
4.02	4.36	7.37	28.80
4.11	4.38	7.14	26.56
4.01	4.3	8.27	32.47
4.03	4.39	9.342	36.08
4.00	4.38	7.54	29.59
4.08	4.32	7.41	27.98
4.03	4.39	7.97	30.77
4.03	4.36	7.68	29.86

20 wt. % Zirconia additions

Sample Thickness (mm)	Sample Width (mm)	Load at Failure (Kg)	MOR (MPa)
4.10	4.52	7.62	27.54
3.83	4.47	7.98	33.61
4.15	4.47	8.83	31.56
4.01	4.53	6.75	25.48
4.10	4.44	7.48	27.59
4.24	4.44	7.61	26.25
4.22	4.45	7.05	24.55
4.07	4.47	9.06	33.69

APPENDIX F (cont.)

24 wt. % Zirconia additions

Sample <u>Thickness (mm)</u>	Sample <u>Width (mm)</u>	<u>Load at Failure (Kg)</u>	<u>MOR (MPa)</u>
4.25	4.50	8.46	28.42
4.30	4.50	8.70	28.78
4.26	4.48	7.09	23.90
4.25	4.52	7.65	25.77
4.34	4.53	8.66	27.93
4.26	4.54	6.98	23.32
4.24	4.54	6.71	22.63
4.22	4.55	8.26	28.05

APPENDIX G

Raw Data for Modulus of Rupture Measurements

Precipitation Toughened Samples

6.7 Mole % Niobia Doped Bismuth Oxide

Sample <u>Thickness (mm)</u>	Sample <u>Width (mm)</u>	<u>Load at Failure (Kg)</u>	<u>MOR (MPa)</u>
4.57	4.33	8.86	27.77
4.70	4.35	9.46	27.92
4.65	4.35	9.18	27.67
4.60	4.36	7.92	24.33
4.65	4.35	8.56	25.81
4.70	4.37	8.63	25.34
4.68	4.34	8.67	25.86

10.0 Mole % Niobia Doped Bismuth Oxide

Sample <u>Thickness (mm)</u>	Sample <u>Width (mm)</u>	<u>Load at Failure (Kg)</u>	<u>MOR (MPa)</u>
4.84	4.63	9.46	24.73
4.86	4.63	10.62	27.52
5.00	4.63	10.94	26.79
4.88	4.58	8.74	22.71
5.12	4.56	9.53	22.60
4.85	4.57	10.11	26.66
4.77	4.59	10.95	29.72

APPENDIX G (cont.)

12.0 Mole % Niobia Doped Bismuth Oxide

Sample Thickness (mm)	Sample Width (mm)	Load at Failure (Kg)	MOR (MPa)
4.58	4.38	12.13	36.80
4.58	4.38	11.36	34.47
4.54	4.38	10.01	30.91
4.58	4.40	10.47	31.62
4.53	4.38	12.60	39.08
4.58	4.40	11.49	34.70
4.66	4.41	13.05	37.99
4.63	4.39	9.41	27.87
4.67	4.39	10.50	30.57

13.0 Mole % Niobia Doped Bismuth Oxide

Sample Thickness (mm)	Sample Width (mm)	Load at Failure (Kg)	MOR (MPa)
4.46	4.43	7.18	22.72
4.66	4.36	8.16	24.03
4.57	4.41	10.13	30.66
4.68	4.36	6.09	17.71
4.66	4.40	8.80	25.68
4.67	4.34	10.89	32.07
4.68	4.34	7.22	21.18
5.01	4.39	8.43	21.33
4.63	4.39	11.93	35.34

APPENDIX G (cont.)

14.0 Mole % Niobia Doped Bismuth Oxide

Sample Thickness (mm)	Sample Width (mm)	Load at Failure (Kg)	MOR (MPa)
4.68	4.36	12.16	35.56
5.06	4.40	8.28	20.49
4.78	4.36	6.71	18.78
4.78	4.36	12.03	33.66
4.61	4.38	7.57	22.67
4.71	4.36	10.60	30.55
4.88	4.35	13.72	36.92
4.62	4.40	12.26	36.39
4.61	4.35	9.79	29.50

16.3 Mole % Niobia Doped Bismuth Oxide

Sample Thickness (mm)	Sample Width (mm)	Load at Failure (Kg)	MOR (MPa)
4.44	4.34	9.91	32.27
4.35	4.33	10.77	36.61
4.24	4.30	14.14	51.06
4.30	4.29	10.99	38.62
4.29	4.30	14.82	52.20
4.25	4.31	11.17	39.98
4.31	4.30	9.05	32.85
4.11	4.30	10.17	39.03
4.24	4.31	8.12	29.22
4.25	4.27	12.79	46.23
3.78	4.38	5.73	25.53
4.35	4.35	17.68	59.87

APPENDIX G (cont.)

19.3 Mole % Niobia Doped Bismuth Oxide

Sample Thickness (mm)	Sample Width (mm)	Load at Failure (Kg)	MOR (MPa)
4.02	4.46	6.63	26.08
4.85	4.38	9.37	25.78
4.77	4.48	7.57	21.05
4.72	4.41	8.31	23.97
4.48	4.27	8.64	28.59
4.46	4.68	5.80	17.66

REFERENCES

1. T. Takahashi, H. Iwahara and T. Arao, "High Oxide Ion Conduction in Sintered Oxides of the System Bi_2O_3 ", *J. of Applied Electrochemistry*, Vol. 5, 187-195, (1975).
2. W. N. Lawless, "Solid State Oxygen Compressor for Joule-Thompson Cryocoolers", Phase I Final Report, Contract #DNA001-87-C-0198, (1988).
3. J. R. Manning, Diffusion Kinetics for Atoms in Crystals, D. Van Nostrand Co. Inc. 10-40, (1968).
4. E. M. Levin and R. S. Roth, "Polymorphism of Bismuth Sesquioxide. I. Pure Bi_2O_3 ", *Journal of Research of the National Bureau of Standards, A. Physics and Chemistry*, Vol. 68A, No. 2, 189- 195, (1964).
5. E. M. Levin and R. S. Roth, "Polymorphism of Bismuth Sesquioxide. II. Effect of Oxide Additions on the Polymorphism of Bi_2O_3 ", *ibid.* 195-200.
6. H. A. Harwig. "On the Structure of Bismuth Sesquioxide: The α , β , γ and δ Phase", *Z. Anorg. Allg. Chem.*, Vol 444, 151-166, (1978).
7. G. Malmros, "The Crystal Structure of α - Bi_2O_3 ", *Acta Chem. Scand.*, Vol. 24, No. 2, 384-396, (1970).

8. K. Khachaturyan, "On the Prediction of Structure Changes in Bi_2O_3 Caused by Ordering and Pseudo-Jahn-Teller Instability", *Acta Cryst.* B24, 213-224, (1986).
9. L. G. Sillen, "X-Ray Studies on Bismuth Trioxide", *Arkiv. Kemi, Mineralogi Och Geologi*, Vol 16, Bd. 12A, No. 18, 1-13, (1943).
10. H. A. Harwig. "Phase Relations in Bismuth Sesquioxide", *Z. Anorg. Allg. Chem.*, Vol 444, 167-177, (1978).
11. W. C. Schumb and E. S. Rittner, "Polymorphism of Bismuth Trioxide", *J. Material Science*, Vol 65, 1055-1060,(1943).
12. R. S. Roth and J. L. Waring, "Phase Equilibrium Relations in the Binary System Bismuth Sesquioxide - Niobium Pentoxide", *J. of Res. Nat. Bur. of Stds. , A. Physics and Chemistry*, Vol. 66A, No. 6, 197-206, (1962).
13. W. Zhou, D. A. Jefferson and J. M. Thomas, "A New Structure Type in the Bi_2O_3 - Nb_2O_5 System", *J. Solid State Chem.*, Vol. 70, 129-136, (1987).
14. V. J. Powers, "Electrical Properties and Phase Stability in the High Oxygen Conducting System Bi_2O_3 - Y_2O_3 - Nb_2O_5 ", PhD. Thesis, The Ohio State University, 128-150, (1989).
15. A. G. Evans, D. R. Biswas and R. M. Fulrath, "Some Effects of Cavities on the Fracture of Ceramics: I, Cylindrical Cavities", *J. Am. Cer. Soc.*, Vol. 62, No. 1-2, 95-99, (1979).
16. A. G. Evans, D. R. Biswas and R. M. Fulrath, "Some Effects of Cavities on the Fracture of Ceramics: II, Spherical Cavities", *J. Am. Cer. Soc.*, Vol. 62, No. 1-2, 101-106, (1979).
17. R. E. Fryxell and B. A. Chandler, "Creep, Strength, Expansion, and Elastic Moduli of Sintered BeO as a Function of Grain Size, Porosity, and Grain Orientation", *J. Am. Cer. Soc.*, Vol. 47, No. 6, 283-291, (1964).

18. R. M. Spriggs, "Effect of Open and Closed Pores on Elastic Moduli of Polycrystalline Alumina", *J. Am. Cer. Soc.*, Vol. 45, No. 9, 454, (1962).
19. R. M. Spriggs, "Expression for Effect of Porosity on Elastic Modulus of Polycrystalline Refractory Materials, Particularly Aluminum Oxide", *J. Am. Cer. Soc.*, Vol. 45, No. 9, 454, (1962).
20. D. P. Hasselman, "On the Porosity Dependence of Elastic Moduli of Polycrystalline Refractory Alumina", *J. Am. Cer. Soc.*, Vol. 45, No. 9, 452-53, (1962).
21. R. L. Coble and W. D. Kingery, "Effect of Porosity on Physical Properties of Sintered Alumina", *J. Am. Cer. Soc.*, Vol. 39, No. 11, 377-385, (1962).
22. J. K. Mackenzie, "Elastic Constants of a Solid Containing Spherical Holes", *Proc. Phys. Soc., London*, 63B No. 1, 2-11, (1950).
23. O. Hunter and G. E. Graddy, "Porosity Dependence of Elastic Properties of Polycrystalline Cubic Lu_2O_3 ", *J. Am. Cer. Soc.*, Vol. 59, No. 1-2, 82, (1962).
24. E. A. Dean and J. A. Lopez, "Empirical Dependence of Elastic Moduli on Porosity for Ceramic Materials", *J. Am. Cer. Soc.*, Vol. 66, No. 5, 366-370, (1983).
25. F. P. Knudsen, "Dependence of Mechanical Strength of Brittle Polycrystalline Specimens on Porosity and Grain Size", *J. Am. Cer. Soc.*, Vol. 42, No. 8, 376-387, (1959).
26. E. Ryshkewitch, "Compression Strength of Porous Sintered Alumina and Zirconia - 9th Communication to Ceramography", *J. Am. Cer. Soc.*, Vol. 36, No. 2, 65-68, (1953).

27. C. E. Inglis, Proceedings, Institute of Naval Architects, Vol. 55, 139-145, (1913).
28. R. W. Hertzberg, Deformation and Fracture Mechanics of Engineering Materials, John Wiley and Sons, New York, 269-322, (1976).
29. E. Orowan, "Fracture and Strength of Solids [Metals]", Repts. Progr. in Phys., Vol. 12, 185-232, (1949).
30. A. A. Griffith, "Phenomena of Rupture and Flow in Solids", Phil. Trans. Roy. Soc. London, A221, 163-198, (1920).
31. N. J. Petch, "Cleavage Strength of Polycrystals", J. Iron Steel Inst. (London), Vol. 174, Part I, 25-28, (1953).
32. R. W. Rice, "Strength/Grain-Size Effects in Ceramics", Properties and Microstructure, R. K. MacCrone Ed., Academic Press, New York, 205-249, (1977).
33. R. W. Rice, S. W. Freiman and P. F. Becher, "Grain-Size Dependence of Fracture Energy in Ceramics: I, Experiment", J. Am. Cer. Soc., Vol. 64, No. 6, 345-350, (1981).
34. A. G. Evans and G. Tappin, "Effects of Microstructure on the Stress to Propagate Inherent Flaws", Proc, Br. Ceram. Soc., Vol. 20, 275-297, (1972).
35. T. Vasilos, J. B. Mitchell and R. M. Spriggs, "Mechanical Properties of Pure, Dense Magnesium Oxide as a Function of Temperature and Grain Size", J. Am. Cer. Soc., Vol. 47, No. 12, 606-610, (1964).
36. R. L. Coble, "Effect of Microstructure on Mechanical Properties of Ceramic Materials", Ceramic Fabrication Processes, W. D. Kingery Ed., Technology Press of Mass. Institute of Tech., Cambridge, 213-228, (1958).

37. F. W. Dynys and J. W. Halloran, "Influence of Aggregates on Sintering", *J. Am. Cer. Soc.*, Vol. 67, No. 9, 598-601, (1984).
38. H. L. Hsieh and T. T. Fang, "Effects of Powder Processing on the Green Compacts of High-Purity BaTiO₃", *J. Am. Cer. Soc.*, Vol. 72, No. 1, 142-145, (1989).
39. F. F. Lange, "Sinterability of Agglomerated Powders", *J. Am. Cer. Soc.*, Vol. 67, No. 2, 83-89, (1984).
40. A. G. Evans, "The Strength of Brittle Materials Containing Second Phase Dispersions", Fracture Mechanics of Ceramics, Vol. 4, 1327-1344. (1981).
41. F. F. Lange, "The Interaction of a Crack Front with a Second-Phase Dispersion", *Philos. Mag.* Vol. 22, 983-993, (1983).
42. D. J. Green and P. S. Nicholson, "Fracture of Brittle Particulate Composites", Fracture Mechanics of Ceramics, Vol. 4, 945-960.
43. D. P. H. Hasselman and R. M. Fulrath, "Proposed Fracture of a Dispersion-Strengthened Glass Matrix", *J. Am. Cer. Soc.*, Vol. 49, No. 2, 68-72, (1966).
44. K. T. Faber, A. G. Evans and M. D. Drory, "A Statistical Analysis of Crack Deflection as a Toughening Mechanism in Ceramic Materials", *Fracture Mechanics of Ceramics*, Vol. 6, 77-91, (1974).
45. K. T. Faber and A. G. Evans, "Crack Deflection Processes- II. Experiment", *Acta. Metall.*, Vol. 31, No. 4, 577-584, (1983).
46. R. M. McMeeking and A. G. Evans, "Mechanics of Transformation - Toughening in Brittle Material", *J. Am. Cer. Soc.*, Vol. 65, No. 5, 242-246, (1982).

47. Communication from Kenny Associates on the Rate Controlled Sintering of BNO powder compacts. (1989).
48. P. Chantikul, G. R. Anstis, B. R. Lawn and D. B. Marshall, "A Critical Evaluation of Indentation Techniques for Measuring Fracture Toughness: II, Strength Method", *J. Am. Cer. Soc.*, Vol. 64, No. 9, 539-543, (1981).
49. T. Tada, H. Paris and G. Irwin, The Stress Analysis of Cracks Handbook, Del Research Corp., Heelertown, Pa., (1973).
50. E. A. Smith, "Some Special Functions of the Vibrational Ball Mill", *Chemistry and Industry*, August 26, 1437-1442, (1967).
51. H. E. Rose, "Some Observations on the Application of Vibration Mills", *Chemistry and Industry*, August 19, 1383-1390, (1967).
52. C. F. Cooper, "Ceramic Fabrication Science Some Problems", *Proc. Brit. Ceram. Soc.*, Vol. 56, No. 11, (1973).
53. E. R. Kreidler, "Conventional Sintering Study of BNO Ceramics", Report to CeramPhysics, Inc., December 12, (1988).
54. V. Powers, Personal Communications, The Ohio State University, Columbus, Ohio.
55. B. Lawless and F. Clark, Personal communications CeramPhysics, Inc., Westerville, Ohio. (1991).
56. P. Anderson and D. Sherman, "Finite Element Analysis of Honeycomb Structures", *Interm Reports*, The Ohio State University, (1990).
57. Finite element analysis was done using a program called ABAQUS made by HKS, Inc.

58. W. Summers, "Broad Scope Particle Size Reduction by Means of Vibratory Grinding", Ceramic Bulletin, Vol. 62, No. 2, 212-215, (1983).
59. K. H. Petersson and B. Bergman, "Comparison of Fracture Toughness Testing Methods Applied to Alumina-Zirconia Material", Acta Metall., Vol. 37, No. 5, 15-22, (1987).
60. N. Miyata and H Jinno, "Fracture Toughness and Fracture Energy of Lead Borate Glasses", J. Mat. Sci. Letters, Vol 1, 156 - 158, (1982).
61. W. D. Kingery, H. K. Bowen and D. R. Uhlmann, Introduction to Ceramics, John Wiley and Sons, New York, (1976).
62. F. F. Lange and M. Hirlinger, "Hindrance of Grain Growth in Al_2O_3 by ZrO_2 Inclusions", J. Am. Cer. Soc., Vol. 67, No. 3, 164-168, (1984).
63. N. Claussen, "Strengthening Strategies for ZrO_2 -Toughened Ceramics At High Temperature", Mat. Sci. Eng., Vol.71, 23-38, (1985).

DISTRIBUTION LIST

DNA-TR-96-45

DEPARTMENT OF DEFENSE

DEFENSE INTELLIGENCE AGENCY
ATTN: DT-1

DEFENSE SPECIAL WEAPONS AGENCY
ATTN: ESA, W Summa
ATTN: EST, R Gullickson
2 CYS ATTN: ISST
ATTN: WE
ATTN: WEL
ATTN: WEL, L Wittwer

DEFENSE TECHNICAL INFORMATION CENTER
2 CYS ATTN: DTIC/OCP

FC DEFENSE SPECIAL WEAPONS AGENCY
ATTN: FCTT Dr BALADI
ATTN: FCTT, J Hughes

DEPARTMENT OF THE ARMY

MDSTC
ATTN: CSSD-TC-AC I Merritt

U.S. ARMY NUCLEAR & CHEMICAL AGENCY
ATTN: MONA-NU
ATTN: MONA-NU, Cpt Umend

DEPARTMENT OF THE NAVY

NAVAL PLANT REPRESENTATIVE OFFICE
LOCKHEED MISSILE & SPACE CO, INC
ATTN: R R Hess

DEPARTMENT OF THE AIR FORCE

PHILLIPS LABORATORY
ATTN: PL/SUL

DEPARTMENT OF ENERGY

LAWRENCE LIVERMORE NATIONAL LAB
ATTN: David Stanfel, L-313 L-13
ATTN: F Heuze, L-200
ATTN: W Farley, L-84
2 CYS ATTN: Technical Information Div Lib, L-53

LOS ALAMOS NATIONAL LABORATORY
2 CYS ATTN: Technical Library
ATTN: X-5, D218, J Brownell

SANDIA NATIONAL LABORATORIES
4 CYS ATTN: D Cook, MS 1169
ATTN: F Dean, MS 0475
ATTN: W H Barrett, jMS 1159
ATTN: Tech Lib
2 CYS ATTN: Tech Lib, MS 0899

DEPARTMENT OF DEFENSE CONTRACTORS

APTEK, INC.
ATTN: T. Meagher

CERAMPHYSICS INC
2 CYS ATTN: W N Lawless

DEFENSE GROUP, INC.
ATTN: Robert Poll

JAYCOR
ATTN: Cyrus P Knowles

KAMAN SCIENCES CORP
ATTN: C Eklund

KAMAN SCIENCES CORP
2 CYS ATTN: DASIAc

LOCKHEED MARTIN CORPORATION
ATTN: S Salisbury

M I T LINCOLN LAB
ATTN: C F Wilson

MAXWELL LABORATORIES INC
S-CUBED DIVISION
ATTN: Dr C Wilson
ATTN: Dr E Peterson

PRIMEX PHYSICS INTERNATIONAL
ATTN: G B Frazier

TECH REPS, INC
ATTN: F McMullan

TRW INC
ATTN: T.I.C., S/1930